Available online at www.sciencedirect.com
SCIENCE DIRECT®
ELSEVIER
Nuclear Physics A 713 (2003) 231–310
NUCLEAR PHYSICS A
www.elsevier.com/locate/npe

Local and global nucleon optical models from 1 keV to 200 MeV

A.J. Koning [a,*], J.P. Delaroche [b]

[a] *Nuclear Research and Consultancy Group NRG, PO Box 25, 1755 ZG Petten, The Netherlands*
[b] *Commissariat à l'Energie Atomique, DAM/DIF/DPTA, Boîte Postale 12, 91680 Bruyères-le-Châtel, France*

Received 7 August 2002; received in revised form 24 September 2002; accepted 2 October 2002

Abstract

We present new phenomenological optical model potentials (OMPs) for neutrons and protons with incident energies from 1 keV up to 200 MeV, for (near-)spherical nuclides in the mass range $24 \leqslant A \leqslant 209$. They are based on a smooth, unique functional form for the energy dependence of the potential depths, and on physically constrained geometry parameters. For the first time, this enables one to predict basic scattering observables over a broad mass range and over an energy range that covers several orders of magnitude in MeV. Thereby, the necessity of using different OMPs in different energy regions has been removed. Using extensive grid searches and a new computational steering technique, we have obtained optical model parameters for many isotopes separately. We recommend that the resulting, so-called local, optical models be used in theoretical analyses of nuclear data. From these parameterizations, we have also constructed asymmetry-dependent neutron and proton global OMPs that are superior to all other existing phenomenological ones, not only with respect to the description of observables, but also as they cover larger mass and energy ranges. These (nucleon) global OMPs, we believe, may be used with some confidence in other studies whenever one of our local OMPs does not exist. To constrain our parameterization as much as possible and to assess the performance of our OMPs, we have compared our calculated results with an extensive experimental data set. This data set includes average resonance parameters, total and non-elastic cross sections, elastic scattering angular distributions and analyzing powers. The numerous local OMPs we have obtained allow us to disentangle asymmetry, Coulomb correction and mass-dependent components of our global OMPs.

PACS: 24.10.-i; 24.10.Ht; 25.40.-h; 25.40.Cm; 25.40.Dn; 28.20.-v

* Corresponding author.
E-mail addresses: koning@nrg-nl.com (A.J. Koning), jean-paul.delaroche@cea.fr (J.P. Delaroche).

0375-9474/02/$ – see front matter
PII: S0375-9474(02)01321-0

1. Introduction

The optical model has a significant impact on many branches of nuclear reaction physics. The central assumption of that model is that the complicated interaction between an incident particle and a nucleus can be represented by a complex mean-field potential, which divides the reaction flux into a part covering shape elastic scattering and a part describing all competing non-elastic channels. Solving the Schrödinger equation with this complex potential yields a prediction for the basic observables, namely the elastic scattering angular distribution and analyzing power, the reaction and total cross sections and, for low neutron energies, the s- and p-wave strength functions (S_0, S_1) and the potential scattering radius (R'). An important feature of a good OMP is that it can be used to reliably predict these observables for energies and nuclides for which no measurements exist, while the ingredients of the model, either microscopic or phenomenological, are physically well-behaved. Moreover, the quality of several derived quantities that are provided by the optical model has an important impact on the evaluation of the various non-elastic channels. Well-known examples are S-matrix elements and the related transmission coefficients that enter the statistical model of compound nucleus evaporation, and the distorted wave functions that are used for the description of direct inelastic scattering to discrete states as well as in evaluations of multi-step direct transitions to the continuum. The reaction cross sections that are calculated with the optical model are important for the evaporation part of intranuclear cascade models and also for semi-classical pre-equilibrium models. All these nuclear models for the non-elastic channels rely on various other ingredients, such as discrete level schemes, level densities, gamma-ray strength functions, fission barriers, etc. Uncertainties in those quantities all add to the total uncertainty of the calculated results. Therefore, it is crucial that the OMPs which enter such nuclear model calculations be adequately determined, independent pieces of information.

The construction of reliable phenomenological OMPs on a broad scale is exactly the purpose of this paper. For each (near-)spherical nucleus for which appropriate experimental data exists, we have constructed local neutron and proton OMPs for the entire 1 keV–200 MeV energy region without any discontinuities in their parameter values. In addition, we have constructed global neutron and proton OMPs for the same energy region and for nearly the whole periodic table of elements (more precisely, for $24 \leqslant A \leqslant 209$). All OMPs are based on the same smooth energy dependent functional forms for the potential depths, while the associated geometry parameters are constrained within acceptable limits around a global average. Apart from an unprecedented fit to the observables, we can pin down the behaviour of the various components of the OMP, which will serve as additional assessment of the quality of microscopic optical model approaches. We hope that the most important spin-off of our new OMPs is a significant increase in the precision of the description of non-elastic reaction channels up to 200 MeV.

Throughout this paper, we will compare our OMPs with other existing potentials. Therefore, to put our work better in perspective, we now proceed with a general categorization of OMPs.

1.1. Microscopic and phenomenological optical models

In a broad sense, one may distinguish between the microscopic optical model and the phenomenological optical model. In the microscopic optical model, the nucleon–nucleon effective interaction is folded with the matter density distribution to give a direct measure of the strength and shape of the nuclear potential. In the phenomenological optical model, one adopts a suitable analytical form for the potential, usually a Woods–Saxon form, and determines its depth and geometry parameters by means of parameter adjustment to best fit available experimental data. The simultaneous development of both approaches is important, since they usually serve as each others' guide and inspiration. Recently, there has been considerable progress in microscopic optical models (see, e.g., [1–3]). In this paper, we will develop new phenomenological OMPs that will provide a new challenge, in terms of predictive power, to the microscopic approaches.

1.2. Local and global optical models

From the literature, it seems that there are three methods commonly used to set the parameterization of the phenomenological OMP, which vary in the amount and type of data used. They are (i) a *"best-fit" optical model*, representing a potential for one nucleus and one single incident energy, (ii) a *local optical model*, representing a potential for one nucleus and an energy region, and (iii) a *global optical model*, in which a potential is specified for both a mass region and an energy region. In addition to this classification, one can consider neutron and proton potentials separately or a more general isospin dependent nucleon potential, and one can distinguish between the spherical and deformed OMPs, the latter being applied in coupled channels analyses. Note that we define the term *local* optical model as the opposite case of the global optical model. Thus, in this paper the term does *not* indicate an equivalent local potential for a non-local, energy-dependent potential.

Of these approaches, the best-fit potentials (case (i)) obviously give the best description of measured data. Indeed, it is usually not too difficult to obtain a satisfactory fit of a single elastic angular distribution since there are, usually, more than 10 parameters available for adjustment. Unfortunately, the obtained parameter sets invariably are uncorrelated from energy to energy, whereas one may a priori assume that at least the geometry parameters should, albeit in an effective way, reflect the size and structure of the nucleus and thus be energy independent. While best-fit potentials alone are useless for the prediction of observables at energies for which no measurements exist, they are useful for the determination of global trends in optical model parameters as a function of energy. We have used that approach, by means of so-called grid searches, as a first step in the construction of our parameterizations.

The other extreme is case (iii), the global optical model. From a physical point of view, a *phenomenological* global optical model should not be expected to provide an adequate description of a nucleon–nucleus interaction, simply because the nuclear structure differences among adjacent nuclei cannot be cast into a simple and smooth Z- and A-dependence of the Woods–Saxon parameters. Only *microscopic* optical models can be expected to provide these local nucleus-by-nucleus differences, since they are built from detailed nuclear structure properties. However, the global phenomenological optical

model provides a convenient average description of the overall trend of the interaction as a function of mass and energy and is the only option for nuclides for which experimental data and a microscopic approach are not available. For this reason, part of the results presented in this paper consists of new neutron and proton global OMPs. As we will show, they significantly outperform all previous global OMPs.

Nevertheless, we argue that the best approach is given by the local optical model (case (ii)), in which an OMP parameter set is found for each target nucleus separately, and with its energy behaviour expressed analytically. The parameters of these functions must then vary around those of the global OMP within acceptable limits. We expect, and actually find, that the optical model parameters for a particular nucleus are similar to those of a neighboring one, but the way in which the parameter sets of two adjacent nuclides differ turns out to be unpredictable. Again, this is not surprising, since the Woods–Saxon form factor is a very approximative representation of the complicated nucleon–nucleus interaction, including all its shell and deformation effects, and this is reflected by unpredictable changes in the phenomenological parameters from nucleus to nucleus. Furthermore, it is well known that the actual nucleon–nucleus interaction is non-local; due if to nothing else than the Pauli principle. However, as has been shown [2], there always exists an equivalent local potential for the scattering phase shifts generated from any fully non-local interaction. Basically the non-locality translates into an energy dependence of that equivalent local field.

In sum, local OMPs for each nucleus are the most appropriate for the analysis of experimental data. The best-fit potentials serve as tools to initialize the local OMP parameter set and the global OMP serves as a guideline to keep the parameters within physically reasonable bounds. Accordingly, this entails that in this work we have developed local and global OMPs iteratively. Of course, such OMPs can only be taken seriously if the number of free parameters is kept to a minimum, certainly with respect to the number of data points to be described. We argue here that, in comparison with earlier work, we have *reduced* the number of parameters but still get a better description of the experimental data.

1.3. Energy and mass range

The use of the optical model in other nuclear reaction models, for non-elastic channels, clearly indicates the need for OMP parameterizations over a broad energy range. The problem one generally faces is that for the theoretical calculation of all non-elastic reaction spectra, reliable OMPs are required from the incident projectile energy down to a few keV. Prior to the present work, complete parameterizations for energies covering several orders of magnitude in MeV only existed for a few nuclides, usually obtained with dispersion relations. Thus complete nuclear reaction analyses have mostly been restricted to the use of uncorrelated OMP parameterizations in various energy regions. Consequently there have been undesired discontinuities at the matching energies, not only for the predicted standard observables, but also for all other derived cross sections, spectra and angular distributions. Especially this aspect motivated us to revisit the standard optical model with Woods–Saxon form factors, and to eliminate these restrictions.

We realize the restrictions of adopting a spherical optical model for *all* energies and target masses. The phenomenological optical model is physically dubious for light nuclei,

which we would define as $A < 24$. It is also dubious for many nuclei, especially in the rare earth and actinide regions, which must be described by deformed OMPs that take into account the strong channel coupling to the first collective excited states. Nuclides for which those features are known to be relevant, therefore have been excluded from the present analysis.

The energy range is also limited since, above about 200 MeV, the Woods–Saxon form is known to be inappropriate, and a "wine-bottle" shape of the form factor is more favored. This can also be attributed to the natural non-locality of the nucleon–nucleus interaction [2]. In addition, the depth of real volume potential is changing sign around this energy, and there are indications that the imaginary part of the volume potential increases due to increasing importance of relativistic dynamics. Thus, in this study we have not considered light mass and strongly deformed nuclides, and we have not considered nucleon projectile energies above 200 MeV.

1.4. Optical model calculations and optimization

The determination of phenomenological OMP parameters from a set of different experimental observables has often been described as an art rather than a science. In particular, χ^2 optimization has a reputation in optical model research that is always under debate. Therefore, we use χ^2 assessments only to initialize the OMP parameters.

There are however various reasons why we can expect an improvement over the last large-scale optical model study of 1991, by Varner [4]. First, there is now a much better experimental database (which includes for example high-energy neutron total cross sections for many nuclides) with which OMP parameters can be better constrained. Indeed, our analysis is based on an unprecedented collection of experimental data, and the references for this database are listed in Tables 1, 2 and 7. In addition, there is now enhanced theoretical guidance from the microscopic optical model approaches. The significant increase in computer power enables us to use more robust parameter optimization methods than in the past. The two methods used here are Simulated Annealing (see Section 3), and a new visualization technique, called computational steering [5], which enabled us to obtain the final OMP parameters manually; an activity considered impossible until recently. Since we wish to emphasize the power of this approach, we give a description of the relevant software package, ECISVIEW, in Section 3. All the individual optical model calculations have been performed with the versatile code ECIS-97 [6], which takes into account both low-energy (compound nucleus) and high-energy (relativistic) effects.

1.5. This paper

A central feature of our work is that we treat all nuclei on the same footing. In the past, a new local OMP was generated whenever new experiments were added to the existing experimental database for the nucleus under consideration. Inevitably, the functional form of the OMP for a particular nucleus then differed from paper to paper. Also certain nuclides (e.g., ^{40}Ca, ^{90}Zr, and ^{208}Pb) were better covered than others. On the other hand, global optical model studies were not so variable since they used complete databases for the energy and mass ranges under study. However, their results lacked the precision of the

Table 1
$d\sigma/d\Omega$ and $A_y(\theta)$ database for neutron elastic scattering

Target	Ref.	Energy (MeV)	Ref.	Energy (MeV)
^{24}Mg	[61]	3.4	[63]	9.8, 14.8
	[62]	6.1		
^{nat}Mg	[64]	1.9, 2.8, 3.8, 4.8	[67]	11
	[65]	5.4, 6.4, 7.6, 8.6	[68]	14.8
	[66]	8	[69]	21.6
^{27}Al	[70]	3.2	[75]	18, 20, 22, 25, 26
	[71]	5.4 6.4, 7.5, 8.6	[76]	84
	[72]	7.6	[77]	96
	[73]	10.9, 13.9, 16.9	[78]	136
	[74]	14, 17		
^{28}Si	[79]	21.7	[80]	30.3, 40
^{nat}Si	[71]	5.4, 6.4, 7.6, 8.6	[81]	11, 20, 26
	[51]	8, 10, 12, 14, 17	[29]	55, 65, 75
^{31}P	[82]	3.5, 3.9, 4.2, 4.5, 4.8	[84]	7.8, 9
	[83]	6		
^{32}S	[79]	21.7		
^{nat}S	[85]	3, 4, 7.1	[67]	11
	[86]	5.5, 6.4, 7.6, 8.5	[81]	20, 26
	[51]	8, 10, 12, 14, 17	[87]	30.3, 40
^{nat}Cl	[88]	14.1		
^{nat}Ar	[72]	7.8	[89]	14
^{nat}K	[90]	3	[91]	3.7, 4.3, 6.5, 7.9
^{40}Ca	[91]	2.1, 3.3, 5.3, 5.9, 6.5, 7.9	[47]	11, 20, 26
	[92]	9.9, 11.9, 13.9	[94]	19
	[93]	11	[95]	21.6
	[30]	16.9	[80]	30.3, 40
^{nat}Ca	[96]	65		
^{45}Sc	[97]	2.6, 2.9, 3.8, 5, 5.9, 6.5 7.1, 8, 9, 10		
^{nat}Ti	[98]	4.5, 5.5, 6.5, 7.6, 8.1 8.4, 9.1, 9.5, 10	[99]	14
^{51}V	[100]	5.4, 6.4, 8.6	[101]	8, 9, 10.1, 10.9, 11.9, 13, 14.4
^{52}Cr	[85]	3, 4	[35]	8, 9, 9.8, 10.8, 11.4, 12
	[102]	4.3, 4.9, 6.4, 7.5, 8.6		12.7, 13.7, 14.1, 14.8
			[69]	21.6
^{55}Mn	[85]	2.5, 3, 3.5, 4, 4.6, 6.1, 7, 8	[67]	11

(*continued on next page*)

Table 1 (*Continued*)

Target	Ref.	Energy (MeV)	Ref.	Energy (MeV)
^{54}Fe	[103]	7, 8.5	[104]	10, 12, 14
	[33]	10, 14, 17	[105]	11, 20, 24, 26
^{56}Fe	[103]	4.6, 5, 5.6, 6.5, 7.6	[105]	11, 20, 26
	[106]	5	[95]	21.6
	[107]	8, 10, 12, 14	[108]	24.8
^{nat}Fe	[29]	55, 65, 75		
^{59}Co	[85]	2, 2.5, 3, 3.5, 4, 4.6, 6.1	[99]	14
		7.1, 8.1	[69]	21.6
	[100]	5, 5.4, 6.4, 7.6, 8.6	[109]	23
	[67]	11		
^{58}Ni	[110]	8, 10, 12, 14	[111]	24
	[33]	10, 14, 17		
^{60}Ni	[112]	4.3, 4.9	[110]	8, 10, 12, 14
	[113]	6.4, 7.5, 8.6	[111]	24
^{nat}Ni	[85]	3, 3.5, 4, 4.6, 6.1, 7	[67]	11
	[112]	5, 6.4, 7.5	[69]	21.6
^{63}Cu	[114]	5.5, 7, 8.5	[104]	8, 10, 12, 14
^{65}Cu	[115]	10, 14		
^{nat}Cu	[116]	1.6, 2, 2.2, 2.6, 3, 3.4, 3.8	[77]	96
	[76]	84	[117]	155
^{nat}Ge	[118]	7.5		
^{75}As	[119]	8.1		
^{80}Se	[120]	4	[121]	8, 10
^{nat}Se	[122]	1	[123]	3.7
	[70]	3.2	[124]	14.1
^{88}Sr	[125]	11		
^{nat}Sr	[126]	0.9	[127]	4.4
	[70]	3.2	[128]	14.8
	[123]	3.7		
^{89}Y	[129]	3.8, 4.5, 5, 5.9, 6.5, 7.1	[131]	8, 10, 12, 14, 17
		7.5, 8.4, 9, 9.5	[132]	11
	[130]	5.5	[69]	21.6
^{90}Zr	[133]	2, 2.6, 3, 3.5, 4	[14]	8, 10, 24
	[134]	2.1, 5.2	[125]	11
	[135]	5.9, 6.9, 7.8		
^{91}Zr	[136]	8, 10, 24		

(*continued on next page*)

Table 1 (*Continued*)

Target	Ref.	Energy (MeV)	Ref.	Energy (MeV)
^{92}Zr	[133]	2, 3, 4	[136]	8, 10, 24
	[135]	5.9, 7, 7.8		
^{94}Zr	[137]	1.5	[136]	8, 10, 24
^{nat}Zr	[29]	55, 65, 75		
^{93}Nb	[138]	2.6, 2.9	[67]	11
	[139]	4.5, 5, 5.5, 5.9, 6.5, 7.1	[140]	10, 12, 14, 14.6, 17
		7.5, 8, 8.4, 9.1	[141]	20
^{92}Mo	[137]	1.5	[143]	6
	[142]	1.8, 2, 2.2, 2.4, 2.6, 2.8, 3	[144]	9, 11, 20, 26
		3.2, 3.4, 3.6, 3.8, 4		
^{96}Mo	[137]	1.5	[143]	6
	[142]	1.8, 2, 2.2, 2.4, 2.6, 2.8, 3	[144]	9, 11, 20, 26
		3.2, 3.4, 3.6, 3.8, 4		
^{98}Mo	[142]	1.8, 2, 2.2, 2.4, 2.6, 2.8, 3	[144]	9, 11, 20, 26
		3.2, 3.4, 3.6, 3.8, 4		
^{100}Mo	[137]	1.5	[143]	6
	[142]	1.8, 2, 2.2, 2.4, 2.6, 2.8, 3	[144]	9, 11, 20, 26
		3.2, 3.4, 3.6, 3.8, 4		
^{103}Rh	[138]	1.5, 1.8, 2.3, 2.8, 3.3, 3.8	[145]	4.5, 5, 5.5, 5.9, 6.5, 7.1
			[145]	7.5, 8, 8.4, 9.1, 9.5, 10
^{nat}Pd	[146]	1.5, 1.8, 2.3, 2.8, 3.3, 3.8	[147]	5.9, 7.1, 8
^{107}Ag	[148]	1.6, 2.2, 2.8, 3.4, 4		
^{nat}Ag	[149]	4.5, 5, 5.5, 5.9, 6.5, 7.1		
		7.5, 8, 8.4, 9.1, 9.5, 10		
^{nat}Cd	[138]	2.3, 2.9, 3.4, 4,	[151]	14.6
	[150]	4.5, 5, 5.5, 5.9, 6.5, 7.1	[77]	96
		7.5, 8.1, 8.4, 9.1, 9.5, 10		
^{nat}In	[152]	4.5, 5, 5.9, 7.1, 8	[67]	11
		9.1, 9.5, 10	[153]	14
^{116}Sn	[154]	10, 14	[155]	11, 24
^{118}Sn	[155]	11, 24		
^{120}Sn	[156]	1.6, 2, 2.2, 2.3, 2.5, 2.7	[157]	6
		2.8, 3, 3.4, 3.8, 4	[154]	10, 11, 14, 17
^{124}Sn	[155]	11, 24		
^{nat}Sn	[158]	24	[96]	65
^{123}Sb	[156]	1.6, 2.1, 2.6, 3, 3.4, 4	[160]	14
	[159]	4.5, 5.5, 5.9, 6.5, 7.1, 7.6		
		8.1, 8.4, 9.1, 9.5, 10		

(*continued on next page*)

Table 1 (*Continued*)

Target	Ref.	Energy (MeV)	Ref.	Energy (MeV)
^{127}I	[120]	4	[161]	16.1
^{nat}Te	[70]	3.2	[162]	14
^{nat}Ba	[122]	1	[164]	5
	[163]	4.1		
^{nat}La	[165]	2.5, 3.1, 3.6	[72]	7.8
^{nat}Ce	[166]	1	[167]	5
	[70]	3.2	[69]	21.6
^{141}Pr	[168]	1.2	[167]	5
	[165]	1.5, 2, 2.5, 3.1, 3.6	[169]	8
	[70]	3.2		
^{142}Nd	[170]	2.5	[171]	7
^{144}Nd	[170]	2.5	[171]	7
^{nat}Nd	[166]	1		
^{148}Sm	[172]	2.5	[174]	7
	[173]	6.2		
^{197}Au	[175]	2.5	[177]	7
	[176]	4.1	[178]	8
	[167]	5		
^{nat}Hg	[179]	3.0	[124]	14.8
	[70]	3.2	[161]	16.1
^{206}Pb	[177]	7	[67]	11
	[72]	7.7	[180]	13.7
	[119]	8.1	[69]	21.6
^{208}Pb	[181]	2	[87]	30.3, 40
	[23]	4, 4.5, 5, 5.5	[29]	55, 65, 75
	[182]	6, 7, 8, 9, 10, 14, 17	[76]	84
	[183]	9, 11, 20, 25.7	[77]	96
	[69]	21.6	[78]	136
	[37]	22, 24	[117]	155
	[109]	23		
^{209}Bi	[184]	2, 2.5, 3, 3.5, 4, 4.5, 6, 6.5, 7, 7.5, 8, 9, 10, 11, 12, 20, 24	[23]	5, 5.5
			[186]	6, 9
	[179]	3	[72]	7.8
	[185]	4.5	[187]	21.6

local optical model. In this paper we consider both local and global OMPs, using the same methodology so that systematic "errors" in the determination of OMP parameters are minimized.

Table 2
Total cross section database for incident neutrons

Target	Ref.	Target	Ref.
^{nat}Mg	[25,188]	^{89}Y	[25,205]
^{27}Al	[24,189–191]	^{90}Zr	[24,133,206,207]
^{nat}Si	[24,191–193]	^{93}Nb	[24,138,205,208]
^{nat}S	[24,194,195]	^{nat}Mo	[25,195,205,209]
^{40}Ca	[24,196]	^{nat}Sn	[24,205,210]
^{nat}Ti	[25,197]	^{nat}Ce	[189,195,211–214]
^{nat}Cr	[25,192,198,199]	^{197}Au	[25,215]
^{56}Fe	[25,192,200,201]	^{nat}Hg	[25,195,211,216]
^{58}Ni	[25,202,203]	^{208}Pb	[24,195,217,218]
^{nat}Cu	[24,116,204]	^{209}Bi	[24,184,195,219,220]

Our results will be directly applicable in optical model calculations. So far, two large OMP parameter collections have been assembled: the study by Perey and Perey [7] and, more recently, by Young [8]. The results of this paper are added to the latter collection and can also be obtained in direct usable form, including a parameter calculator, from the authors [9].

This paper is set up as follows. In Section 2 we discuss the basic functional form of our OMP. In Section 3 we give an outline of the optimization method. Section 4 contains a comparison of our OMP results with experimental data, for incident neutrons and protons and on a nucleus by nucleus basis. In Section 5, we identify the asymmetry and Coulomb correction terms of the potential in order to build a global nucleon–nucleus OMP. The results are then compared with experimental data and with other optical model predictions. In Section 6 we provide integral properties of out global OMP by means of volume integrals. Finally, we give the conclusions in Section 7.

2. Theory

2.1. The optical model potential

The phenomenological, OMP for nucleon–nucleus scattering, $\mathcal{U}$, usually is defined as

$$\begin{aligned}\mathcal{U}(r,E) = {} & -\mathcal{V}_V(r,E) - i\mathcal{W}_V(r,E) - i\mathcal{W}_D(r,E) \\ & + \mathcal{V}_{SO}(r,E).\mathbf{l}.\sigma + i\mathcal{W}_{SO}(r,E).\mathbf{l}.\sigma + \mathcal{V}_C(r),\end{aligned} \tag{1}$$

where $\mathcal{V}_{V,SO}$ and $\mathcal{W}_{V,D,SO}$ are the real and imaginary components of the volume-central (V), surface-central (D) and spin–orbit (SO) potentials, respectively. E is the laboratory energy of the incident particle in MeV. All components are separated in E-dependent well depths, V_V, W_V, W_D, V_{SO}, and W_{SO}, and energy-independent radial parts f, namely

$$\mathcal{V}_V(r,E) = V_V(E) f(r, R_V, a_V),$$
$$\mathcal{W}_V(r,E) = W_V(E) f(r, R_V, a_V),$$
$$\mathcal{W}_D(r,E) = -4a_D W_D(E) \frac{d}{dr} f(r, R_D, a_D),$$
$$\mathcal{V}_{SO}(r,E) = V_{SO}(E) \left(\frac{\hbar}{m_\pi c}\right)^2 \frac{1}{r}\frac{d}{dr} f(r, R_{SO}, a_{SO}),$$
$$\mathcal{W}_{SO}(r,E) = W_{SO}(E) \left(\frac{\hbar}{m_\pi c}\right)^2 \frac{1}{r}\frac{d}{dr} f(r, R_{SO}, a_{SO}). \tag{2}$$

As usual, the form factor $f(r, R_i, a_i)$ is a Woods–Saxon shape

$$f(r, R_i, a_i) = \left(1 + \exp\left[(r - R_i)/a_i\right]\right)^{-1}, \tag{3}$$

where, with A being the atomic mass number, the geometry parameters are the radius $R_i = r_i A^{1/3}$ and the diffuseness parameters a_i. For charged projectiles, the Coulomb term $\mathcal{V}_C$, as usual, is given by that of a uniformly charged sphere

$$\begin{aligned} \mathcal{V}_C(r) &= \frac{Zze^2}{2R_C}\left(3 - \frac{r^2}{R_C^2}\right), && \text{for } r \leqslant R_C, \\ &= \frac{Zze^2}{r}, && \text{for } r \geqslant R_C, \end{aligned} \tag{4}$$

with $Z(z)$ the charge of the target (projectile), and $R_C = r_C A^{1/3}$ the Coulomb radius.

It is important to note that in Eq. (2) the real and imaginary potentials of each component V and SO share the same form factors, i.e., we assume the same geometry parameters for the pair $(\mathcal{V}_V, \mathcal{W}_V)$ and for the pair $(\mathcal{V}_{SO}, \mathcal{W}_{SO})$, while $\mathcal{W}_D$ has its own geometry parameters. Moreover, we take each r_i and a_i independent of energy. Hence, we have not used the full flexibility of the potential form in our search process. By so doing, we significantly curtail the number of degrees of freedom of the general form, but this is in line with the wanted situation of as few variable parameters as possible in data analyses.

2.2. Functional forms of potential well depths

For both the local and global OMPs we have determined the values for the three pairs of radius and diffuseness parameter and the most appropriate E-dependent parameterization for the various potential depths. In many previous studies, this energy dependence has been modeled by one or more straight line segments. As a consequence, the first derivatives of such parameterizations are discontinuous at the connecting points. Associated problematic anomalies then result for transmission coefficients and angular distributions around those connection points. It is more appropriate to replace these straight line segments by smooth functions that contain the same, and preferably a smaller, number of parameters which at the same time allow more flexibility.

Previous dispersive optical model analyses suggest that all functional forms for the potential depths depend on $(E - E_f)$, where E_f, the Fermi energy in MeV, is defined as

the energy halfway between the last occupied and the first unoccupied shell of the nucleus. For incident neutrons

$$E_f^n = -\frac{1}{2}\big[S_n(Z,N) + S_n(Z,N+1)\big], \tag{5}$$

with S_n the neutron separation energy for a nucleus with proton number Z and neutron number N, while for incident protons

$$E_f^p = -\frac{1}{2}\big[S_p(Z,N) + S_p(Z+1,N)\big], \tag{6}$$

with S_p the proton separation energy. We have used the Audi–Wapstra mass table [10] to obtain the values of the separation energies.

Our OMP parameterization for either incident neutrons or protons is given the common form

$$\begin{aligned}
&V_V(E) = v_1\big[1 - v_2(E-E_f) + v_3(E-E_f)^2 - v_4(E-E_f)^3\big],\\
&W_V(E) = w_1\frac{(E-E_f)^2}{(E-E_f)^2 + (w_2)^2},\\
&r_V = \text{constant},\\
&a_V = \text{constant},\\
&W_D(E) = d_1\frac{(E-E_f)^2}{(E-E_f)^2 + (d_3)^2}\exp\big[-d_2(E-E_f)\big],\\
&r_D = \text{constant},\\
&a_D = \text{constant},\\
&V_{SO}(E) = v_{so1}\exp\big[-v_{so2}(E-E_f)\big],\\
&W_{SO}(E) = w_{so1}\frac{(E-E_f)^2}{(E-E_f)^2 + (w_{so2})^2},\\
&r_{SO} = \text{constant},\\
&a_{SO} = \text{constant},\\
&r_C = \text{constant},
\end{aligned} \tag{7}$$

where $E_f = E_f^n$ for incident neutrons and $E_f = E_f^p$ for incident protons. An illustration of the E-dependence adopted here for the OMP components is shown in Fig. 1 for neutrons incident on ^{56}Fe.

In general, all parameters change from nucleus to nucleus. Moreover, our OMP analyses have been made separately for incident protons and neutrons. Hence, an OMP for one specific nucleus and projectile is described by the potentials and geometries given in Eq. (7), and the various parameters are given in Tables 3–6 for neutrons and Tables 8, 9 for protons. A more precise definition of specific OMP parameterizations, i.e., in terms of asymmetry-dependent and Coulomb correction components, is outlined in Section 5, where we will provide global nucleon–nucleus potentials. We will now discuss the specific E-dependence of the various potential depths of Eq. (7).

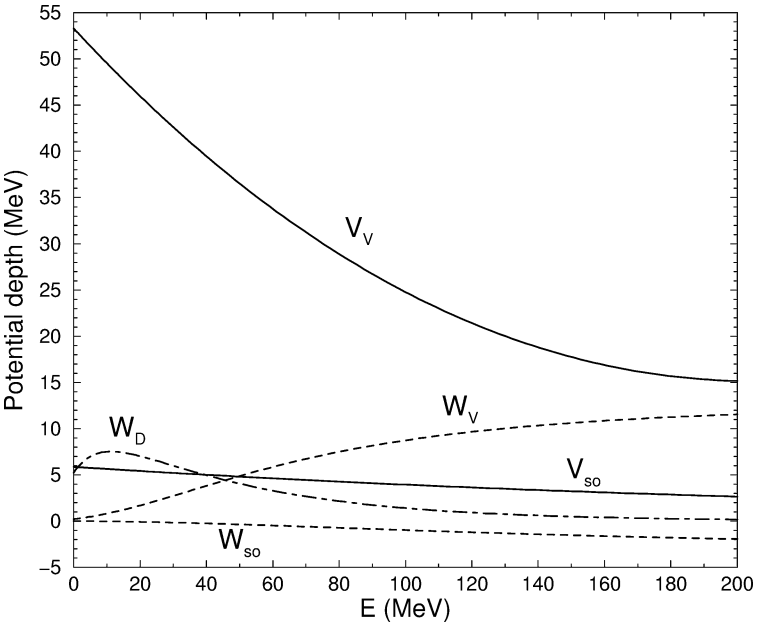

Fig. 1. The various potential well depths as a function of incident (laboratory) energy, see Eq. (7). As an example, the values for neutrons incident on ^{56}Fe are plotted.

It is well known that, due to non-locality, the depth of the real central potential $V_V(E)$ decreases with increasing energy. Instead of a linear E-dependence, often assumed in former OMP analyses for $V_V(E)$, we adopt a polynomial dependence. This choice is dictated by the following considerations. First, the linear E-dependence is a reasonable assumption only in a narrow energy interval, typically from 10 to 40 MeV. Second, we know from dispersive OMP analyses and Dirac phenomenology, which both cover broad energy ranges, that $V_V(E)$ behaves as an exponential function ($V_V(E) \sim \exp[-E]$) for energies up to 140 MeV and as $V_V(E) \sim \log(E)$ at higher incident energies [11,12]. In the early stages of our study we adopted an exponential function to represent $V_V(E)$ below 200 MeV, but that closed form leads to reasonable fits only for $E \leqslant 140$ MeV. The polynomial form in (7) was then considered, since it bears similarity with a truncated Taylor series expansion of the exponential function. The parameters v_2, v_3 and v_4 were then taken uncorrelated, which enabled us to achieve good fits over a larger energy region. Parameter v_4 is equal for all nuclides and has merely been included to keep our predictions under control at about 200 MeV. At higher energies, our functional form will fail since the real central potential is known to become repulsive there.

Similarly, the volume (W_V) and surface (W_D) absorption OMP components are also given a $(E - E_f)$ dependence. The closed forms assigned to the absorptive potentials are suggested by earlier OMP analyses covering broad energy ranges. At low incident energy, the absorption is dominated by the surface component $W_D(E)$. Beyond about 10 MeV, the volume term $W_V(E)$ can no longer be ignored, and at higher energies the absorption is completely dominated by $W_V(E)$. The specific E-dependence adopted for $W_V(E)$ in

Table 3
Neutron OMP parameters. The parameters r_V, a_V, r_D, a_D are given in fm, v_1, w_1, w_2 in MeV, v_2 in MeV^{-1}, v_3 in MeV^{-2}, and v_4 in MeV^{-3}

Nuclide	r_V	a_V	v_1	v_2	v_3	v_4	w_1	w_2	r_D	a_D
^{24}Mg	1.170	0.676	58.0	0.0072	0.000020	7×10^{-9}	12.0	74	1.298	0.540
^{26}Mg	1.172	0.692	58.0	0.0071	0.000019	7×10^{-9}	12.6	74	1.295	0.550
^{27}Al	1.162	0.665	58.8	0.0071	0.000019	7×10^{-9}	12.8	75	1.290	0.538
^{28}Si	1.170	0.668	58.8	0.0070	0.000019	7×10^{-9}	12.5	75	1.294	0.540
^{31}P	1.196	0.675	57.8	0.0072	0.000019	7×10^{-9}	12.4	76	1.293	0.540
^{32}S	1.197	0.678	59.5	0.0072	0.000019	7×10^{-9}	12.6	75	1.302	0.545
^{35}Cl	1.196	0.674	58.4	0.0072	0.000019	7×10^{-9}	12.5	76	1.296	0.540
^{39}K	1.194	0.670	58.8	0.0072	0.000019	7×10^{-9}	12.5	76	1.290	0.535
^{40}Ar	1.188	0.670	56.4	0.0072	0.000019	7×10^{-9}	12.5	76	1.290	0.543
^{40}Ca	1.206	0.676	59.2	0.0072	0.000019	7×10^{-9}	12.4	76	1.295	0.543
^{45}Sc	1.200	0.672	56.6	0.0072	0.000019	7×10^{-9}	12.8	78	1.282	0.532
^{48}Ti	1.185	0.671	56.2	0.0071	0.000019	7×10^{-9}	13.2	76	1.286	0.535
^{51}V	1.180	0.669	56.7	0.0071	0.000019	7×10^{-9}	12.8	78	1.277	0.533
^{52}Cr	1.190	0.667	56.2	0.0071	0.000019	7×10^{-9}	12.8	78	1.282	0.535
^{54}Fe	1.186	0.663	58.2	0.0071	0.000019	7×10^{-9}	13.2	78	1.278	0.536
^{55}Mn	1.183	0.663	56.4	0.0071	0.000018	7×10^{-9}	13.3	74	1.278	0.528
^{56}Fe	1.186	0.663	56.8	0.0071	0.000019	7×10^{-9}	13.0	80	1.282	0.532
^{58}Ni	1.192	0.663	57.8	0.0072	0.000019	7×10^{-9}	13.4	78	1.278	0.536
^{60}Ni	1.193	0.664	57.0	0.0073	0.000020	7×10^{-9}	12.8	78	1.284	0.533
^{59}Co	1.203	0.662	56.2	0.0072	0.000019	7×10^{-9}	12.9	80	1.282	0.532
^{63}Cu	1.200	0.663	56.5	0.0072	0.000019	7×10^{-9}	13.5	80	1.278	0.532
^{65}Cu	1.203	0.663	56.0	0.0072	0.000019	7×10^{-9}	13.5	80	1.278	0.532
^{69}Ga	1.217	0.675	56.0	0.0071	0.000018	7×10^{-9}	13.8	80	1.275	0.535
^{74}Ge	1.220	0.675	54.6	0.0071	0.000018	7×10^{-9}	13.8	80	1.275	0.535
^{75}As	1.215	0.675	54.6	0.0071	0.000018	7×10^{-9}	13.8	80	1.275	0.535
^{79}Br	1.223	0.672	54.0	0.0071	0.000018	7×10^{-9}	13.8	80	1.273	0.528
^{80}Se	1.219	0.675	53.4	0.0071	0.000018	7×10^{-9}	13.6	80	1.273	0.535
^{85}Rb	1.224	0.668	55.0	0.0071	0.000017	7×10^{-9}	14.2	80	1.270	0.530
^{88}Sr	1.220	0.662	55.2	0.0071	0.000017	7×10^{-9}	13.8	80	1.274	0.530
^{89}Y	1.218	0.666	54.8	0.0071	0.000018	7×10^{-9}	14.6	82	1.272	0.530
^{90}Zr	1.218	0.666	54.7	0.0071	0.000017	7×10^{-9}	14.6	80	1.272	0.530
^{91}Zr	1.216	0.666	54.4	0.0071	0.000017	7×10^{-9}	14.6	80	1.276	0.530
^{92}Zr	1.220	0.663	53.4	0.0070	0.000017	7×10^{-9}	14.6	80	1.274	0.528
^{92}Mo	1.222	0.661	55.0	0.0071	0.000018	7×10^{-9}	14.5	80	1.264	0.524
^{93}Nb	1.215	0.663	54.0	0.0070	0.000017	7×10^{-9}	14.6	82	1.274	0.534

Eq. (7) is from Ref [13]. This so-called Brown–Rho function is negligible at low energies, then increases until it finally tends to a constant value. The form is illustrated in Fig. 1. This picture is reasonable for the energy range considered in our work. The functional form for $W_D(E)$ was first used in Ref. [14], and consists of a Brown–Rho function multiplied by an exponentially decreasing function. In dispersion analyses, the power of the Brown–Rho function, as in $W_V(E)$, may in general be equal to any low even integer, e.g., 2, 4 or 6. In our work, we have found that the power of 2 for both $W_D(E)$ and $W_V(E)$ gives the best description for all nuclides.

Table 4
Neutron OMP parameters, continued. The parameters r_{SO}, a_{SO} are given in fm, $d_1, d_3, v_{so1}, w_{so1}, w_{so2}, E_f^n$ in MeV, and d_2, v_{so2} in MeV^{-1}

Nuclide	d_1	d_2	d_3	r_{SO}	a_{SO}	v_{so1}	v_{so2}	w_{so1}	w_{so2}	E_f^n
^{24}Mg	16.2	0.0214	12.5	1.00	0.58	6.0	0.0035	−3.1	160	−11.93
^{26}Mg	15.5	0.0218	13.5	1.00	0.58	6.0	0.0035	−3.1	160	−8.77
^{27}Al	13.0	0.0224	11.5	1.00	0.58	6.1	0.0035	−3.1	160	−10.39
^{28}Si	13.8	0.0216	11.1	1.00	0.58	6.0	0.0040	−3.1	160	−12.83
^{31}P	15.4	0.0214	11.5	1.00	0.59	6.0	0.0040	−3.1	160	−10.12
^{32}S	15.6	0.0215	11.0	1.00	0.59	6.0	0.0040	−3.1	160	−11.84
^{35}Cl	13.3	0.0220	13.5	1.00	0.60	6.1	0.0040	−3.1	160	−11.84
^{39}K	13.3	0.0228	13.5	1.01	0.58	6.1	0.0040	−3.1	160	−10.44
^{40}Ar	12.4	0.0220	12.5	1.01	0.58	6.1	0.0040	−3.1	160	−7.98
^{40}Ca	14.4	0.0205	13.4	1.01	0.60	6.1	0.0040	−3.1	160	−12.00
^{45}Sc	12.5	0.0228	12.6	1.01	0.60	6.1	0.0040	−3.1	160	−10.04
^{48}Ti	12.6	0.0228	13.4	1.01	0.60	6.0	0.0040	−3.1	160	−9.88
^{51}V	12.8	0.0228	13.4	1.00	0.60	6.1	0.0040	−3.1	160	−9.18
^{52}Cr	13.6	0.0215	11.0	1.01	0.60	6.2	0.0040	−3.1	160	−9.99
^{54}Fe	15.4	0.0223	10.9	1.00	0.58	6.1	0.0040	−3.1	160	−11.34
^{55}Mn	13.6	0.0229	11.2	1.00	0.55	6.2	0.0035	−3.1	160	−8.75
^{56}Fe	15.3	0.0211	10.9	1.00	0.58	6.1	0.0040	−3.1	160	−9.42
^{58}Ni	15.4	0.0218	10.5	1.00	0.58	6.1	0.0040	−3.1	160	−10.61
^{60}Ni	15.2	0.0218	10.8	1.00	0.58	6.1	0.0045	−3.1	160	−9.60
^{59}Co	15.6	0.0224	12.7	1.00	0.58	6.1	0.0040	−3.1	160	−8.97
^{63}Cu	14.6	0.0219	11.6	1.00	0.58	6.1	0.0040	−3.1	160	−9.38
^{65}Cu	14.2	0.0219	11.6	1.00	0.58	6.1	0.0040	−3.1	160	−8.49
^{69}Ga	12.8	0.0225	11.0	1.03	0.58	6.2	0.0040	−3.1	160	−8.98
^{74}Ge	12.8	0.0225	11.0	1.03	0.58	6.2	0.0040	−3.1	160	−8.35
^{75}As	12.4	0.0225	11.0	1.03	0.58	6.2	0.0040	−3.1	160	−8.78
^{79}Br	13.6	0.0225	10.5	1.03	0.58	6.2	0.0040	−3.1	160	−9.29
^{80}Se	13.5	0.0225	10.8	1.03	0.58	6.2	0.0040	−3.1	160	−8.31
^{85}Rb	13.5	0.0225	12.6	1.04	0.58	6.2	0.0040	−3.1	160	−9.57
^{88}Sr	13.0	0.0225	13.2	1.05	0.58	6.2	0.0040	−3.1	160	−8.74
^{89}Y	13.6	0.0224	14.2	1.05	0.56	6.2	0.0040	−3.1	160	−9.17
^{90}Zr	13.2	0.0215	14.6	1.05	0.60	6.2	0.0040	−3.1	160	−9.58
^{91}Zr	12.8	0.0215	13.6	1.05	0.60	6.2	0.0040	−3.1	160	−7.91
^{92}Zr	14.2	0.0220	12.5	1.05	0.59	6.2	0.0040	−3.1	160	−7.68
^{92}Mo	14.8	0.0210	12.6	1.05	0.58	6.2	0.0040	−3.1	160	−10.37
^{93}Nb	15.1	0.0215	13.5	1.05	0.59	6.2	0.0040	−3.1	160	−8.03

Finally, the functional forms for $V_{SO}(E)$ and $W_{SO}(E)$ are similar to the E-dependence used in semi-microscopic analyses [1] and of Dirac phenomenology [12], respectively. There is a slight decrease in the real SO potential with increasing energy. Evidence for the imaginary SO potential is difficult to establish at low energies but analyses of proton polarization above 100 MeV indicate that it is certainly present at higher energies. We found it convenient to approximate its well depth by a Brown–Rho function. To obtain a homogeneous notation for the whole OMP, a $(E - E_f)$ dependence is also assigned to the SO potential components in Eq. (7).

Table 5
Neutron OMP parameters. For more details, see the caption of Table 3

Nuclide	r_V	a_V	v_1	v_2	v_3	v_4	w_1	w_2	r_D	a_D
^{94}Zr	1.215	0.658	54.0	0.0071	0.000018	7×10^{-9}	14.5	80	1.264	0.524
^{94}Mo	1.222	0.658	54.2	0.0071	0.000018	7×10^{-9}	14.5	80	1.264	0.524
^{96}Mo	1.222	0.658	53.7	0.0071	0.000018	7×10^{-9}	14.5	80	1.270	0.534
^{98}Mo	1.218	0.658	53.4	0.0071	0.000018	7×10^{-9}	14.5	80	1.270	0.536
^{99}Tc	1.226	0.660	53.7	0.0071	0.000018	7×10^{-9}	14.5	80	1.274	0.534
^{100}Mo	1.220	0.658	53.0	0.0071	0.000018	7×10^{-9}	14.5	80	1.270	0.536
^{103}Rh	1.230	0.660	55.1	0.0071	0.000017	7×10^{-9}	13.8	82	1.266	0.530
^{106}Pd	1.228	0.660	54.6	0.0071	0.000017	7×10^{-9}	13.8	82	1.265	0.530
^{107}Ag	1.232	0.660	54.4	0.0071	0.000017	7×10^{-9}	14.0	82	1.263	0.526
^{114}Cd	1.232	0.665	52.4	0.0070	0.000016	7×10^{-9}	14.4	84	1.260	0.523
^{115}In	1.214	0.662	52.8	0.0071	0.000018	7×10^{-9}	14.5	84	1.272	0.535
^{116}Sn	1.222	0.665	53.6	0.0070	0.000017	7×10^{-9}	14.5	84	1.265	0.524
^{118}Sn	1.225	0.662	52.8	0.0070	0.000017	7×10^{-9}	14.5	84	1.269	0.528
^{120}Sn	1.225	0.662	52.2	0.0070	0.000017	7×10^{-9}	14.5	84	1.269	0.528
^{121}Sb	1.230	0.652	52.6	0.0071	0.000018	7×10^{-9}	14.0	84	1.263	0.524
^{122}Sn	1.225	0.662	51.9	0.0070	0.000017	7×10^{-9}	14.5	84	1.269	0.528
^{123}Sb	1.230	0.652	52.0	0.0071	0.000018	7×10^{-9}	14.0	84	1.263	0.524
^{124}Sn	1.225	0.662	51.8	0.0070	0.000017	7×10^{-9}	14.5	84	1.269	0.528
^{127}I	1.233	0.652	52.0	0.0071	0.000017	7×10^{-9}	14.0	84	1.263	0.524
^{128}Te	1.226	0.652	51.6	0.0071	0.000017	7×10^{-9}	14.0	84	1.263	0.524
^{133}Cs	1.235	0.655	51.7	0.0071	0.000017	7×10^{-9}	13.8	84	1.258	0.520
^{138}Ba	1.235	0.665	52.0	0.0072	0.000017	7×10^{-9}	13.8	84	1.258	0.520
^{139}La	1.230	0.650	52.2	0.0070	0.000017	7×10^{-9}	14.4	86	1.258	0.520
^{140}Ce	1.232	0.646	52.3	0.0070	0.000017	7×10^{-9}	14.4	86	1.254	0.520
^{141}Pr	1.232	0.650	52.8	0.0070	0.000017	7×10^{-9}	14.0	86	1.258	0.520
^{142}Nd	1.230	0.650	52.6	0.0070	0.000017	7×10^{-9}	14.2	86	1.258	0.520
^{144}Nd	1.226	0.658	52.1	0.0070	0.000017	7×10^{-9}	14.4	86	1.258	0.520
^{148}Sm	1.226	0.658	52.0	0.0070	0.000017	7×10^{-9}	14.4	86	1.258	0.520
^{194}Pt	1.237	0.650	51.2	0.0069	0.000015	7×10^{-9}	15.4	88	1.255	0.515
^{197}Au	1.237	0.652	50.0	0.0069	0.000015	7×10^{-9}	15.8	88	1.257	0.508
^{202}Hg	1.246	0.637	50.2	0.0069	0.000015	7×10^{-9}	15.8	88	1.254	0.515
^{206}Pb	1.242	0.646	50.4	0.0069	0.000015	7×10^{-9}	15.6	88	1.246	0.510
^{208}Pb	1.244	0.646	50.6	0.0069	0.000015	7×10^{-9}	15.6	88	1.246	0.510
^{209}Bi	1.248	0.642	50.1	0.0069	0.000015	7×10^{-9}	15.4	88	1.255	0.510

2.3. Compound nucleus contribution and relativistic kinematics

A sound analysis of scattering observables at low energies requires the inclusion of a compound nucleus (CN) contribution. For this, we use the width fluctuation correction model by Moldauer [15], coupled with the Blatt–Biedenharn formalism [16] for angular distributions. For a particular incident energy, all channels that are open to CN emission are included. We include the first several discrete states as competing channels and complement this, for higher excitation energies, by a continuum described by the Gilbert–

Table 6
Neutron OMP parameters, continued. For more details, see the caption of Table 4

Nuclide	d_1	d_2	d_3	r_{SO}	a_{SO}	v_{so1}	v_{so2}	w_{so1}	w_{so2}	E_f^n
^{94}Zr	13.8	0.0212	12.2	1.05	0.58	6.2	0.0040	−3.1	160	−7.34
^{94}Mo	14.8	0.0208	11.2	1.05	0.58	6.2	0.0040	−3.1	160	−8.53
^{96}Mo	15.1	0.0203	10.8	1.05	0.58	6.2	0.0040	−3.1	160	−7.99
^{98}Mo	15.4	0.0203	10.3	1.05	0.58	6.2	0.0040	−3.1	160	−7.29
^{99}Tc	15.1	0.0203	10.4	1.05	0.58	6.2	0.0040	−3.1	160	−7.86
^{100}Mo	15.4	0.0200	10.0	1.05	0.58	6.2	0.0040	−3.1	160	−6.84
^{103}Rh	14.2	0.0206	10.0	1.06	0.60	6.2	0.0040	−3.1	160	−8.16
^{106}Pd	13.8	0.0210	10.0	1.06	0.60	6.2	0.0040	−3.1	160	−8.05
^{107}Ag	13.0	0.0225	12.6	1.06	0.60	6.2	0.0040	−3.1	160	−8.41
^{114}Cd	13.6	0.0225	11.0	1.06	0.60	6.2	0.0040	−3.1	160	−7.59
^{115}In	13.8	0.0222	12.0	1.07	0.60	6.3	0.0040	−3.1	160	−7.91
^{116}Sn	15.0	0.0206	12.3	1.06	0.60	6.2	0.0040	−3.1	160	−8.25
^{118}Sn	14.8	0.0206	13.0	1.07	0.60	6.2	0.0040	−3.1	160	−7.91
^{120}Sn	14.6	0.0206	13.0	1.07	0.60	6.2	0.0040	−3.1	160	−7.64
^{121}Sb	14.0	0.0210	13.2	1.07	0.60	6.2	0.0040	−3.1	160	−8.02
^{122}Sn	14.3	0.0206	13.0	1.07	0.60	6.2	0.0040	−3.1	160	−7.38
^{123}Sb	14.0	0.0206	13.2	1.07	0.60	6.2	0.0040	−3.1	160	−7.72
^{124}Sn	14.0	0.0206	13.0	1.07	0.60	6.2	0.0040	−3.1	160	−7.38
^{127}I	14.0	0.0218	13.2	1.07	0.60	6.2	0.0040	−3.1	160	−7.98
^{128}Te	14.8	0.0216	12.0	1.07	0.60	6.2	0.0040	−3.1	160	−7.42
^{133}Cs	14.0	0.0220	13.0	1.08	0.59	6.4	0.0040	−3.1	160	−7.94
^{138}Ba	13.8	0.0220	13.0	1.08	0.59	6.4	0.0040	−3.1	160	−6.67
^{139}La	14.0	0.0220	14.0	1.08	0.59	6.4	0.0040	−3.1	160	−6.97
^{140}Ce	14.0	0.0220	14.0	1.08	0.59	6.4	0.0040	−3.1	160	−7.32
^{141}Pr	14.8	0.0220	14.5	1.08	0.59	6.4	0.0040	−3.1	160	−7.62
^{142}Nd	14.5	0.0206	13.2	1.08	0.59	6.4	0.0040	−3.1	160	−7.97
^{144}Nd	15.0	0.0206	12.7	1.08	0.59	6.4	0.0040	−3.1	160	−6.78
^{148}Sm	15.2	0.0206	12.7	1.08	0.59	6.4	0.0040	−3.1	160	−7.01
^{194}Pt	14.2	0.0180	12.2	1.10	0.60	6.6	0.0035	−3.1	160	−7.01
^{197}Au	12.7	0.0180	13.2	1.10	0.60	6.6	0.0035	−3.1	160	−7.29
^{202}Hg	13.2	0.0180	12.2	1.10	0.60	6.6	0.0035	−3.1	160	−6.88
^{206}Pb	13.8	0.0180	14.3	1.08	0.57	6.6	0.0035	−3.1	160	−7.42
^{208}Pb	13.8	0.0180	13.8	1.08	0.57	6.6	0.0035	−3.1	160	−5.65
^{209}Bi	13.8	0.0180	13.8	1.08	0.57	6.6	0.0035	−3.1	160	−6.03

Cameron level density formula [17]. The level density parameters are taken from Ref. [18]. The analysis of shape + compound elastic scattering was iteratively performed, since the transmission coefficients required for the CN cross section calculations are derived from potentials that describe the shape elastic component.

For a consistent analysis at all energies we have employed the relativistic Schrödinger equation throughout. In practice, this means that if one would apply our parameters in a calculation without relativistic kinematics, significant deviations from the correct results should be expected above several tens of MeV. All our optical model calculations are performed with the true masses of the projectile and target expressed in atomic mass units.

Table 7
$\sigma(\theta)/\sigma_{\mathrm{Ruth}}$ and $A_y(\theta)$ database for proton elastic scattering

Target	Ref.	Energy (MeV)	Ref.	Energy (MeV)
^{27}Al	[221]	17	[225]	141
	[222]	28	[226]	156
	[223]	35.2	[227]	160
	[224]	61.4	[228]	180
^{28}Si	[229]	17.8	[232]	65
	[222]	28	[233]	79.1, 99, 198.1
	[230]	30.4	[234]	134.2
	[231]	40	[235]	180
^{40}Ca	[236]	14.5, 18.6, 21	[232]	65
	[237]	16	[241]	75, 152
	[238]	26.3, 30.3	[234]	80.2, 160, 181
	[239]	40	[242]	135.1
	[240]	45.5	[226]	156
	[224]	61.4	[243,244]	201.4
^{54}Fe	[245]	9.7	[250]	19.6
	[246]	11	[251]	30.4
	[247]	12	[223]	35.0
	[237]	16	[252]	40
	[248]	17.2, 20.4, 24.6	[253]	49.4
	[249]	18.6	[232]	65
^{56}Fe	[246]	11, 11.7	[256]	30.3
	[254]	14.5	[223]	35.2
	[248]	15.3, 17.2, 20.4, 24.6	[252]	40
	[237]	16	[253]	49.4
	[249]	18.6	[232]	65
	[255]	19.1	[226]	156
$^{\mathrm{nat}}$Fe	[257]	155	[228]	182
	[258]	179		
^{58}Ni	[259]	10.7, 14.5, 15.4	[262]	35
	[246]	12	[263]	39.6
	[237]	16	[239]	40
	[221]	17.8	[224]	61.4
	[249]	18.6	[232]	65
	[248]	20.4, 24.6	[264]	100
	[260]	21.3	[265]	160
	[261]	22	[266]	178
	[238,256]	30.3	[267]	200
$^{\mathrm{nat}}$Ni	[268]	17.3	[257]	155
^{60}Ni	[259]	14.5, 15.4	[238,256]	30.3
	[237]	16	[263]	39.6
	[249]	18.6	[239]	40
	[248]	20.4, 24.6	[232]	65

(*continued on next page*)

Table 7 (*Continued*)

Target	Ref.	Energy (MeV)	Ref.	Energy (MeV)
^{90}Zr	[245]	9.7, 12.7, 14.7	[253]	49.4
	[237]	16	[224]	61
	[269]	18.8	[232]	65
	[270]	20.0	[234,242]	79.8, 135.1, 160, 180
	[271]	22.5	[264]	100.4
	[272]	30	[226]	156
	[239]	40		
^{120}Sn	[245]	9.7	[274]	40
	[237]	16	[264]	100.4
	[273]	20.4, 24.6	[226]	156
	[256]	30.3	[265]	160
^{208}Pb	[275]	11, 12, 13	[224]	61.4
	[237]	16	[232]	65
	[276]	21, 24.1, 35, 45, 47.3, 185	[242]	79.9, 100.4, 121.2
	[238]	26.3	[234]	79.9, 185
	[256,277]	30.3	[226]	156
	[239]	40	[265]	161
	[253]	49.4	[278–280]	201
^{209}Bi	[237]	16	[241]	78, 153
	[281]	57	[226]	155
	[232]	65		

Table 8
Proton OMP parameters. For more details, see the caption of Table 3

Nuclide	r_V	a_V	v_1	v_2	v_3	v_4	w_1	w_2	r_D	a_D
^{27}Al	1.162	0.665	62.4	0.0070	0.000017	7×10^{-9}	15.2	75	1.290	0.510
^{28}Si	1.170	0.668	62.6	0.0071	0.000018	7×10^{-9}	15.0	75	1.294	0.510
^{40}Ca	1.206	0.676	61.6	0.0072	0.000018	7×10^{-9}	14.0	76	1.295	0.535
^{54}Fe	1.186	0.663	63.0	0.0072	0.000018	7×10^{-9}	15.2	78	1.282	0.545
^{56}Fe	1.186	0.663	64.2	0.0072	0.000018	7×10^{-9}	15.4	80	1.282	0.555
^{58}Ni	1.192	0.663	63.8	0.0073	0.000017	7×10^{-9}	15.4	78	1.282	0.550
^{60}Ni	1.193	0.664	64.2	0.0073	0.000017	7×10^{-9}	15.2	78	1.284	0.560
^{62}Ni	1.193	0.664	64.0	0.0073	0.000018	7×10^{-9}	15.4	78	1.284	0.555
^{63}Cu	1.200	0.663	63.2	0.0073	0.000019	7×10^{-9}	15.5	80	1.284	0.550
^{64}Ni	1.200	0.663	64.8	0.0073	0.000018	7×10^{-9}	15.2	80	1.278	0.565
^{90}Zr	1.218	0.666	63.3	0.0075	0.000019	7×10^{-9}	15.6	80	1.272	0.585
^{120}Sn	1.225	0.662	65.5	0.0077	0.000019	7×10^{-9}	16.0	84	1.269	0.605
^{208}Pb	1.244	0.646	67.2	0.0079	0.000020	7×10^{-9}	16.6	88	1.246	0.615
^{209}Bi	1.248	0.642	66.8	0.0079	0.000019	7×10^{-9}	16.6	88	1.255	0.615

3. Optimization of optical model parameters

From the large number of phenomenological optical model studies that have been performed in the past, one can infer that the determination of a set of optical model

Table 9
Proton OMP parameters, continued. The parameter r_C is given in fm. For more details, see the caption of Table 4

Nuclide	d_1	d_2	d_3	r_{SO}	a_{SO}	v_{so1}	v_{so2}	w_{so1}	w_{so2}	r_C	E_f^p
^{27}Al	14.6	0.0224	11.5	1.00	0.58	6.0	0.0035	−3.1	160	1.329	−9.93
^{28}Si	14.6	0.0216	11.1	1.00	0.58	6.0	0.0035	−3.1	160	1.324	−7.16
^{40}Ca	15.2	0.0205	13.4	1.01	0.60	6.1	0.0040	−3.1	160	1.285	−4.71
^{54}Fe	15.4	0.0223	10.9	1.00	0.58	6.1	0.0040	−3.1	160	1.264	−6.96
^{56}Fe	16.0	0.0211	10.9	1.00	0.58	6.1	0.0040	−3.1	160	1.261	−9.42
^{58}Ni	15.2	0.0218	10.5	1.00	0.58	6.1	0.0040	−3.1	160	1.259	−5.79
^{60}Ni	16.0	0.0218	10.8	1.00	0.58	6.1	0.0045	−3.1	160	1.258	−7.17
^{62}Ni	16.4	0.0216	11.2	1.00	0.58	6.1	0.0040	−3.1	160	1.256	−8.63
^{63}Cu	16.0	0.0219	11.6	1.00	0.58	6.1	0.0040	−3.1	160	1.255	−6.92
^{64}Ni	16.5	0.0216	11.2	1.00	0.58	6.1	0.0040	−3.1	160	1.254	−10.00
^{90}Zr	18.1	0.0215	14.6	1.05	0.60	6.2	0.0040	−3.1	160	1.240	−6.80
^{120}Sn	19.3	0.0206	13.0	1.07	0.60	6.2	0.0040	−3.1	160	1.231	−8.23
^{208}Pb	19.5	0.0180	13.8	1.08	0.57	6.6	0.0035	−3.1	160	1.220	−5.90
^{209}Bi	19.4	0.0180	13.8	1.08	0.57	6.6	0.0035	−3.1	160	1.220	−4.39

parameters is considered to be successful only if *all* of the following three criteria are satisfied:

(i) *Physically meaningful parameters*. From general properties of nuclei and microscopic optical model calculations one can estimate the allowed range for the parameters determined in a phenomenological approach,
(ii) *The parameters must satisfy a numerical optimization criterion*. Usually this is related to a minimal value of χ^2, or better, χ^2/N, where $N = P - F$ is the number of degrees of freedom, with P the number of experimental data points and F the number of freely varying parameters, and
(iii) *A good visual fit*. This means that, irrespective of the χ^2 values, the comparison between theory and experiment is satisfactory when judged by eye, for all different types of observables (angular distributions for elastic scattering cross sections and analyzing powers, total cross sections) simultaneously.

Of these criteria, the best consensus seems to exist for case (i), see, e.g., Ref. [19]. Also criterion (iii) is, albeit somewhat subjective, easily imaginable. It is the unambiguous definition of the optimization criterion (ii) which is very difficult, if not impossible, to judge. Moreover, even if such an optimization criterion is invoked, the obtained result often turns out to be in disagreement with the subjective criterion (iii), and in some case also with (i). This occurs especially when only a few experimental data sets are available. This outstanding problem of the phenomenological optical model was already addressed by Satchler [20], who concluded that "Sometimes, if χ^2/N is large, a subjective judgment ('by eye') of the goodness of fit may have, in an ill-defined way, more significance than χ^2 itself. Similar remarks apply if the minimum χ^2 corresponds to parameter values that are obviously unphysical".

We will now enumerate the problems one encounters when attempting to solve the optical model problem completely numerically. We do this to justify our computational steering technique, which we will outline thereafter. Finally, we will establish the complete optimization approach that we have used for our parameter determination.

3.1. Numerical goodness-of-fit estimator

3.1.1. The optimization problem

In 1963, Perey [21] gave a systematic discussion of the optimization problem for phenomenological optical model analyses of nuclear scattering. He concluded that for the optical model χ^2 may have little meaning as an estimator of the goodness-of-fit. Nevertheless, in the absence of any reasonable and full-proof alternative, that method has generally been adopted to obtain "best-fit" OMPs. Since our optimization method also uses the χ^2 method to some extent (to get the best initial parameters), we will here list some of the problems that will be encountered when determining OMP parameters purely numerically:

(i) *Phasing of elastic angular distributions*. Unless it is close to the value 1, χ^2 does not give an indication of the oscillatory behaviour of the calculated curve relative to the measured data. Hence, a result found for minimal $\chi^2 > 1$ may exhibit, when judged visually, theoretical angular distributions which are clearly out of phase with their experimental counterparts.

(ii) $\chi^2 \gg 1$. This was first reported by Perey. When χ^2 is large, a change in χ^2 does not correspond to the expected associated visual change. In other words, if χ^2 is large, a decrease of χ^2 does not necessarily mean a better subjective, visual result. Among others, this is related to the aforementioned phasing problem. When χ^2 is small, this correspondence is much better.

(iii) *Experimental uncertainty*. When constructing optical models over a large energy range, one does not consider only one measurement or even one consistent set of measurements. Instead one makes use of completely uncorrelated experimental data sets, measured at different laboratories with different methods. Even though the statistical errors usually are reported, the systematical errors are often difficult to establish. The optimization procedure is very sensitive to these errors, which means that even a slightly incorrect error estimation can easily vitiate an automated fitting procedure.

(iv) *Distribution of experimental data sets over energy for one type of observable*. In a phenomenological approach, the obtained OMP parameters for each nucleus obviously depend on the included experimental data sets. If these happen to be oddly concentrated in energy, an automated optimization procedure will be biased towards the region where the data are clustered. If for an adjacent nucleus the available measurements are differently distributed over energy, one may find a completely different set of parameters. From physical considerations, one expects that both systems should be described by similar optical models. Hence, information from neighboring nuclei or a global optical model needs to be taken into account to guide the parameterization for the nucleus under study. It is however, very difficult to

devise a computational method to constrain the parameters consistently using this information, because the parameters *do* actually vary from nucleus to nucleus, and in an unpredictable manner.

(v) *Weight of different types of observables*. A good optical model should simultaneously give a good description of angular distributions for elastic scattering cross sections and analyzing powers, total (reaction) cross sections, and for low-energies the s- and p-wave strength functions S_0 and S_1 and potential scattering radius R'. One could define one average χ^2 for each type of observable, but even then the problem of how to weight them in an overall numerical optimization in which all observables need to be fitted together, remains. An extra complication is that the total cross sections usually are measured at energies different from those for the angular distributions $d\sigma/d\Omega$ and the analyzing powers A_y.

(vi) *The validity of the optical model itself*. Although a physical rather than a numerical problem, it has an impact on the parameter search. The conventional spherical optical model probably is inadequate to describe scattering from nuclides known to be strongly deformed and especially if there is strong channel coupling as a result. It may not describe cases for which particular shell effects are needed to describe reactions. Both such phenomena can have a significant impact on the final parameters found using a spherical OMP to analyze associated scattering data.

These considerations lead us to the statement that it is impossible to define a unique goodness-of-fit estimator for the phenomenological optical model that consistently gives numerical, physical and subjective (i.e., visual) satisfaction simultaneously. Even for cases where the systematic errors are completely known, which is very rare, there is always a point in the optimization scheme where one needs to introduce an arbitrary weighting, not only for one type of observable at different energies but also for different types of observables. This weighting is then subjective, i.e., it is usually only accepted if the final results come up to the expectations when judged by eye.

3.1.2. Simulated annealing

Part of our quest for the best OMP parameters is based on automatic χ^2 optimization. We have constructed an optical model optimization program written around ECIS-97 [6]. In fact, we have integrated ECIS-97 in this code as a subroutine and suppressed its input and output to maximize the speed of the optical model calculations. In this way, we can typically perform 500 ECIS calculations per second. The search scheme utilizes simulated annealing [22]; a global optimization method that distinguishes between different local optima.

In simulated annealing, starting from an initial point and evaluated function, the algorithm makes a change in variable and re-evaluates the function. The algorithm then accepts any “downhill” step and the process is repeated. An “uphill” step may be accepted as well, an aspect of the process that enables it to escape from local optima. This “uphill” decision is made using a Monte Carlo criteria with “temperature” and the size of the “downhill” move assessed a probabilistic manner. The smaller the “temperature" and the size of the “downhill” move, the more likely that move will be accepted. If the trial is accepted, the algorithm moves on from that point. If it is rejected, another point is chosen

instead for a trial evaluation. As the optimization process proceeds, the algorithm closes in on the global optimum. Since the algorithm makes very few assumptions regarding the function to be optimized, it is quite robust with respect to non-quadratic surfaces. For the simulated annealing optimization, we have used the SIMANN program by Goffe et al. [22], who developed it for econometric applications. We have found it competitive, if not superior, to multiple restarts of conventional optimization routines for the optical model optimization problem. For a certain initial temperature, a user-defined number of function evaluations is tried. Then, the temperature is reduced, and starting from the previously found minimum, the search continues. The degree of robustness of the search can be adjusted by the user. The temperature, the number of function trials for each temperature and the temperature reduction factor are the crucial parameters in a simulated annealing search. It determines the probability that the function to be minimized escapes from a local minimum, and also how quickly a final optimum is reached. We have minimized the total number of trial evaluations by investigating the sensitivity of the optical model problem to the parameters of the simulated annealing program. Nevertheless, the part of the optimization that is done by χ^2 minimization takes about 2 million ECIS calculations for a typical nucleus. We estimate the total number of ECIS calculations that lie at the basis of this paper, i.e., including local and global OMPs, between 1 and 2 billions. The automatic optimization of local and global OMP parameters has been done in iteration with the visual method that will be discussed later.

3.1.3. Grid search

For the nuclides for which enough experimental data is available, we have used a grid search as the initial step to obtain the OMP parameters. The basic idea behind the grid search method, developed in Refs. [1,14,23], is that the search for the energy *independent* geometry parameters is separated from the search for the energy *dependent* functional form of the potential depths. In this way, one can avoid, to some extent, continuous parameter ambiguities such as $W_D a_D = \text{constant}$ and $V r_V^2 = \text{constant}$. We will now outline how we have used grid search in our work. For the nucleus under study, our search includes all experimental elastic scattering angular distributions $d\sigma/d\Omega$, total cross sections on a reasonable (logarithmically equidistant) energy grid, and analyzing powers $A_y(\theta)$ by means of the product $A_y(\theta)d\sigma/d\Omega$. We fix all geometry parameters r_V, a_V, r_D, a_D, r_{SO}, and a_{SO} to reasonable starting values, e.g., those of a preliminary version of our global optical model. Then for each incident energy for which experimental observables exist, we search for those values of the potential depths V_V, W_V, W_D, V_{SO}, and W_{SO} that have the minimal χ^2 for that particular initial set of geometry parameters. Summed over incident energies, this gives the total χ^2 for the geometry parameter set. Next, we let r_V vary around its starting value in steps of 0.04 fm and repeat the search for all incident energies. In this way, we determine the r_V value for which the sum over minimal χ^2 values is itself minimal. Then, we repeat this with the other 5 geometry parameters. We then return to r_V, now using steps of 0.01 fm, and the whole procedure is repeated a few times until we have obtained a precision of 0.001 fm for each geometry parameter. The final result of the grid search is thus one set of parameters r_V, a_V, r_D, a_D, r_{SO}, and a_{SO} and several sets of "best-fit" parameters V_V, W_V, W_D, V_{SO}, and W_{SO}, one set for each incident energy. When plotted against energy, the potential depths belonging to this set of geometry

parameters show a behaviour for which suitable functional forms can be estimated, and these are the ones given in Eq. (7). Grid search is a powerful method to investigate the energy behaviour of the various potential depths, although we were of course able to anticipate some of our functional forms from previous works. Theoretically, the final result should be the same if we would start with a general search of all geometry parameters and all individual parameters that construct the functional forms for the potential depths. However, the optimization problems mentioned in the previous section imply that this is not guaranteed. The problem should be tackled on a more step-by-step basis. Indeed, we can confirm that the separation of the search into a geometry part and a potential depth part leads to better constrained results than allowing a fully free search from scratch. Only after we determined the final grid search values for the geometry parameters and the parameters (v_1, v_2, etc.) for the potential depths, have we performed a final "half-constrained" OMP search for all parameters, since the chance of being caught in a local minimum was reduced by the grid search. In this way, we found our final answer for the χ^2 part of the optimization which was then used as a starting point in our visual estimation.

3.2. Visual goodness-of-fit estimator

Although the problems of using χ^2 as a measure may be obvious, they do not give guidance to a solution for the optimization problem. Indeed, in the past, a purely numerical optimization problem simply *had* to be adopted in the absence of an alternative approach. Varner et al. [4], in their extensive global optical model study, noted that "the procedure had to search without human guidance, more than a dozen correlated parameters in a highly non-linear model, since we know of no way that a human can compare data and predictions in 292 angular distributions and reliably decide how to change the global parameters". However, in the past decade computer power has increased by several orders, enabling us to use an approach that actually does rely on direct human guidance.

Realizing that the quality of an OMP is eventually always judged by visual estimates, a method was developed at ECN [5] to obtain a good visual fit directly by means of so-called computational steering. We used this in combination, and iteratively, with numerical optimization to arrive at the best results. The means to perform the visual fitting is a software package called ECISVIEW, a graphical interface built around the optical model code ECIS-97 [6]. The basic purpose of ECISVIEW is the possibility to change optical potential parameters interactively, with the keyboard or the mouse, and to display the calculated curves, together with the experimental data, in real time on the computer screen.

ECISVIEW links to the input and output files of ECIS-97, while holding ECIS-97 itself in the background in a wait state until the command to perform calculations is given. When the user changes OMP parameters (with the mouse or the keyboard via several dialog boxes as in a usual X-windows environment), ECISVIEW creates the associated ECIS input file and initiates ECIS-97 calculations. The whole process leading to a graph on the screen is very fast; seemingly instantaneous to the observer.

The data from a typical example is illustrative. Consider a nucleus for which angular distributions at 10 different energies and total scattering cross sections for many energies up to 200 MeV have been measured. With a run of ECISVIEW, those 10 experimental angular distributions and, in a separate panel, the experimental total cross section, are displayed

together with the theoretical curves calculated by some initial OMP parameterization. When a parameter is changed, e.g., the radius r_V, within about 0.2 seconds 10 new calculated angular distributions are displayed with the data. Within about 2 seconds a new calculated total cross section is plotted for the whole energy range. The analyzing powers also can be displayed in a separate panel. One of the key features of ECISVIEW is that one can specify *any* functional form of the potential parameters; be it a function of energy, Z and A, or of user-defined parameters. That flexibility and speed enables one to try various functional forms for the parameters, and so seek insights about the OMP that would otherwise be unattainable. In fact, our final OMP (7) was obtained with this approach, of course in combination with the grid search that we described previously.

At a certain point in the optimization process, visual judgment of all observables simultaneously often suggests which parameters need to be changed. For example, it is known that at low incident energy an underestimation of angular distributions at backward angles indicates a surface absorption that is too strong. If this underestimation occurs only locally in energy, experience indicates which of the parameters that drive $W_D(E)$ needs to be changed. Another important example is the maximum in the proton total reaction cross section at a few tens of MeV. The OMP result for this peak is known to be very sensitive to the imaginary surface diffusivity a_D, and less sensitive to $W_D(E)$. Accordingly, we interactively vary a_D until the proton reaction cross section is satisfactorily reproduced and simultaneously "repair" the backward angular distributions by adjusting W_D. Hence, we find that by simultaneously fitting the elastic angular distributions and the proton reaction cross section data, we can circumvent the well-known ambiguity $W_D a_D = \text{constant}$.

For completeness we note that compound nucleus contributions [15] are included and one can also change the level density parameters to study their influence on the calculated results. Other features are described in Ref. [5].

Finally, for nuclides for which enough experimental data exists, comparison of our OMPs visually obtained with those obtained by a purely automatic optimization through grid search and using χ^2/N per type of observable as the quality criterion lead to differences of no more than 10%, so justifying use of the computational steering method. Of course, in all cases, our final OMPs were the result of an iteration of grid search, visual optimization and global OMP construction. However, we did start with a nucleus for which a lot of experimental data existed. The resulting parameterization then heavily influenced that we chose for neighboring nuclides with more restricted experimental databases. In that way, all of our parameters could be kept reasonably close to a global average.

4. Results for local neutron and proton OMPs

The complete experimental database for our work is detailed in Tables 1, 2 and 7 for incident neutrons and protons, respectively. This database, together with the optimization method outlined in Section 3 has yielded a suite of local OMPs. With our iterative approach, we have been able to unify many of the parameters (mostly the geometry) for neutrons and protons, which puts a heavy constraint on our OMPs. For each individual isotope, the OMP is described by Eq. (7) with the parameters given in Tables 3–6 for incident neutrons and in Tables 8, 9 for incident protons. Results are available in

computational format [9] as well. In this section, we discuss the performance of the OMPs when compared with experimental data. Since global optical models will be the topic of Section 5, the following discussion is restricted to the results from local OMP analyses.

4.1. Presentation of the results

This paper contains a comprehensive collection of figures in which experimental data (represented by symbols) are compared with the local OMP (represented by solid lines) and the global OMP (represented by dashed lines). The experimental data tables indicate whether isotopes or natural samples are used.

For neutron total cross sections, as, e.g., in Fig. 2, the curves and data points at the top represent true values, while the others are offset by factors of 2, 4, 8, and 16. The experimental cross sections below 4 MeV have been averaged over logarithmically equidistant energy bins in order to reduce the number of points.

For neutron elastic differential cross sections, as, e.g., in Fig. 3, the incident laboratory energies are indicated in MeV. The curves and data points at the top represent true values, while the others are offset by factors of 10, 100, etc. A similar representation is used for proton elastic differential cross sections, as, e.g., in Fig. 33, although here the differential cross sections are presented as ratios to the Rutherford cross sections.

For analyzing powers, as, e.g., in Fig. 7, the curves and data points at the top represent true values, while the others are offset by factors of 2, 4, 6, etc.

4.2. Neutron-induced data

For neutrons, our analysis is based on about 800 elastic scattering angular distributions $d\sigma/d\Omega$, 40 analyzing power angular distributions $A_y(\theta)$, and 140 total cross section sets σ_T. A significant part of these data are compared with the theoretical results in Figs. 2–31. The references for the experimental data are listed in Tables 1, 2.

A few general statements can be made that apply to the whole mass range. Considering the fact that only a modest number of adjustable parameters per nucleus is used with a single functional form for the OMP, the overall agreement with experimental data is very good. First of all, for σ_T *above* 5 MeV, the deviation of the local OMP prediction from experiment is on average within 1%, and it is seldom more than 2%. Almost all of the measured σ_T values above 5 MeV that we show are from just two experiments performed at Los Alamos National Laboratory [24,25]. The experimental uncertainties of these measurements are of the order of 1%. We believe this is the first time that such an excellent description over such large mass and energy ranges is obtained within the optical model approach. Note that the fits of σ_T, shown in Figs. 2, 8, 15 and 26 extend to 250 MeV, instead of our advertised validity limit of 200 MeV. Indeed, the v_4 parameter is only included in our parameterization (7) to find good results for the total cross section in the energy region 180–250 MeV. This is a purely phenomenological effect. The Woods–Saxon form factor for $\mathcal{V}_V$ is inadequate in this energy region, which would be more clearly revealed by the more exclusive neutron differential data. However, such data are lacking in this energy region.

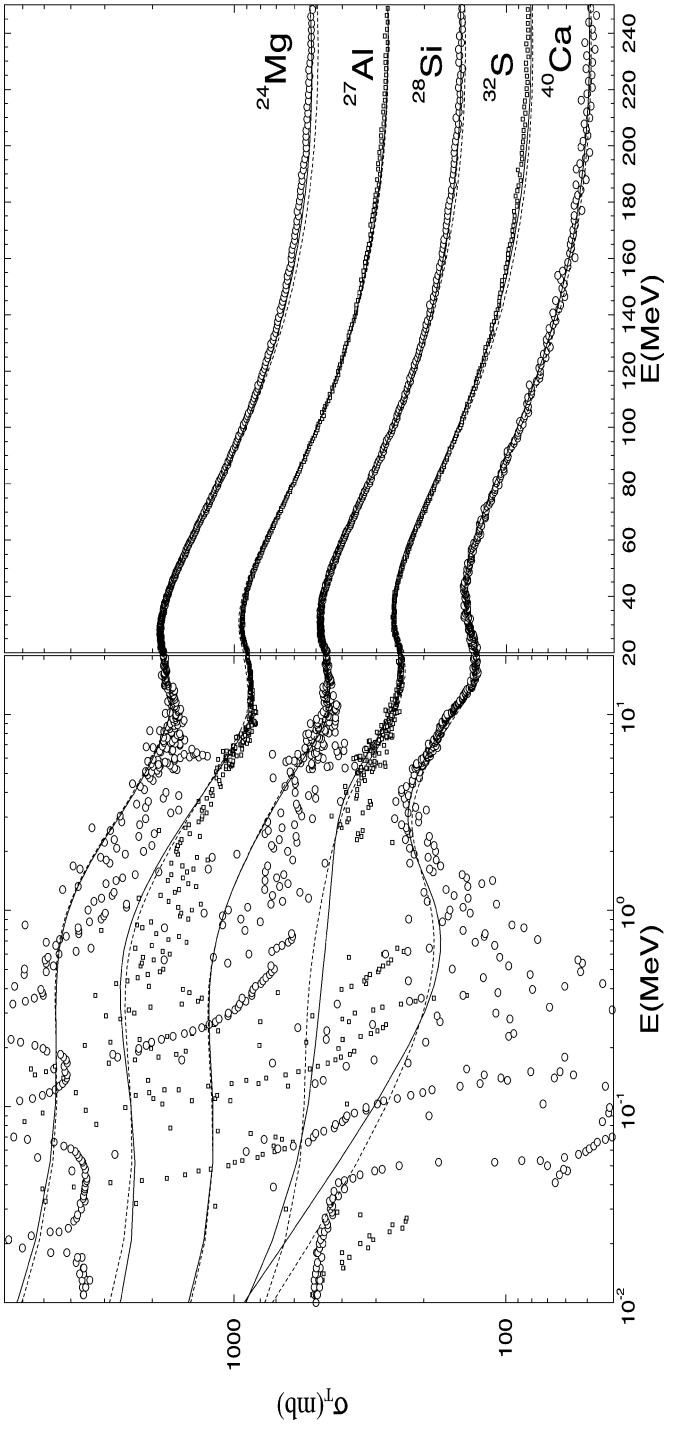

Fig. 2. Comparison of predicted neutron total cross sections and experimental data, for nuclides in the Mg–Ca mass region, for the energy range 10 keV–250 MeV. For more details, see Section 4.1.

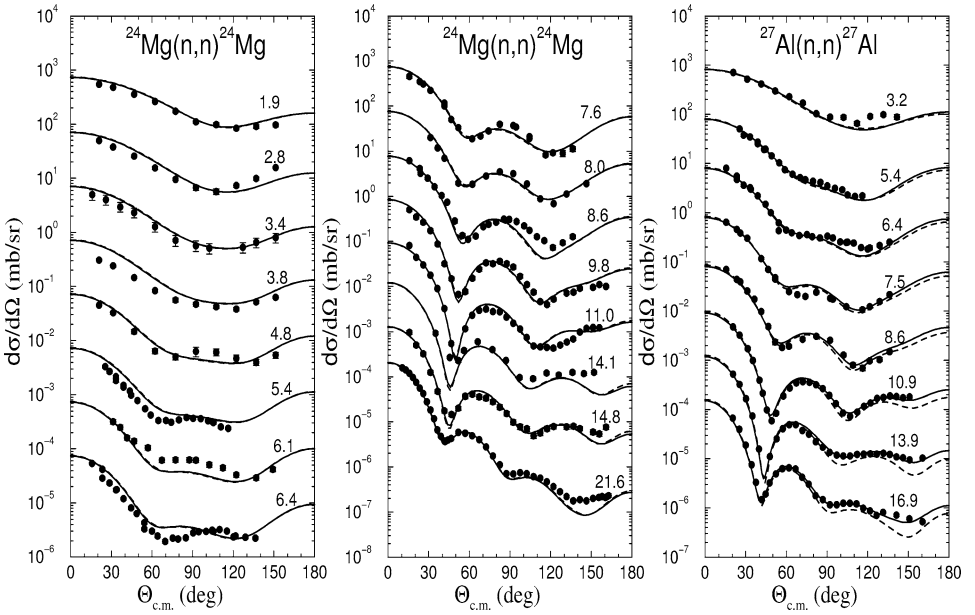

Fig. 3. Comparison of predicted differential cross sections and experimental data, for neutrons scattered from ^{24}Mg and ^{27}Al. For more details, see Section 4.1.

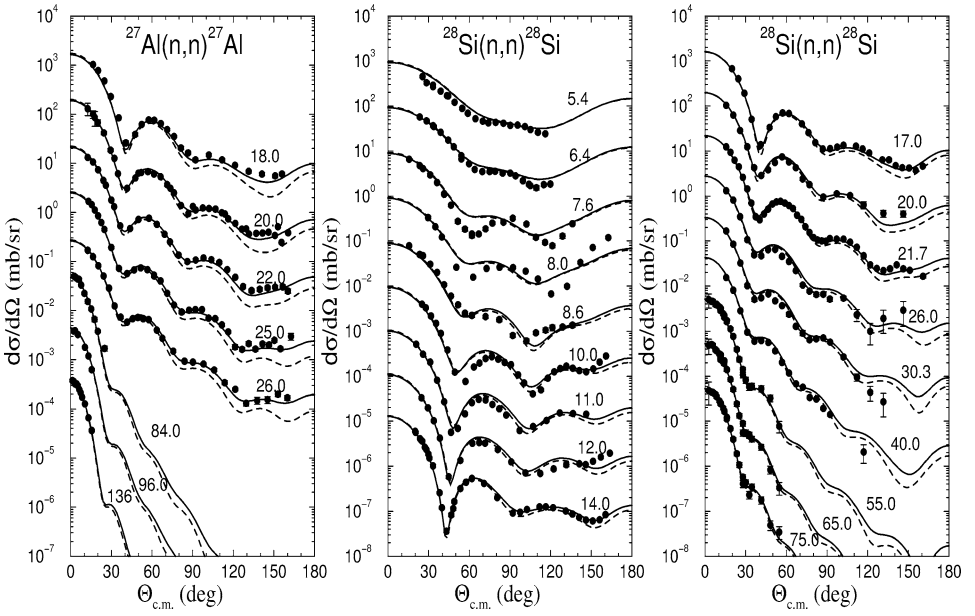

Fig. 4. Comparison of predicted differential cross sections and experimental data, for neutrons scattered from ^{27}Al and ^{28}Si. For more details, see Section 4.1.

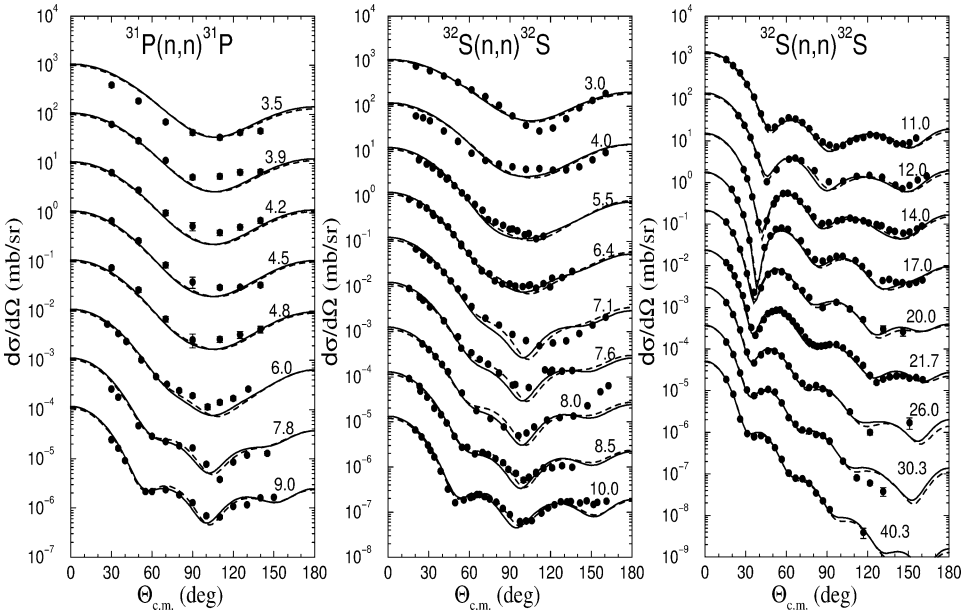

Fig. 5. Comparison of predicted differential cross sections and experimental data, for neutrons scattered from ^{31}P and ^{32}S. For more details, see Section 4.1.

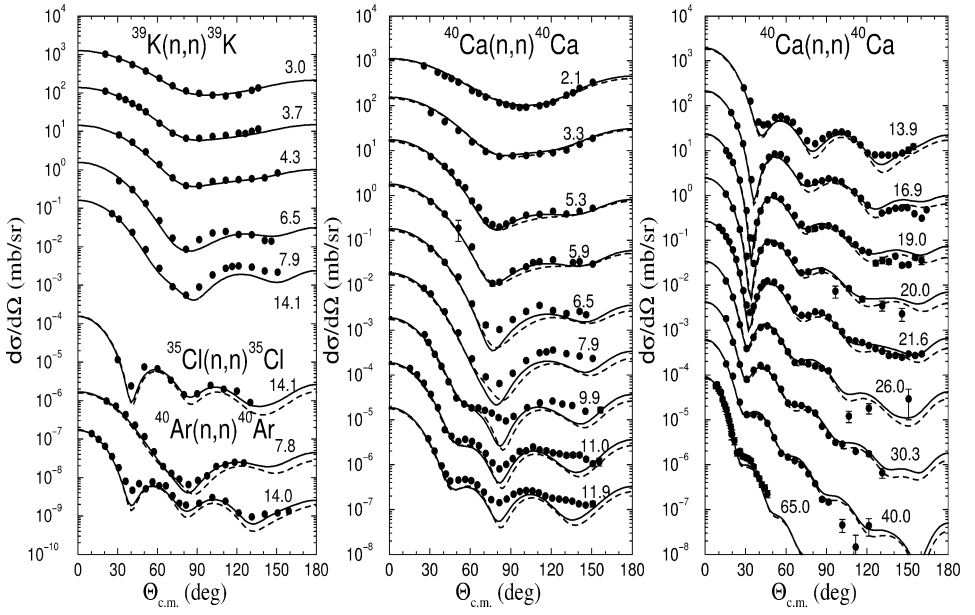

Fig. 6. Comparison of predicted differential cross sections and experimental data, for neutrons scattered from ^{35}Cl, ^{39}K, ^{40}Ar, and ^{40}Ca. For more details, see Section 4.1.

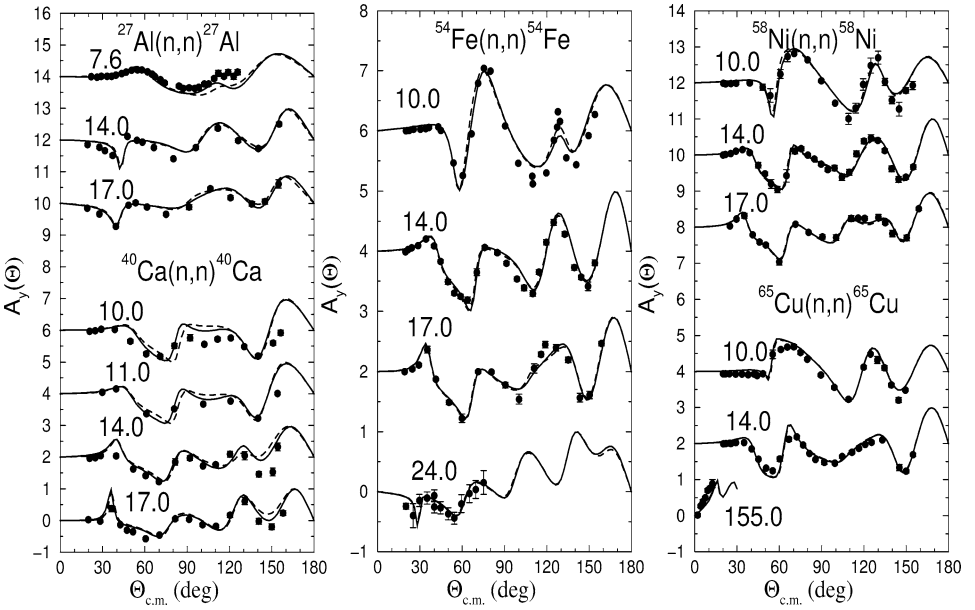

Fig. 7. Comparison of analyzing powers and experimental data, for neutrons scattered from ^{27}Al, ^{40}Ca, ^{54}Fe, ^{58}Ni, and ^{63}Cu. For more details, see Section 4.1.

The general description of $d\sigma/d\Omega$ is also good over the whole energy range, with a globally adequate contribution of the CN process. Nevertheless, there are some local deviations from the experimental data that deserve attention. These will be described in the following discussion, which has been divided into several regional mass ranges. In total, local OMPs have been constructed for $24 \leqslant A \leqslant 148$ and $194 \leqslant A \leqslant 209$. Nuclides outside this range are too light or too deformed to be described by our approach. Also, one has to bear in mind that the final results are always a trade-off between σ_T, $d\sigma/d\Omega$, and A_y data, i.e. we have strived to divide the quality of fit equally over these observables.

4.2.1. Mg, Al, Si, P, S, Cl, Ar, K *and* Ca *targets*

The results for σ_T for some of these targets are plotted in Fig. 2, $d\sigma/d\Omega$ in Figs. 3–6, and A_y in Fig. 7.

Obviously, for these light nuclides the most problematic issue is the description of σ_T at low energies. Narrow and broad resonances with large amplitudes appear in the hundreds of keV to few MeV range and the optical model is only expected to provide smooth average results in this region. This is realized to some extent by our OMPs, although for ^{40}Ca the shape of the predicted σ_T deviates from the experimental data points below 100 keV.

The lightest examples of this set, ^{24}Mg, ^{27}Al, and ^{28}Si are deformed nuclides, which may be the reason for the observed discrepancies in the $d\sigma/d\Omega$ between about 5 and 10 MeV for ^{24}Mg and ^{28}Si. Also, for such light nuclides an effective mean field may no longer provide a totally adequate description of the nucleon–nucleus many body problem. Note however that at higher energies the calculations match the data fairly well. Apparently, as the incident energy crosses the thresholds for inelastic scattering to discrete

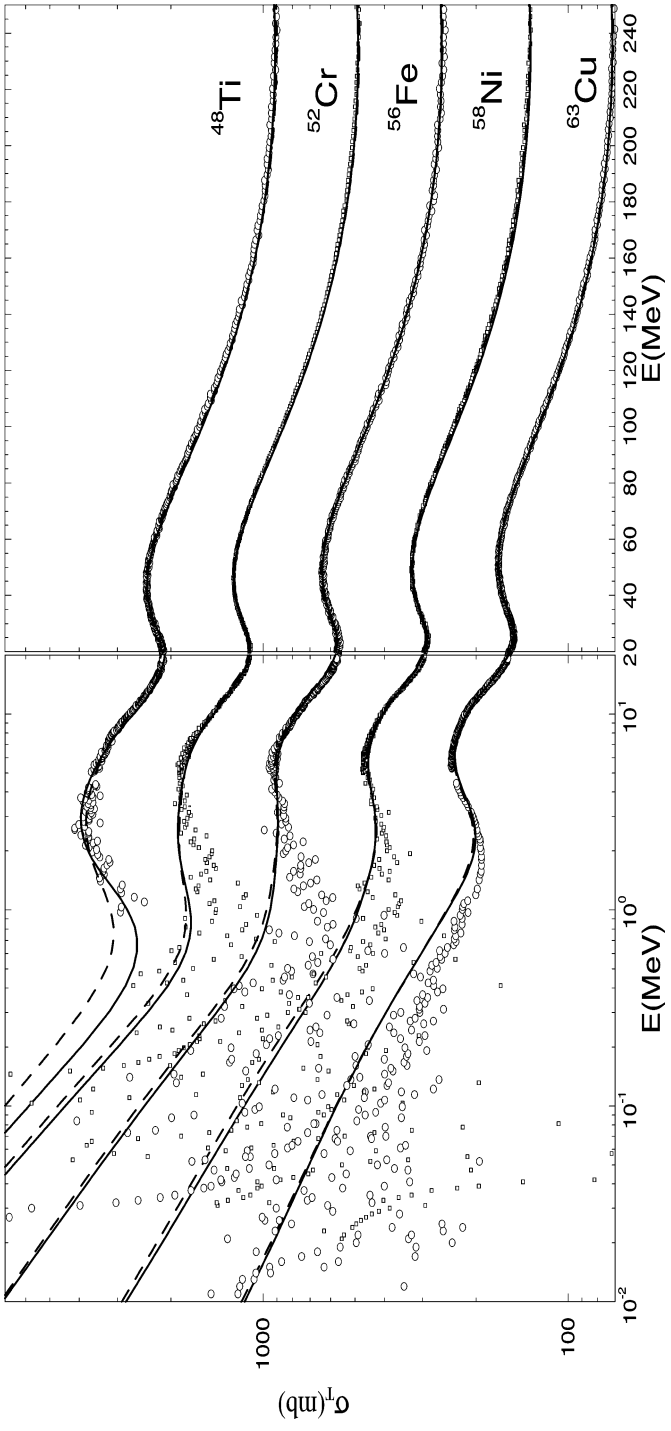

Fig. 8. Comparison of predicted neutron total cross sections and experimental data, for nuclides in the Ti–Cu mass region, for the energy range 10 keV–250 MeV. For more details, see Section 4.1.

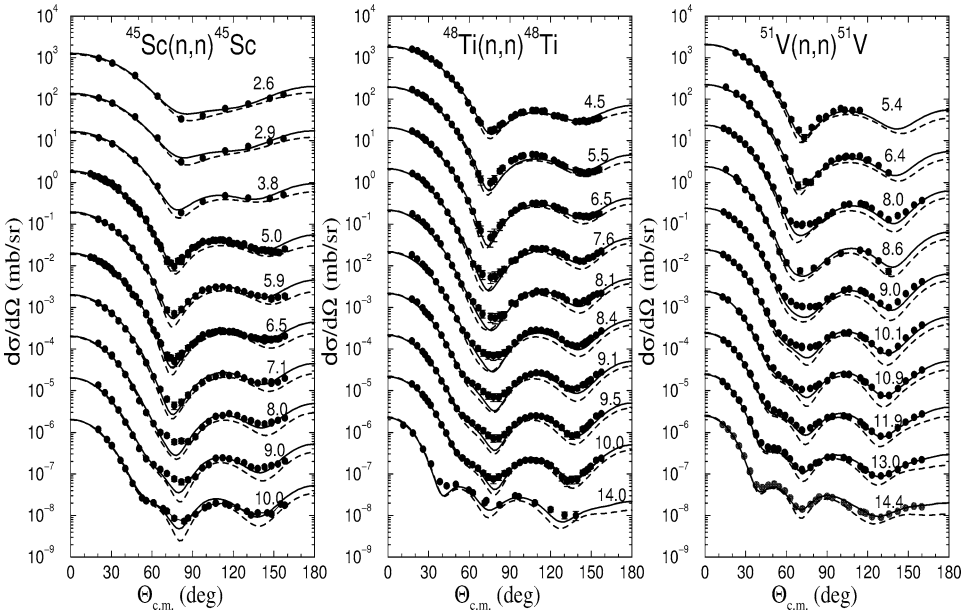

Fig. 9. Comparison of predicted differential cross sections and experimental data, for neutrons scattered from ^{45}Sc, ^{48}Ti, and ^{51}V. For more details, see Section 4.1.

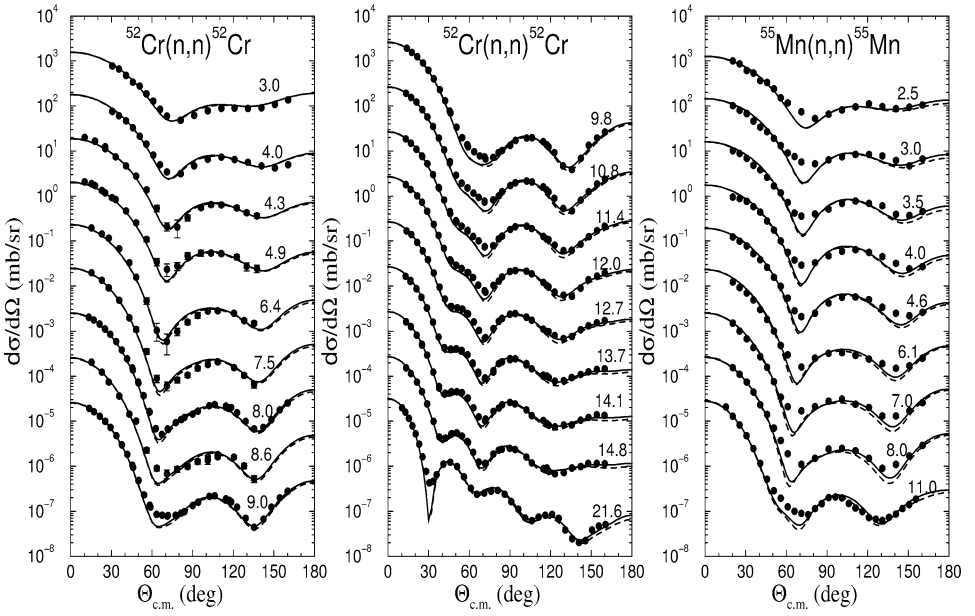

Fig. 10. Comparison of predicted differential cross sections and experimental data, for neutrons scattered from ^{52}Cr and ^{55}Mn. For more details, see Section 4.1.

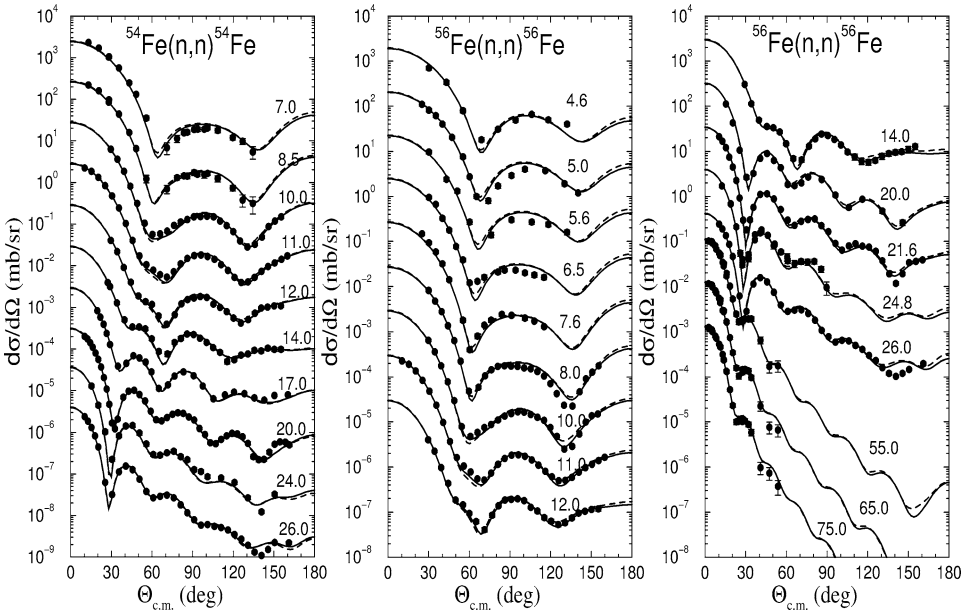

Fig. 11. Comparison of predicted differential cross sections and experimental data, for neutrons scattered from ^{54}Fe and ^{56}Fe. For more details, see Section 4.1.

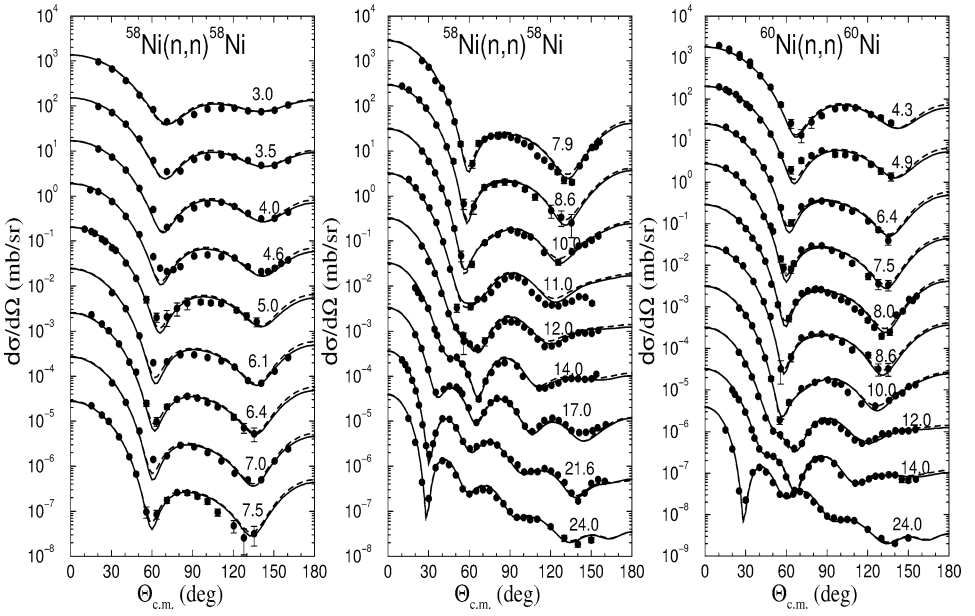

Fig. 12. Comparison of predicted differential cross sections and experimental data, for neutrons scattered from ^{58}Ni and ^{60}Ni. For more details, see Section 4.1.

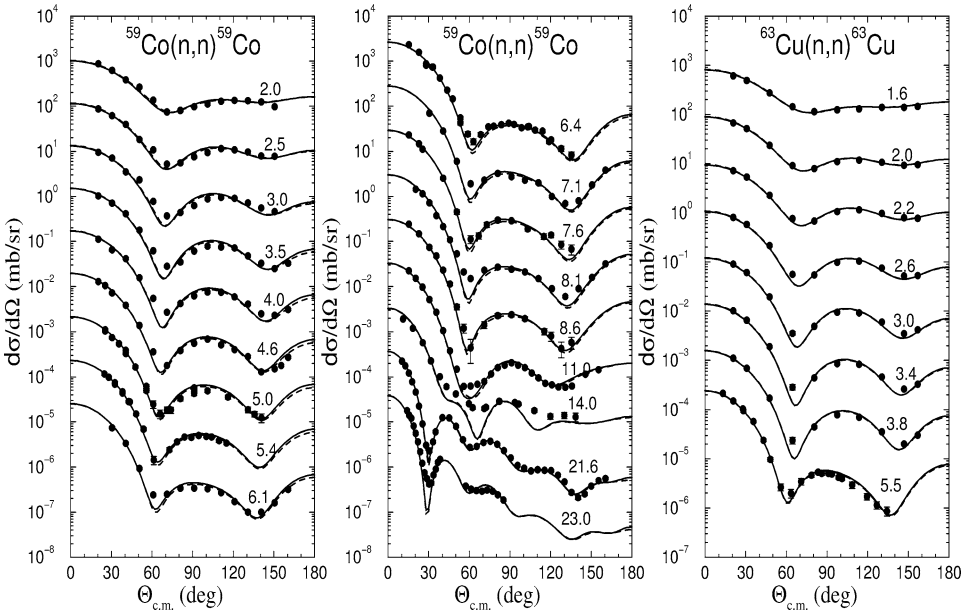

Fig. 13. Comparison of predicted differential cross sections and experimental data, for neutrons scattered from ^{59}Co and ^{63}Cu. For more details, see Section 4.1.

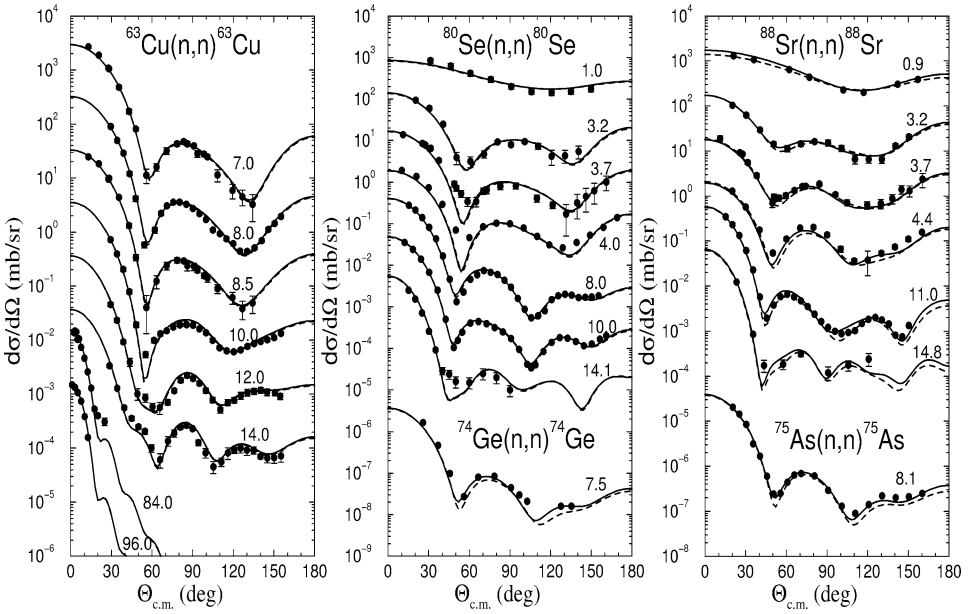

Fig. 14. Comparison of predicted differential cross sections and experimental data, for neutrons scattered from ^{63}Cu, ^{74}Ge, ^{75}As, ^{80}Se, and ^{88}Sr. For more details, see Section 4.1.

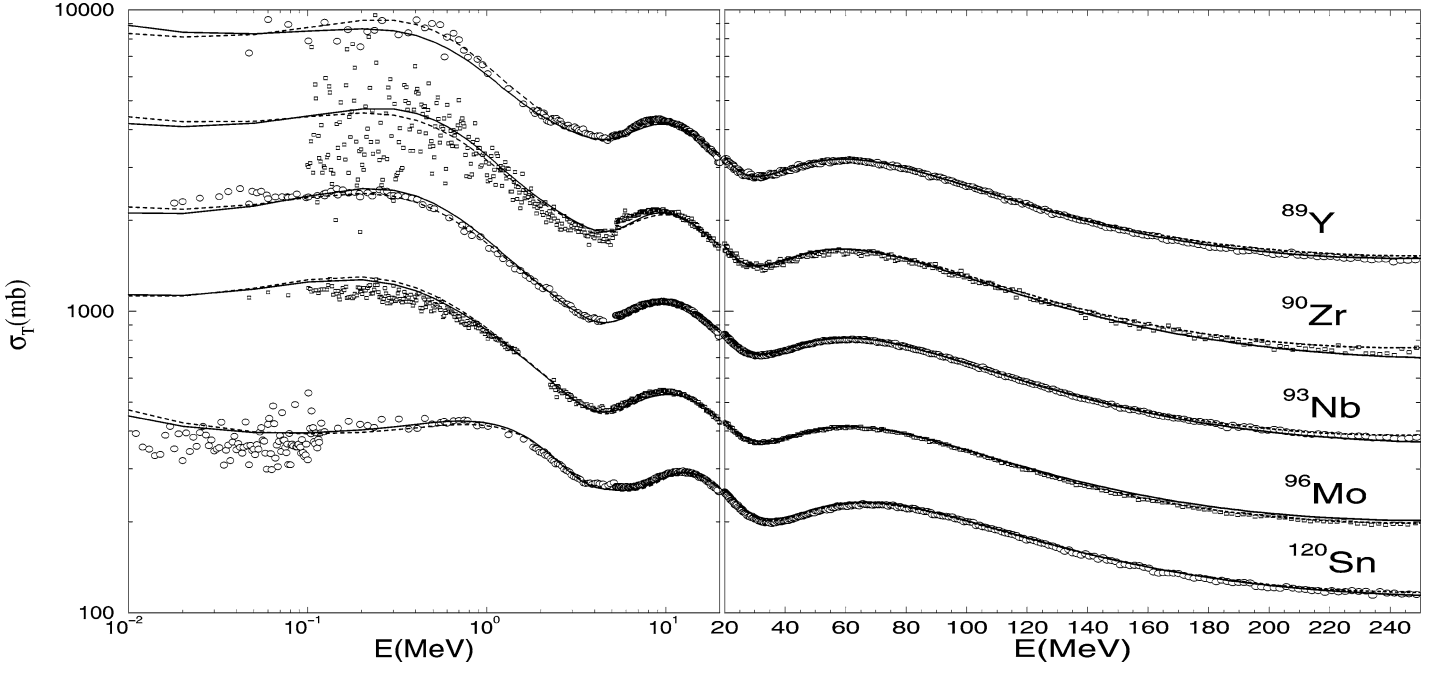

Fig. 15. Comparison of predicted neutron total cross sections and experimental data, for nuclides in the Y–Sn mass region, for the energy range 10 keV–250 MeV. For more details, see Section 4.1.

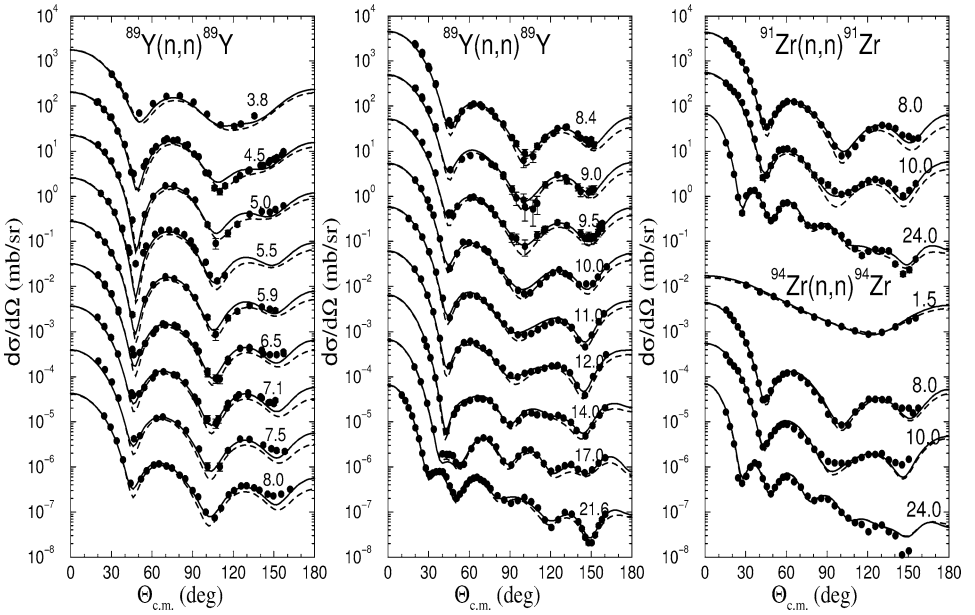

Fig. 16. Comparison of predicted differential cross sections and experimental data, for neutrons scattered from ^{89}Y, ^{91}Zr, and ^{94}Zr. For more details, see Section 4.1.

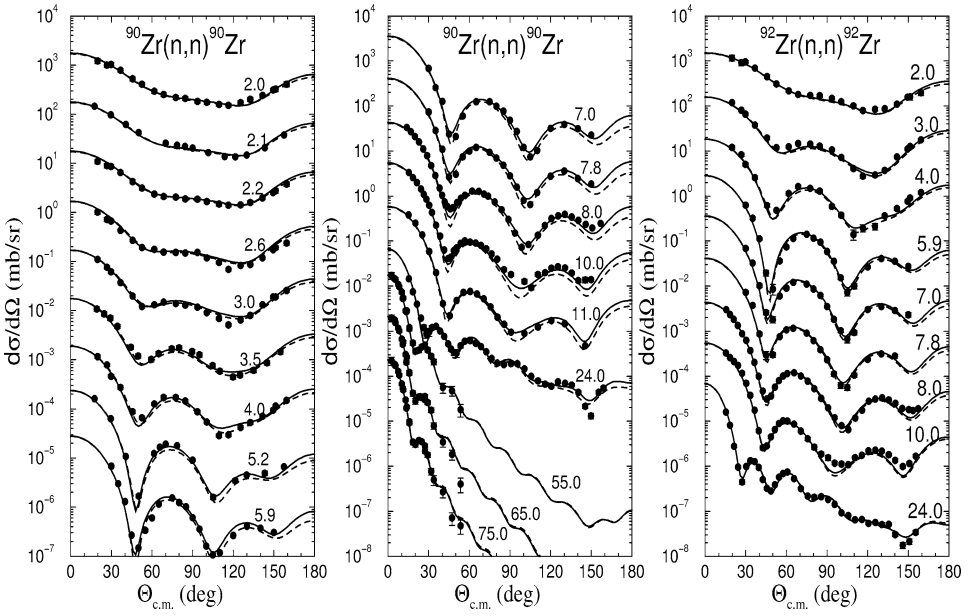

Fig. 17. Comparison of predicted differential cross sections and experimental data, for neutrons scattered from ^{90}Zr and ^{92}Zr. For more details, see Section 4.1.

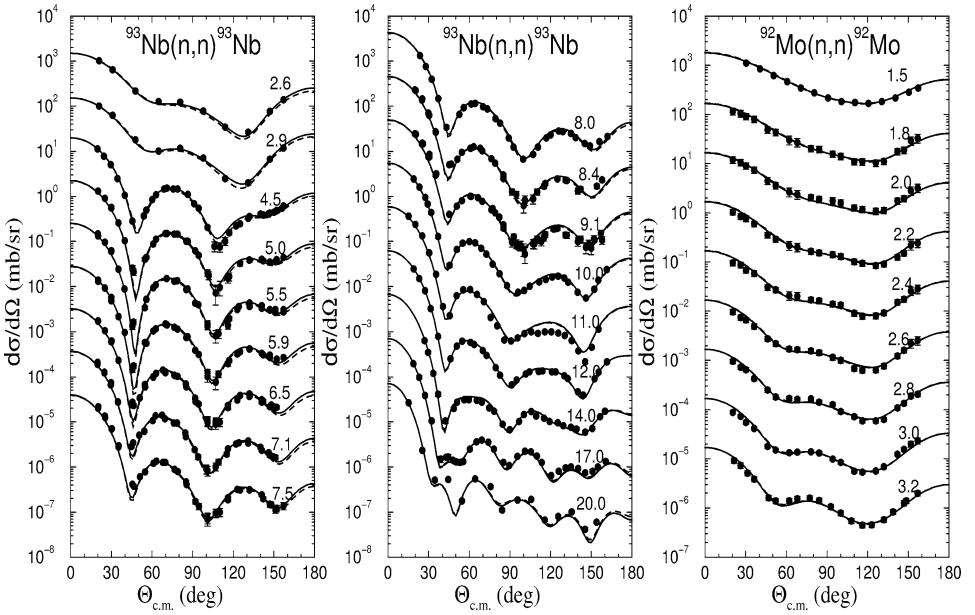

Fig. 18. Comparison of predicted differential cross sections and experimental data, for neutrons scattered from ^{93}Nb and ^{92}Mo. For more details, see Section 4.1.

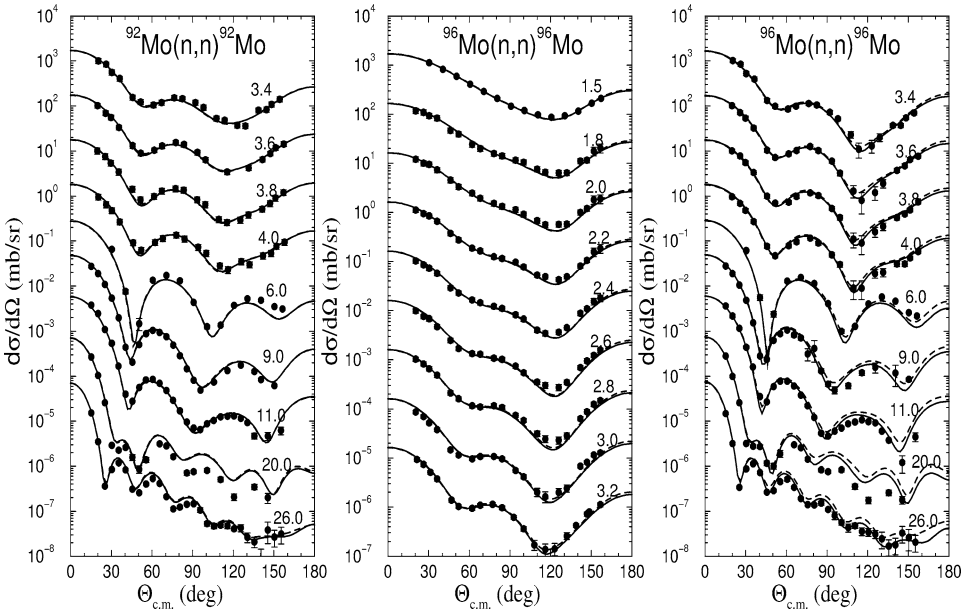

Fig. 19. Comparison of predicted differential cross sections and experimental data, for neutrons scattered from ^{92}Mo and ^{96}Mo. For more details, see Section 4.1.

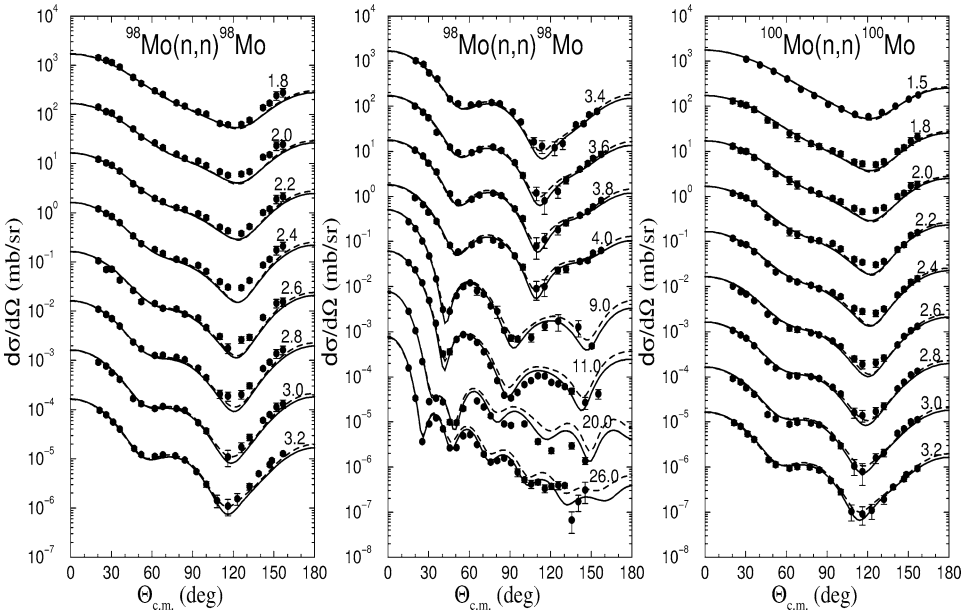

Fig. 20. Comparison of predicted differential cross sections and experimental data, for neutrons scattered from ^{98}Mo and ^{100}Mo. For more details, see Section 4.1.

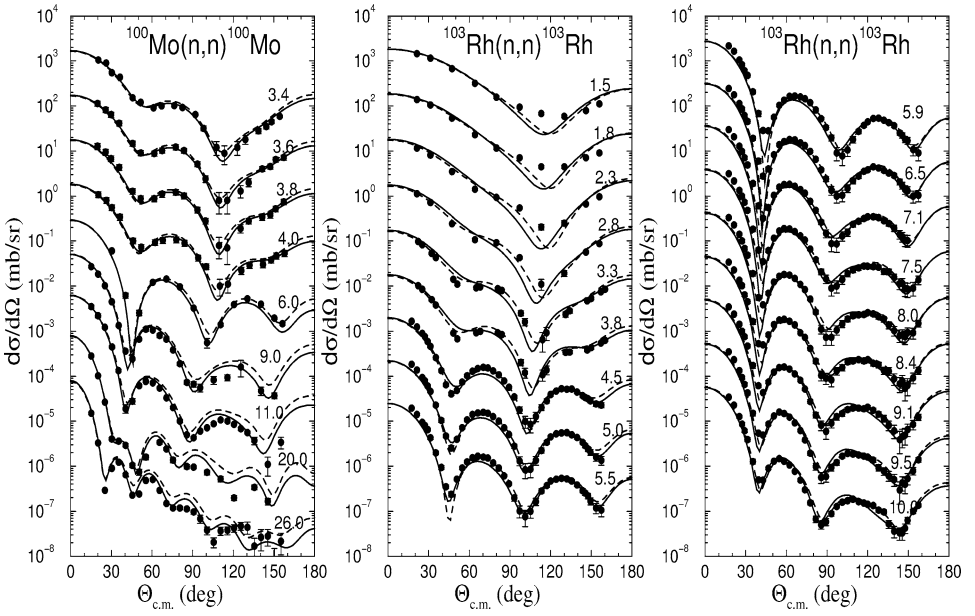

Fig. 21. Comparison of predicted differential cross sections and experimental data, for neutrons scattered from ^{100}Mo and ^{103}Rh. For more details, see Section 4.1.

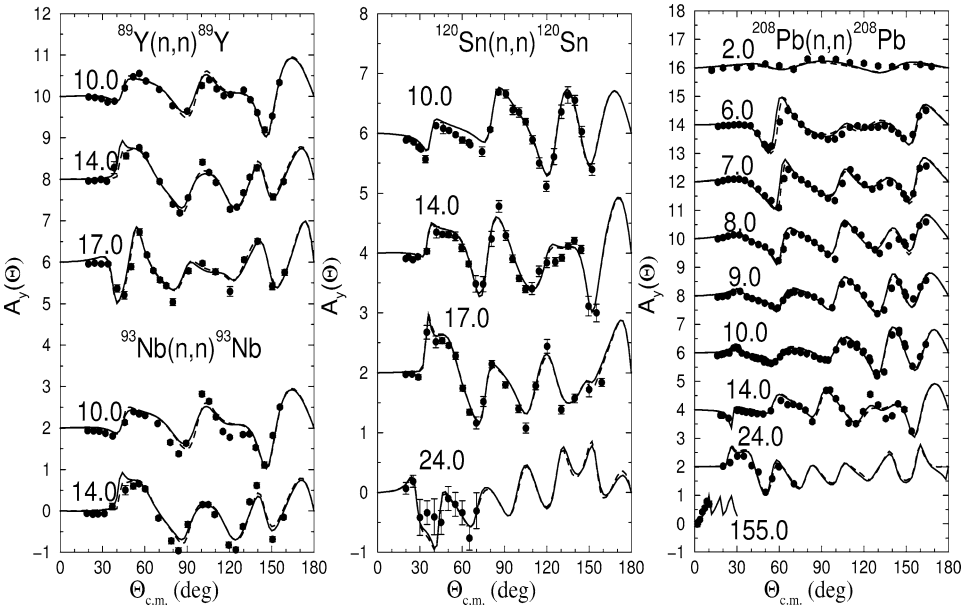

Fig. 22. Comparison of analyzing powers and experimental data, for neutrons scattered from ^{89}Y, ^{93}Nb, ^{120}Sn, and ^{208}Pb. For more details, see Section 4.1.

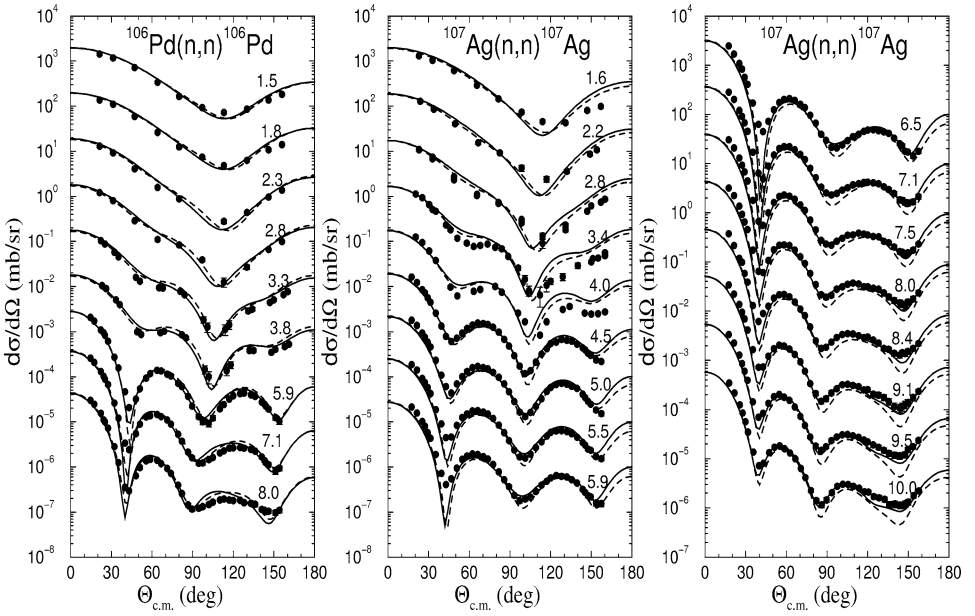

Fig. 23. Comparison of predicted differential cross sections and experimental data, for neutrons scattered from ^{106}Pd and ^{107}Ag. For more details, see Section 4.1.

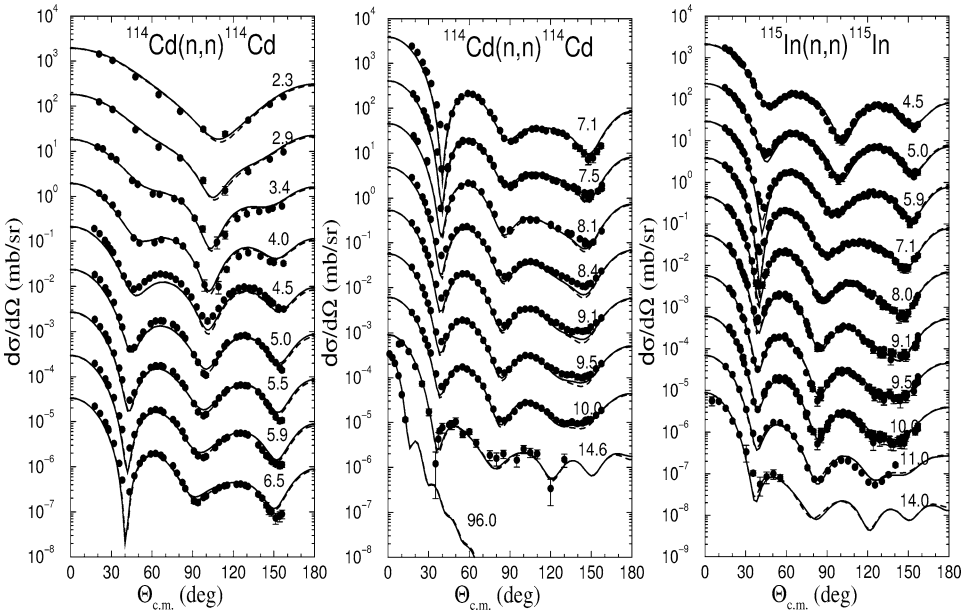

Fig. 24. Comparison of predicted differential cross sections and experimental data, for neutrons scattered from ^{114}Cd and ^{115}In. For more details, see Section 4.1.

states, coupled-channels effects appear to be maximal, whereas they tend to disappear at increasing energies. Difficulties at low energies with using the spherical optical model is a well-known issue that was addressed in the past for proton elastic scattering from light and medium mass nuclei in the 25–50 MeV energy range [26,27]. This problem was also discussed at length in Ref. [28], where coupling to giant resonances was shown to be a clue for solving most existing discrepancies between OMP predictions and scattering data at backward angles. This specific nuclear structure effect identified in the reaction mechanism of incident protons is indeed relevant to the OMP description of neutron scattering from light and medium mass nuclides of present interest. It deserves consideration in a separate study. We intend to repeat our work with full coupled-channels calculations for deformed nuclides, which will hopefully further elucidate such dependencies. The recent $d\sigma/d\Omega$ measurements for Si at 55, 65, and 75 MeV by Baba et al. [29] were included *after* the construction of the local (and global) OMP.

A recurring, and well-known problem [1,30,31] is formed by the $d\sigma/d\Omega$ for ^{40}Ca in the energy range 6–12 MeV. The data is not as sharply structured as the OMP result, and it is not yet known why this happens for this spherical nucleus. Again, coupling to giant resonances [28] might alleviate this burden. The predicted A_y at 10 MeV suffers from a similar deviation from the data.

4.2.2. Sc, Ti, V, Cr, Mn, Fe, Ni, Co *and* Cu *targets*

The results for σ_T for some of these targets are plotted in Fig. 8, $d\sigma/d\Omega$ in Figs. 9–14, and A_y in Fig. 7.

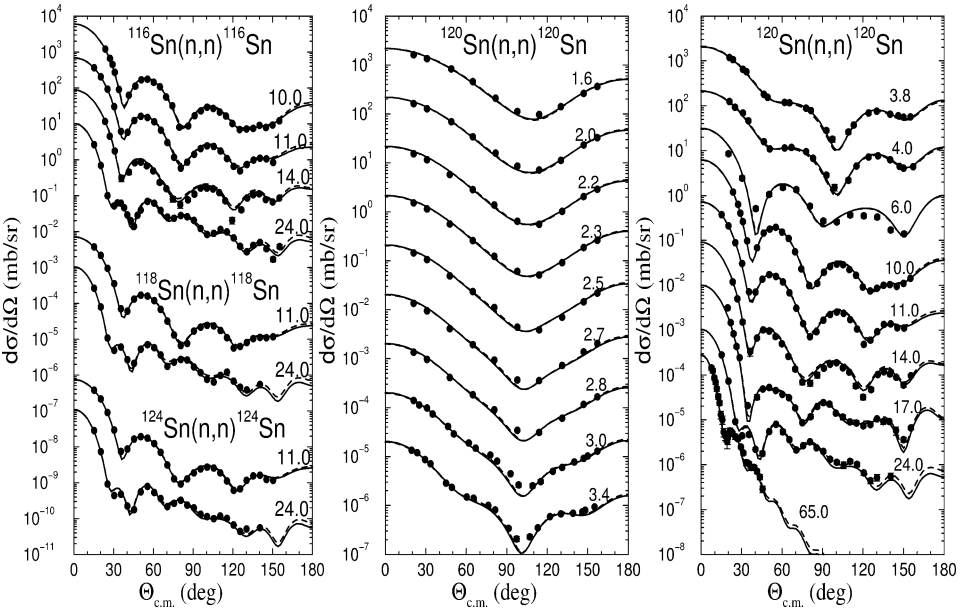

Fig. 25. Comparison of predicted differential cross sections and experimental data, for neutrons scattered from ^{116,118,120,124}Sn. For more details, see Section 4.1.

A well known problem, and one that is not solved in this paper, is the poor description of σ_T below 3 MeV in the Cr–Ni region. The measurements suggest a broad low-energy structure which is not predicted by our OMP. Dispersion relations [32] and a coupled-channels approach [33] only partially solve this problem and so far only an optical model with a contribution from selected partial waves has been able to reproduce the data [34]. With ECISVIEW we have found that only a local E-dependence of the volume and surface geometry parameters at low energies can account for the required extra minimum around 1–2 MeV. Since there does not seem to be a physical ground for this, and we only use this approach for purely applied purposes, we will not discuss it in the present paper. For targets around copper, our low-energy model results are again in phase with the experimental data. At energies above 3 MeV, we get the usual agreement with data, to within 1–2% for each nuclide.

The predicted $d\sigma/d\Omega$ are in good agreement with experiment for all target nuclides in this mass range. The largest deviations seem to occur for the first minimum in angular distributions of ^{55}Mn and to a lesser extent for the data from the other odd nuclide ^{59}Co. In the case of ^{55}Mn, we suspect that it was experimentally impossible to resolve the first low-lying inelastic level from the elastic channel. The only other problem we have in this mass region concerns the shoulder before the first minimum in ^{52}Cr elastic scattering between 8 and 12 MeV. This nucleus is deformed which again may be the cause of our underprediction of the experimental data [35].

The $d\sigma/d\Omega$ results at 21.6 and 23 MeV for ^{59}Co illustrate another advantage of our global OMP approach, namely that it brings to surface inconsistencies between several

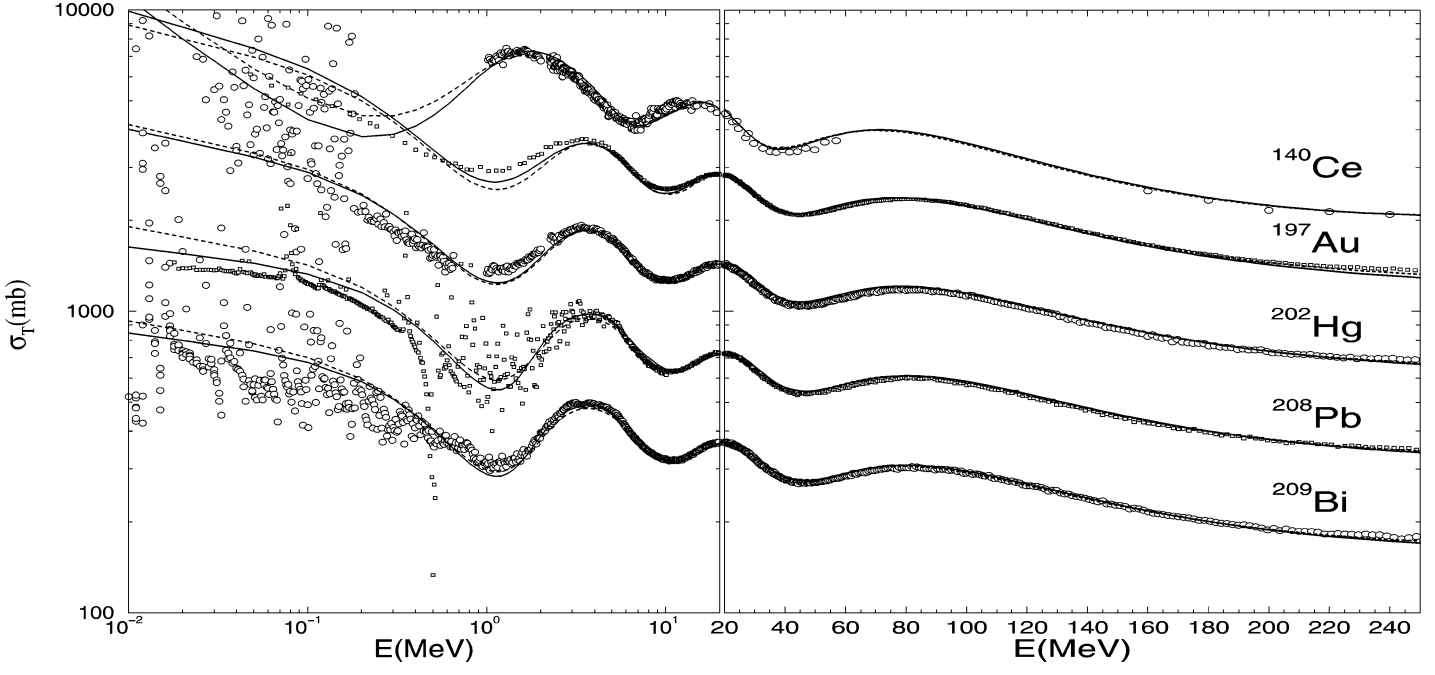

Fig. 26. Comparison of predicted neutron total cross sections and experimental data, for nuclides in the Ce–Bi mass region, for the energy range 10 keV–250 MeV. For more details, see Section 4.1.

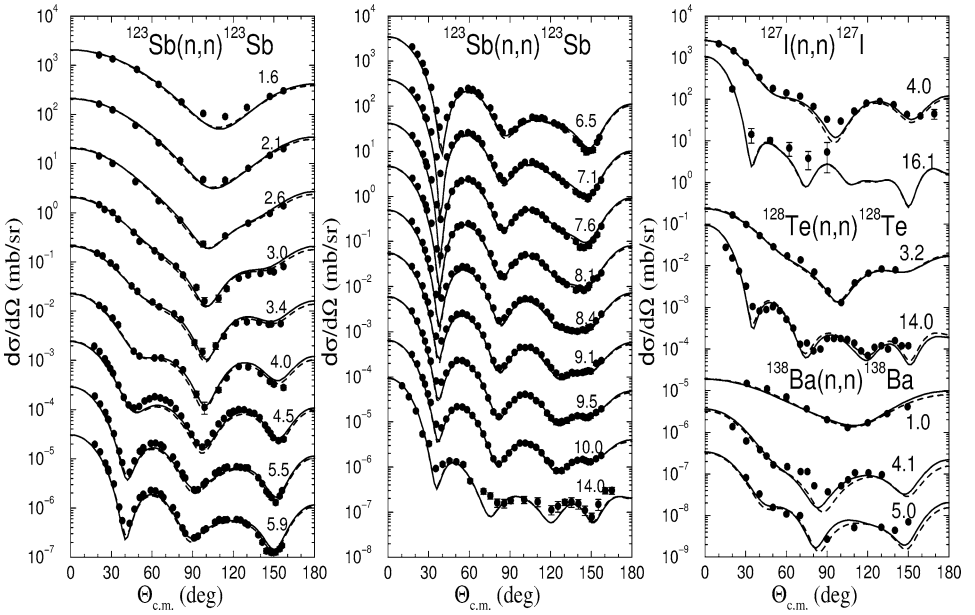

Fig. 27. Comparison of predicted differential cross sections and experimental data, for neutrons scattered from ^{123}Sb, ^{127}I, ^{128}Te, and ^{138}Ba. For more details, see the caption of Fig. 3.

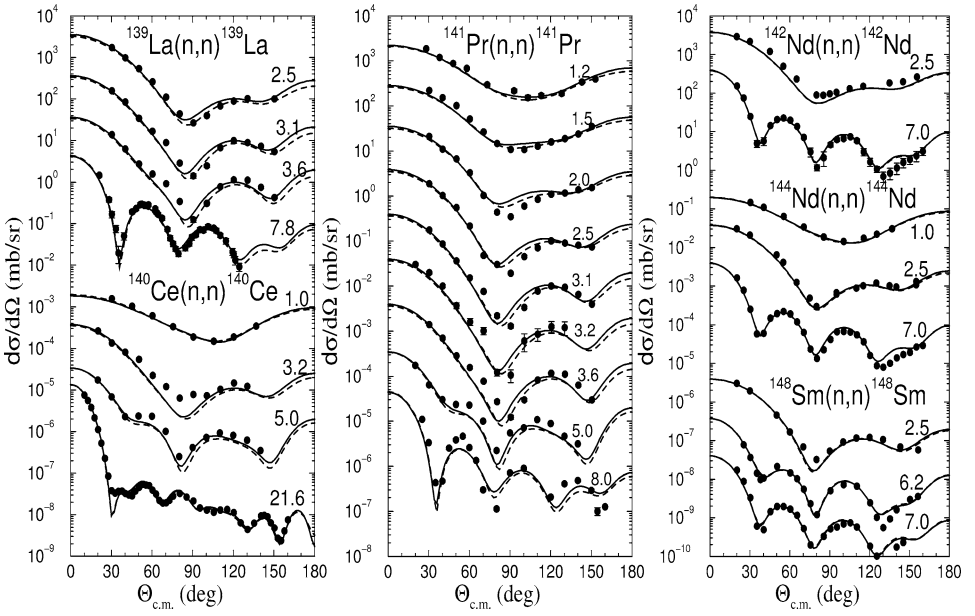

Fig. 28. Comparison of predicted differential cross sections and experimental data, for neutrons scattered from ^{139}La, ^{140}Ce, ^{141}Pr, ^{142}Nd, ^{144}Nd, and ^{148}Sm. For more details, see Section 4.1.

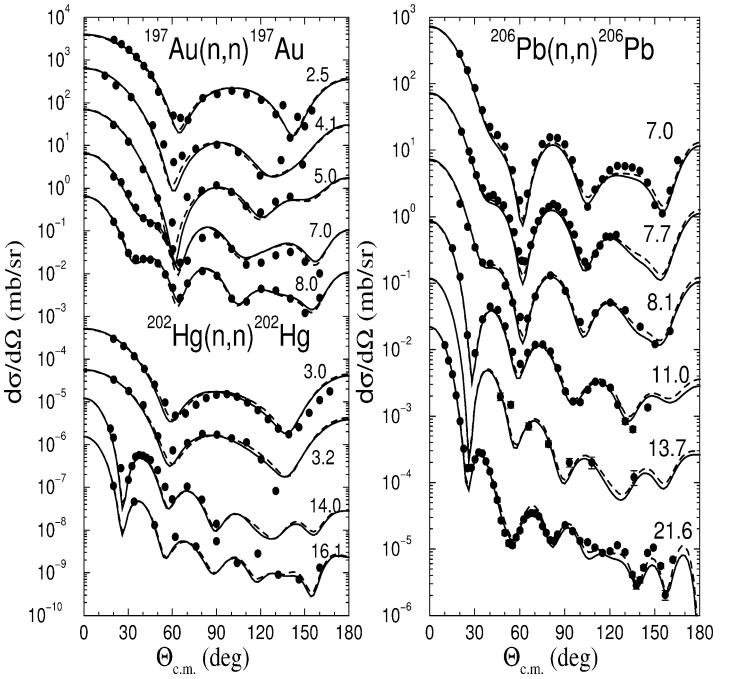

Fig. 29. Comparison of predicted differential cross sections and experimental data, for neutrons scattered from ^{197}Au, ^{202}Hg and ^{206}Pb. For more details, see Section 4.1.

data sets. The effective mean field is not expected to change as much as is suggested by these two angular distributions. A comparison of the results for 21.6 and 24 MeV angular distributions for ^{58}Ni support this statement. Again, we assume that the difference can be attributed to the contamination of the experimental scattering cross sections by inelastic processes that have not been resolved in the measurement at 23 MeV for ^{59}Co. The recent $d\sigma/d\Omega$ measurements for Fe at 55, 65, and 75 MeV by Baba et al. [29] were included *after* the construction of the local (and global) OMP. Finally, the A_y data are well described for all nuclides in this mass range.

4.2.3. Se, Ge, As, Sr, Y, Zr, Nb *and* Mo *targets*

The results for σ_T for some of these targets are plotted in Fig. 15, $d\sigma/d\Omega$ in Figs. 14 and 16–21, and A_y in Fig. 22.

In this mass range, the calculated and measured σ_T values are in excellent agreement over the whole energy range. Only for ^{89}Y and ^{90}Zr at energies between 3 and 7 MeV, is the deviation between our OMP and the data large (about 4%). For all other targets and energies above 1 MeV, the usual 1% precision is found.

Concerning angular distributions, we first note that for ^{80}Se at several incident energies the experimental data sets are in disagreement with our results at the first minimum. This may stem from mishandling of sample size effects (i.e., attenuation of the neutron flux, and multiple scattering in the sample) while extracting the actual data value at each angle from

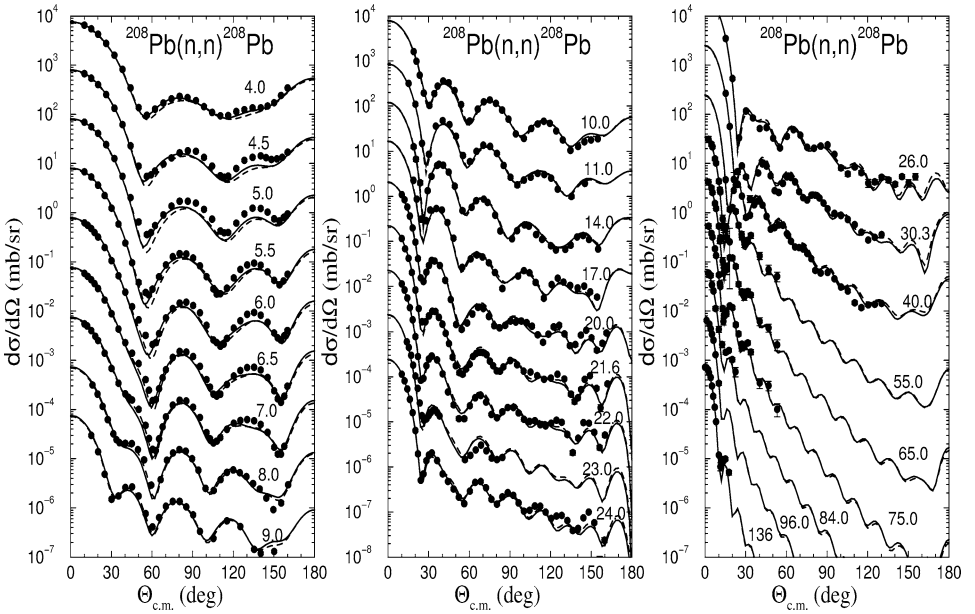

Fig. 30. Comparison of predicted differential cross sections and experimental data, for neutrons scattered from ^{208}Pb. For more details, see Section 4.1.

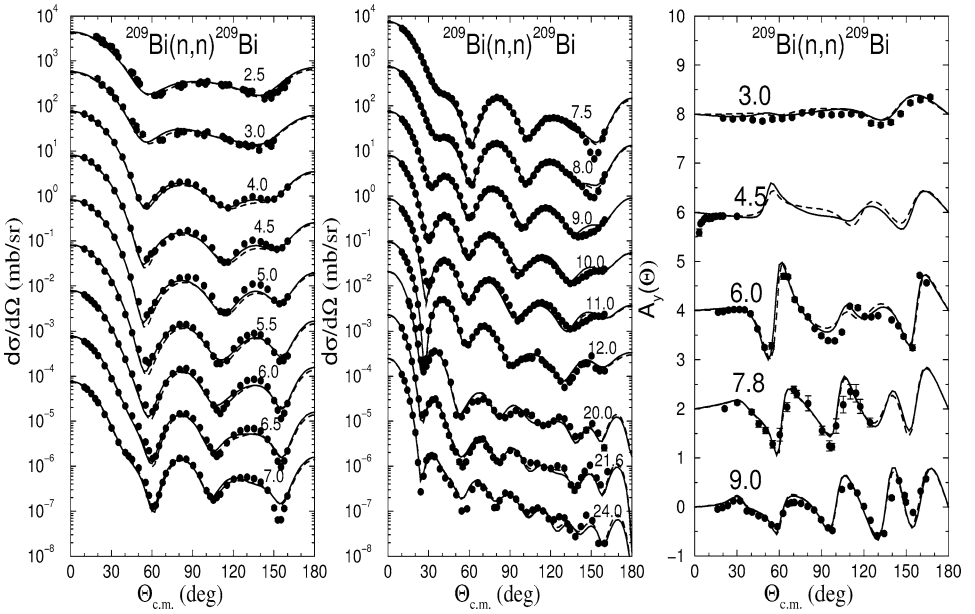

Fig. 31. Comparison of predicted differential cross sections, analyzing powers and experimental data, for neutrons scattered from ^{209}Bi. For more details, see Section 4.1.

raw data. The description of the $d\sigma/d\Omega$ for ^{89}Y, ^{90}Zr, and ^{93}Nb is almost perfect. For the heaviest Mo-isotopes, which are of a deformed nature, there is some overestimation at backward angles for incident energies above 6 MeV (see, e.g., incident energies of 9, 11, and 26 MeV for ^{100}Mo). However, there could be some conflicting measurements in this energy region. The experimental data at 20 MeV seem to strongly contradict our predictions for all Mo-isotopes, including the near-spherical ^{92}Mo, where our description at the other energies is very good.

The recent $d\sigma/d\Omega$ measurements for Zr at 55, 65, and 75 MeV by Baba et al. [29] were included *after* the construction of the local (and global) OMP. The A_y data are well described for all nuclides in this mass range.

4.2.4. Rh, Pd, Ag, Cd, In *and* Sn *targets*

The results for σ_T (i.e., for ^{120}Sn) are plotted in Fig. 15, $d\sigma/d\Omega$ in Figs. 21 and 23–25, and A_y (i.e., for ^{120}Sn) in Fig. 22.

The transition region around $A = 100$–114 should strictly be described by the coupled-channels formalism. Nevertheless, a spherical approach for these nuclides gives surprisingly good results, especially for energies above a few MeV. A small price is to be paid for this however. We note that the value (10) for the optical model parameter d_3 (see Table 6), which drives the low-energy behaviour of the surface absorption, lies somewhat outside the global average for the nuclides ^{100}Mo, ^{103}Rh, and ^{106}Pd. Apparently, this is needed to mask some low-energy collective effects for these nuclides. Not shown here are the σ_T for deformed nuclides like Rh, Pd, and Ag. Our OMPs overpredict the data for these nuclides below 5 MeV by about 5–10%. The total cross section for Sn is again very well described.

The $d\sigma/d\Omega$ data for the deformed nucleus ^{103}Rh seem to suffer somewhat from our spherical model approach. Although the phasing of the angular distributions is satisfactory, the extrema are not completely reached. This also is the case to some extent for ^{106}Pd and ^{114}Cd in the region between 4 and 6 MeV. When we reach the next region of (near-) spherical nuclides, the In and Sn isotopes, we again obtain very good agreement for all energies. The A_y measurements for ^{120}Sn are well described.

4.2.5. Sb, I, Te, Ba, La, Ce, Pr, Nd *and* Sm *targets*

The results for σ_T (i.e., for ^{140}Ce) are plotted in Fig. 26, and $d\sigma/d\Omega$ in Figs. 27–28.

^{140}Ce is one of the few isotopes for which high-energy neutron total cross section measurements were performed prior to the large measurement program of Refs. [24,25]. The high-energy σ_T values are well described by our OMP results. However, a conspicuous issue is the relatively large difference between the local and the global OMP prediction for σ_T of ^{140}Ce below a few MeV.

For nuclei other than ^{123}Sb, there are only a few measurements per isotope in this mass region. Hence, the OMPs had to be carefully designed by combining different adjacent nuclides simultaneously in the optimization process. The results are not satisfactory for 14 MeV on ^{123}Sb and for ^{141}Pr at several incident energies. However, the good performance for neighboring nuclides again reveals the issue of the quality of the measurements. It is often difficult to discern whether the limitations are due to the optical model or due to the experiment. An extraordinary case is the 21.6 MeV $d\sigma/d\Omega$ for ^{140}Ce,

where we get perfect agreement from 40 degrees to the very backward angles, but where our OMP, in contrast with the data, predicts a sharp minimum at 30 degrees.

4.2.6. Au, Hg, Pb *and* Bi *targets*

The results for σ_T for some of these targets are plotted in Fig. 26, $d\sigma/d\Omega$ in Figs. 29–31, and A_y in Figs. 22 (for ^{208}Pb) and 31 (for ^{209}Bi).

^{197}Au and several of the isotopes of Hg are slightly deformed. The failure of a spherical optical model to describe deformed nuclides is often indicated by an inadequate prediction of the extrema in the total cross section. This occurs to some extent for Au (below 10 MeV) and Hg (below 3 MeV). For the spherical nuclides ^{208}Pb and ^{209}Bi the situation is again under control, although there is a slight overestimation (5–10%) of the σ_T measurements for energies below 500 keV. For these heavy nuclides, more Ramsauer resonances appear than for the light nuclides of, e.g., Fig. 2. We mention here that the proper description of the last minimum in σ_T around about 50 MeV is very sensitive to the choice of OMP parameters. Only a very constrained combination of V_V, W_V, r_V, a_V, and W_D is able to describe σ_T in this region. A precise description of σ_T for heavy nuclides can *only* be obtained by means of the power 2 in the Brown–Rho functions of W_V, see Eq. (7), whereas for lighter nuclides a power of 4, with different choices for w_1 and w_2, leads to a solution of equivalent quality. Indeed, the σ_T measurements for Pb and Bi directed us to a global choice of the power of 2.

Only a few $d\sigma/d\Omega$ measurements have been performed for Au and Hg. Our OMPs give a reasonable description of the data, although we anticipate that the coupling to the low-lying collective levels of the deformed Au-nucleus will have a significant effect on the prediction of σ_T and the first angular minimum at low incident energies [36]. For Pb and Bi, this phenomenon is no longer present although our results for these nuclides underestimate the last oscillation in angular distributions between 4 and 8 MeV. This has been observed before [37,38]. At the other energies, close agreement is obtained over the entire angular range. In general, the A_y data are well described.

4.3. Proton-induced data

For incident protons, our analysis is based on about 250 elastic scattering angular distributions $\sigma(\theta)/\sigma_{\text{Ruth}}$, 90 analyzing power angular distributions $A_y(\theta)$, and the large compilation of reaction cross sections σ_R of Ref. [39], augmented with the recent data of Ref. [40]. A significant part of these data are compared with the theoretical results in Figs. 32–44. The references for the experimental differential data are listed in Table 7.

In general, the proton fits are of somewhat lower quality than those we have obtained for neutron scattering. A particular problem arises at the highest energies, above about 150 MeV, where the phasing of forward angle $\sigma(\theta)/\sigma_{\text{Ruth}}$ is often not satisfactory. At these energies, the validity of the Woods–Saxon form factors begins to break down and E-dependent geometry parameters would be required to mimic a different shape of the density distribution of the nucleus. However, we have chosen to retain our unified functional form for the OMP parameters, rather than adopting unphysical E-dependencies of the parameters, at the expense of a somewhat lower quality of fit at the highest energies. The description of proton A_y data is generally quite good, with the exception of the lightest

nuclides and at the highest energies. On average, the difference between calculated and measured reaction cross sections is between 5 and 10%.

4.3.1. Al, Si, *and* Ca *targets*

The results for σ_R for these targets are plotted in Fig. 32, $\sigma(\theta)/\sigma_{\text{Ruth}}$ in Figs. 33–34, and A_y in Fig. 35.

The predicted proton reaction cross sections are in good agreement with the measured data above 20–30 MeV. At lower energies, we overpredict the data by about 10%. Apparently, the problems of our OMPs to fit differential data for light nuclides are larger for protons than for neutrons. Again, there could be two reasons for this: first, our proton OMPs may not be appropriate for nuclides as light as Al and Si, and second, the data may be mutually inconsistent. Note how the $\sigma(\theta)/\sigma_{\text{Ruth}}$ for 28 MeV protons incident on ^{27}Al is underpredicted by our local OMP, while the same reaction on ^{28}Si is overpredicted by roughly the same margin. Such a large difference between two adjacent nuclides is not expected from a theoretical point of view. Notwithstanding possible experimental problems, our predictions for these nuclides tend to produce a too structured angular distribution, which is exemplified by the $\sigma(\theta)/\sigma_{\text{Ruth}}$ at 17 and 61.4 MeV for ^{27}Al, and 17.8 and 40 MeV for ^{28}Si. Similar problems were discussed for neutrons in Section 4.2.1. The first minima in the data at the highest energies for ^{27}Al are not reproduced and there are backward angle problems for ^{28}Si. The $\sigma(\theta)/\sigma_{\text{Ruth}}$ fits at high energies are much better for ^{40}Ca, although here the same phasing problem as for neutrons appears for energies below 30 MeV. For the A_y data for light nuclides, the description is reasonable, although at the highest energies the extrema are not completely reached. Also for 14.5 and 16 MeV protons incident on ^{40}Ca, there is a significant overprediction of the A_y data around 90 degrees. These findings are consistent with those of the semi-microscopic optical model of Ref. [1].

4.3.2. Fe, Ni *and* Cu *targets*

The results for σ_R for these targets are plotted in Fig. 32, $\sigma(\theta)/\sigma_{\text{Ruth}}$ in Figs. 34 and 36–38, and A_y in Figs. 39–40.

Not only are the proton reaction cross sections for these nuclides fitted very well, but also the $\sigma(\theta)/\sigma_{\text{Ruth}}$ are described excellently at all energies. The exceptions are some phasing problems in a few angular distributions at angles beyond 130 degrees (e.g., for 40 MeV protons incident on ^{54}Fe) and an inconsistent behaviour of our $\sigma(\theta)/\sigma_{\text{Ruth}}$ versus data at 100 and 160 MeV protons incident on ^{58}Ni. An overall good description of the A_y data is obtained, although at the highest energies, the extrema of the A_y are too pronounced. Again, this is consistent with the behaviour found in a semi-microscopic OMP approach [1].

4.3.3. Zr and Sn targets

The results for σ_R for these targets are plotted in Fig. 32, $\sigma(\theta)/\sigma_{\text{Ruth}}$ in Figs. 38 and 41, and A_y in Fig. 42.

The predicted proton reaction cross sections are slightly higher than most of the data points for ^{90}Zr, while the description for ^{120}Sn is good. In terms of experimental differential data, ^{90}Zr is a well-covered nucleus and thus particularly suitable to assess the

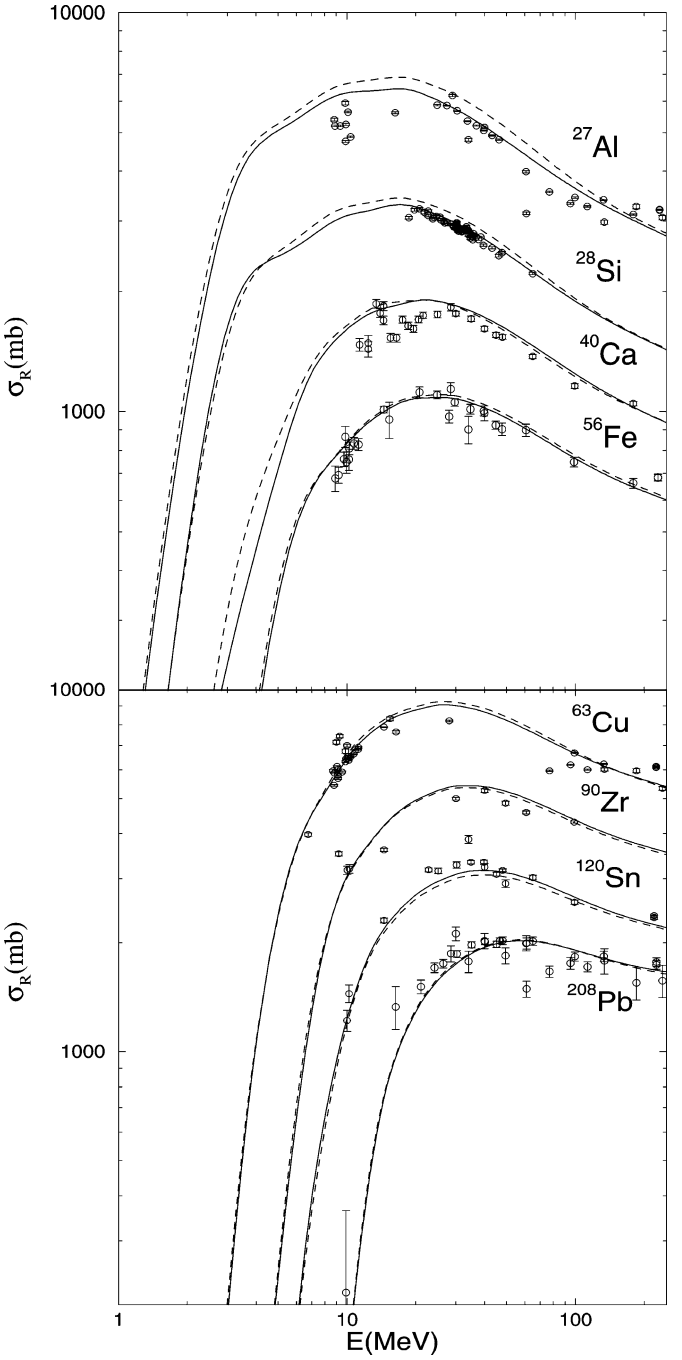

Fig. 32. Comparison of predicted proton reaction cross sections and experimental data, for nuclides in the Al–Pb mass region, for energies up to 250 MeV. For more details, see Section 4.1.

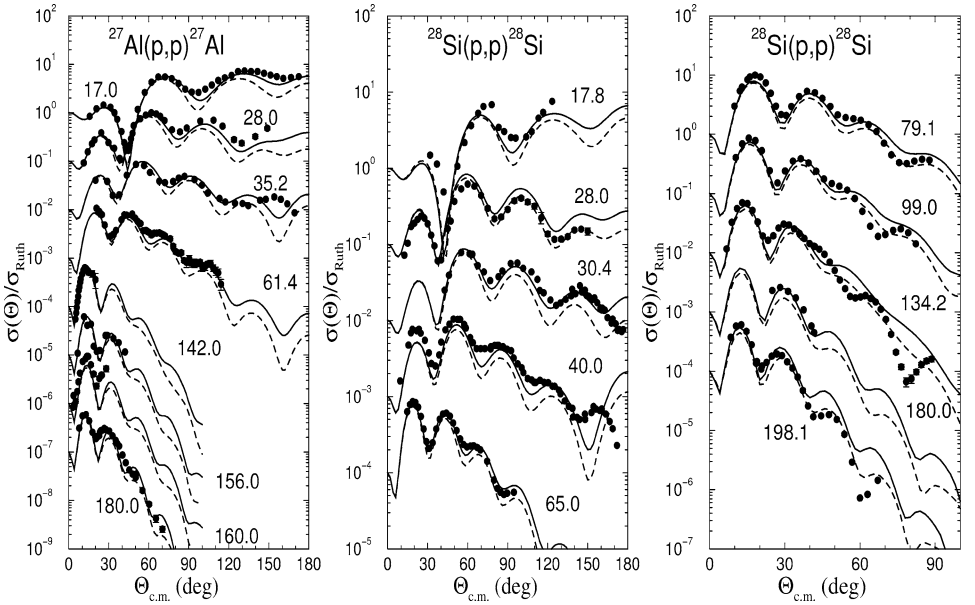

Fig. 33. Comparison of predicted differential cross sections and experimental data, for protons scattered from ^{27}Al and ^{28}Si. For more details, see Section 4.1.

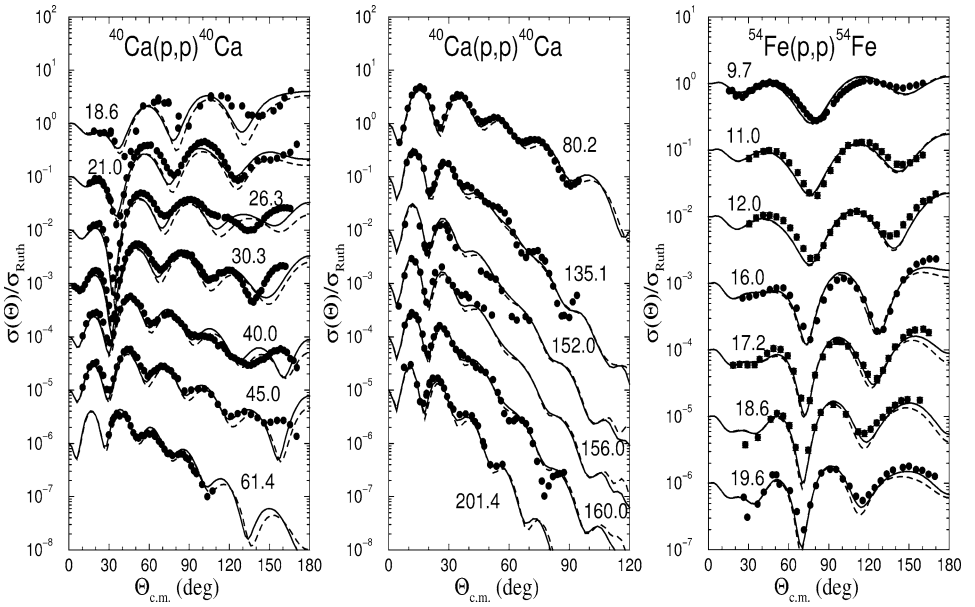

Fig. 34. Comparison of predicted differential cross sections and experimental data, for protons scattered from ^{40}Ca and ^{54}Fe. For more details, see Section 4.1.

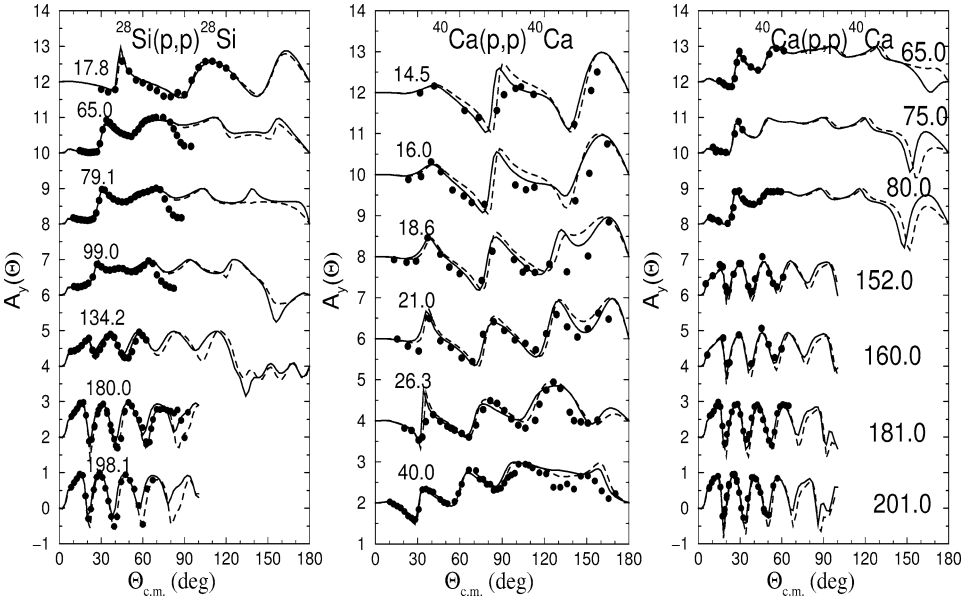

Fig. 35. Comparison of analyzing powers and experimental data, for protons scattered from ^{28}Si and ^{40}Ca. For more details, see Section 4.1.

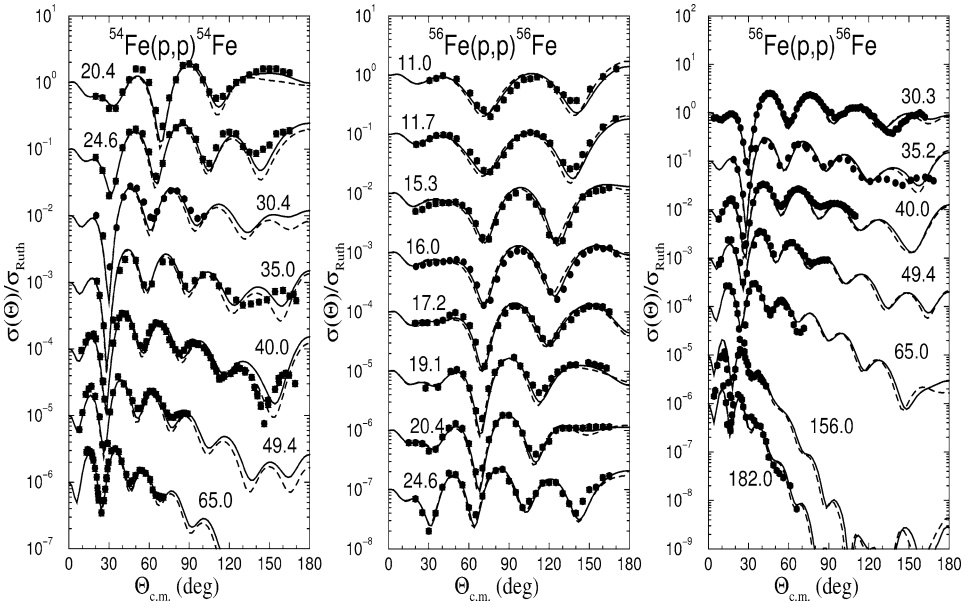

Fig. 36. Comparison of predicted differential cross sections and experimental data, for protons scattered from ^{54,56}Fe. For more details, see Section 4.1.

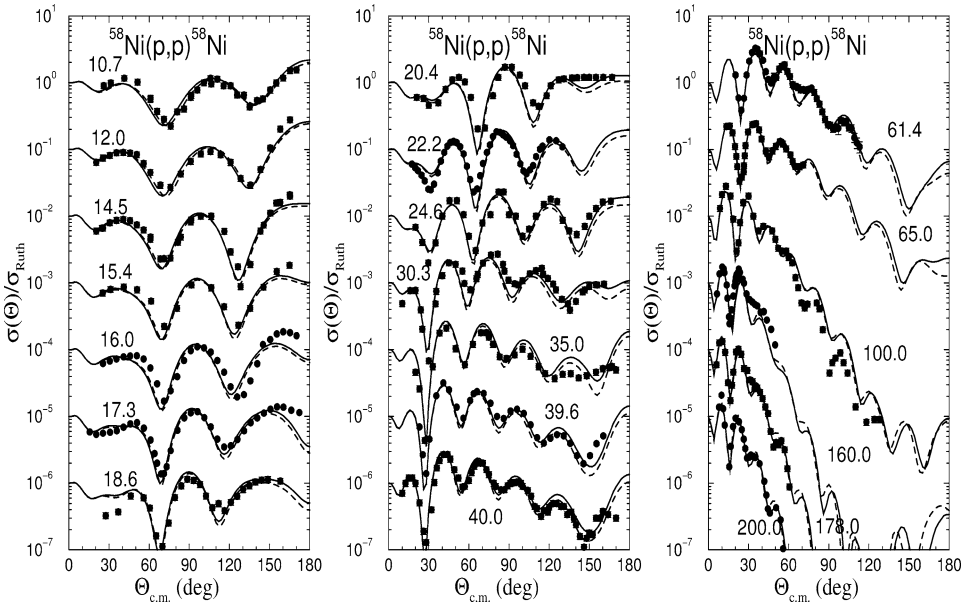

Fig. 37. Comparison of predicted differential cross sections and experimental data, for protons scattered from ^{58}Ni. For more details, see Section 4.1.

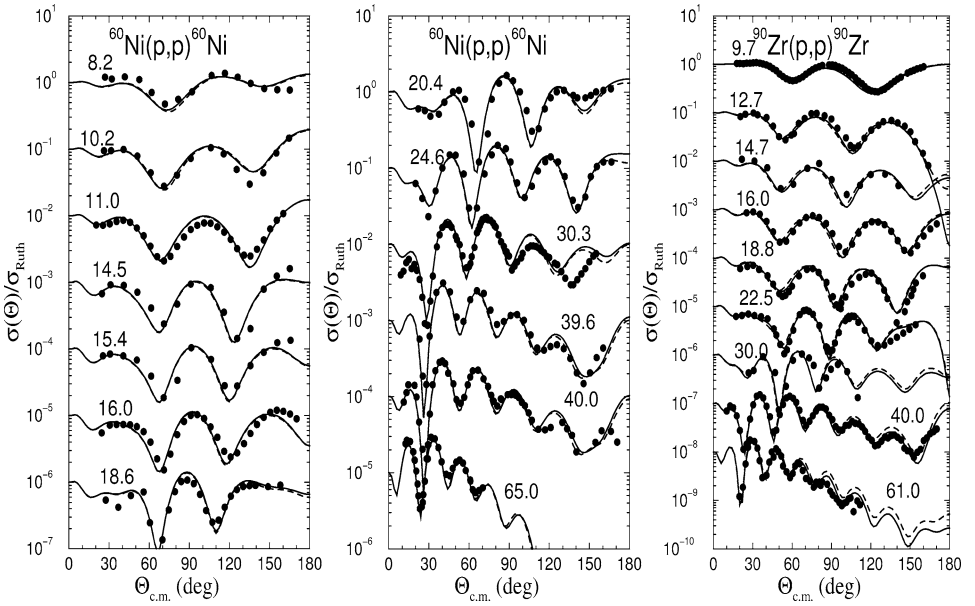

Fig. 38. Comparison of predicted differential cross sections and experimental data, for protons scattered from ^{60}Ni and ^{90}Zr. For more details, see Section 4.1.

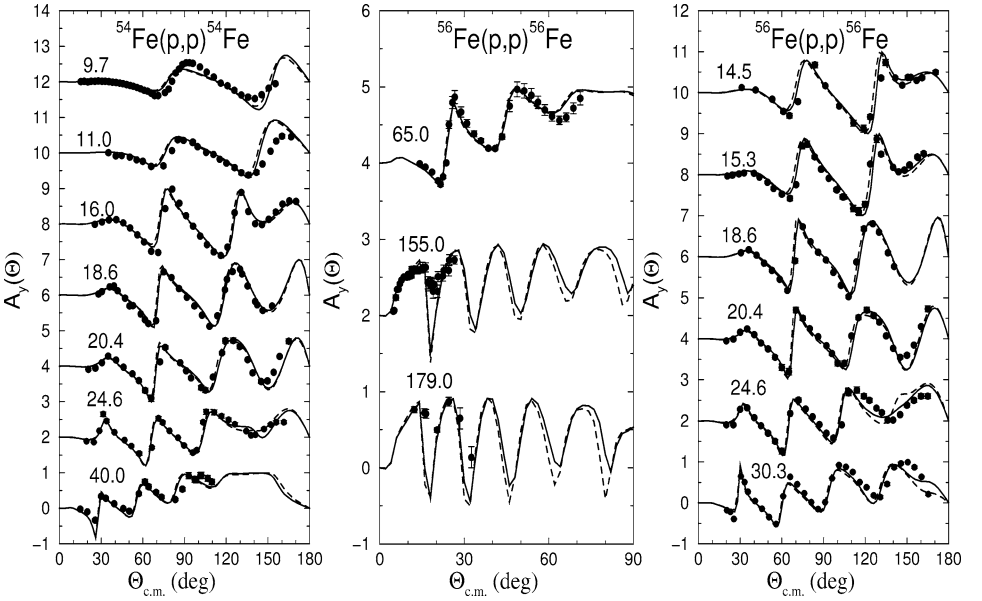

Fig. 39. Comparison of analyzing powers and experimental data, for protons scattered from ^{54,56}Fe. For more details, see Section 4.1.

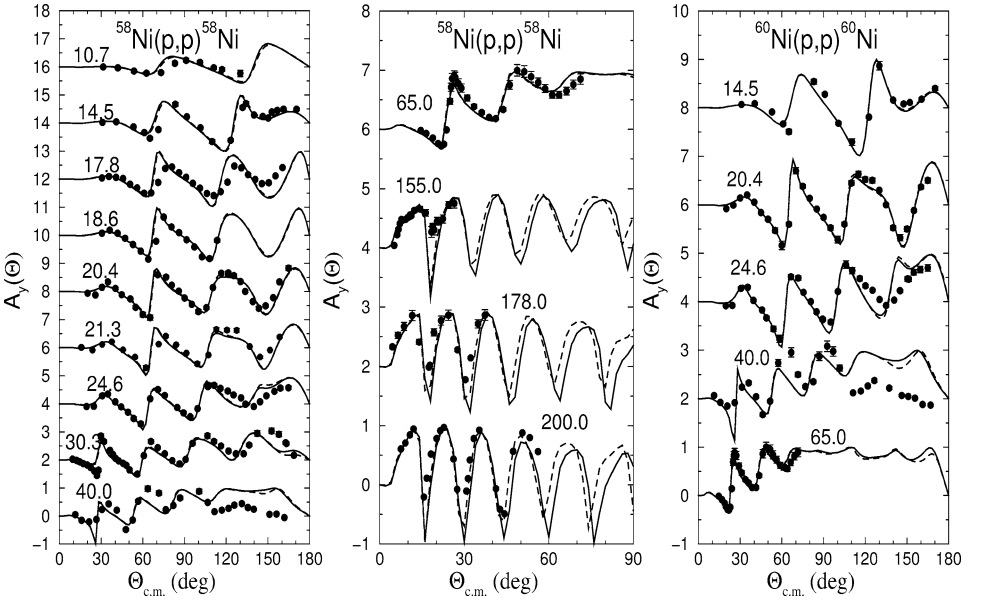

Fig. 40. Comparison of analyzing powers and experimental data, for protons scattered from ^{58,60}Ni. For more details, see Section 4.1.

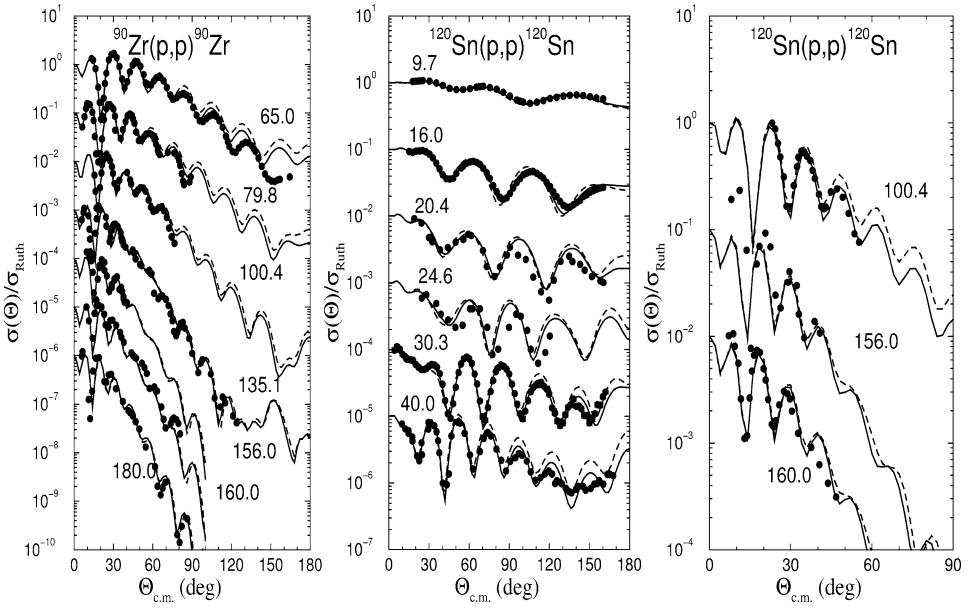

Fig. 41. Comparison of predicted differential cross sections and experimental data, for protons scattered from ^{90}Zr and ^{120}Sn. For more details, see Section 4.1.

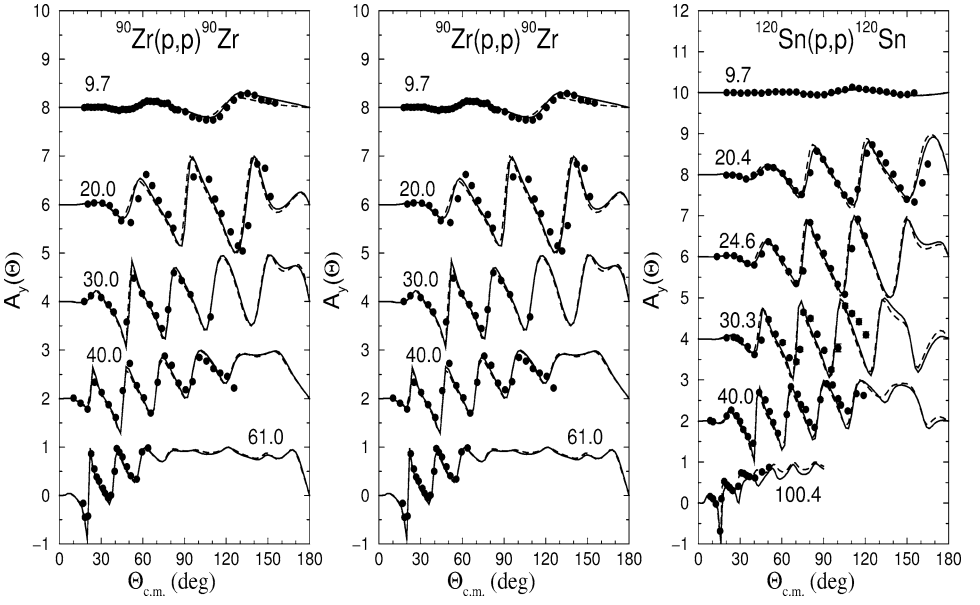

Fig. 42. Comparison of analyzing powers and experimental data, for protons scattered from ^{90}Zr and ^{120}Sn. For more details, see Section 4.1.

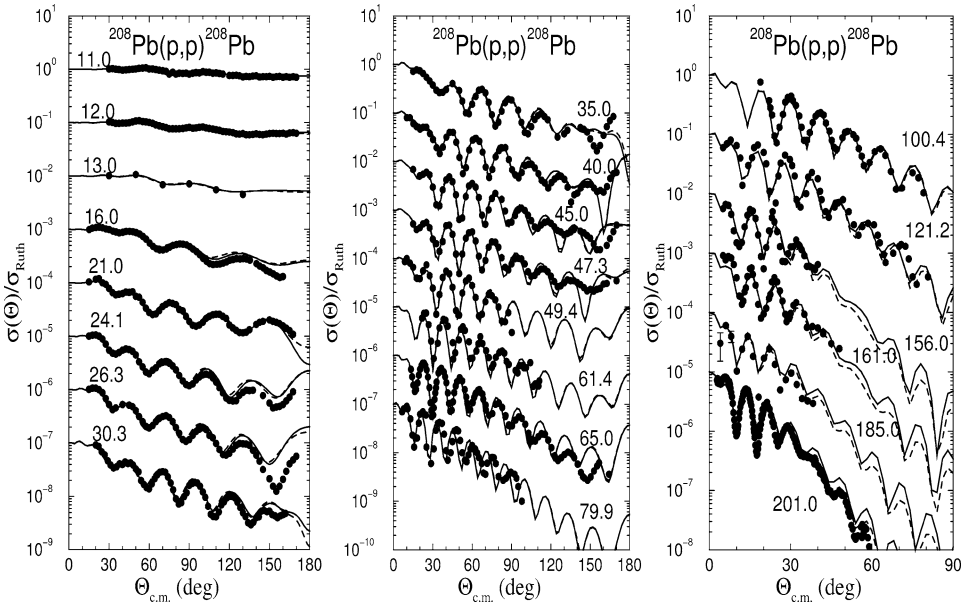

Fig. 43. Comparison of predicted differential cross sections and experimental data, for protons scattered from ^{208}Pb. For more details, see Section 4.1.

performance of an OMP over a large energy range. Apart from the first minima of the $\sigma(\theta)/\sigma_{\mathrm{Ruth}}$ calculations at high energies, the description is good. For ^{120}Sn the measured data at 156 and 160 MeV were arbitrarily renormalized by -20%. The agreement for A_y is satisfactory.

4.3.4. Pb *target*

The results for σ_R for this target is plotted in Fig. 32, $\sigma(\theta)/\sigma_{\mathrm{Ruth}}$ in Fig. 43, and A_y in Fig. 44.

Our OMP underestimates the total reaction cross section below about 25 MeV, as does the semi-microscopic OMP of Ref. [1]. However, our description of $\sigma(\theta)/\sigma_{\mathrm{Ruth}}$ is good in general. There are isolated phasing problems at 79.9 MeV, an overestimation at backward angles between 24 and 35 MeV and too much structure at backward angles between 40 and 50 MeV. The phasing of the A_y data is again very well described, but at high energies the extrema are not. The A_y data at 200 MeV form a rare example where the semi-microscopic approach of Ref. [1] performs better than our OMP does.

5. Building nucleon–nucleus OMPs

Up to now, we have built individual best fit OMPs separately for neutrons and protons incident on many (near-)spherical nuclei, with results shown in Figs. 2–44 and individual parameters gathered in Tables 3–6 and 8, 9.

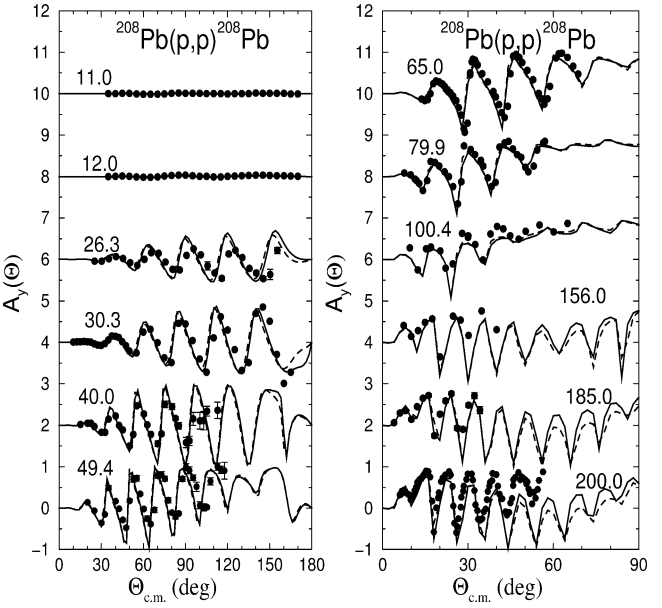

Fig. 44. Comparison of analyzing powers and experimental data, for protons scattered from ^{208}Pb. For more details, see Section 4.1.

When plotted versus A or $(N - Z)/A$, all these parameters display smooth patterns which can be modeled by closed forms or constant values. The natural next step is to optimize this mass dependence to obtain a global OMP. This will be done in two steps: First, we identify the asymmetry and Coulomb correction components of the potential. Next, we generate the global form of all the parameters. In all expressions with numerical parameters, units of fm and MeV are used.

5.1. Asymmetry- and charge-dependent components

The proton and neutron OMPs $\mathcal{U}_p$ and $\mathcal{U}_n$ that were optimized in Sections 3 and 4 on a nucleus-by-nucleus basis are combined to extract the isoscalar ($\mathcal{U}_0$) and asymmetry ($\mathcal{U}_1$) components of the nucleon–nucleus OMP. In general, the real central potential V is divided in an isoscalar component V_0 and an asymmetry component V_1 as follows:

$$V = V_0 \pm \alpha V_1, \tag{8}$$

with the asymmetry parameter $\alpha = (N - Z)/A$ and the upper (lower) sign is to be used for protons (neutrons). Here, we follow a method suggested by Mahaux and Sartor [11]. This states that the real part of the nuclear mean field felt by a nucleon in nuclear matter, whose energy would be equal to E in the absence of a Coulomb potential V_C and of neutron excess α is

$$\begin{aligned} V_n(E) &= V_0(E - \alpha V_1) + \alpha V_1, \\ V_p(E) &= V_0(E - V_C + \alpha V_1) - \alpha V_1, \end{aligned} \tag{9}$$

for neutrons and protons, respectively. Expanding the terms $V_n(E-\alpha V_1)$ and $V_p(E-\alpha V_1+V_C)$ to first order yields

$$V_1(E)=\left[2\alpha\frac{m^*}{m}(E)\right]^{-1}\big[V_n(E)-V_p(E+V_C)\big],$$
$$V_0(E)=V_n(E)-\alpha V_1(E)\left[1-\frac{\partial}{\partial E}V_n(E)\right], \tag{10}$$

with the effective mass

$$\frac{m^*}{m}(E)=1-\frac{1}{2}\frac{\partial}{\partial E}\big[V_n(E)+V_p(E+V_C)\big]. \tag{11}$$

For spherical nuclei, these components can be written as

$$V_1(r,E)=\left[2\alpha\frac{m_v^*}{m}(r,E)\right]^{-1}\big[V_{V,n}(r,E)-V_{V,p}(r,E+\overline{V}_C)\big],$$
$$V_0(r,E)=V_{V,n}(r,E)-\alpha V_1(r,E)\left[1-\frac{\partial}{\partial E}V_{V,n}(r,E)\right], \tag{12}$$

with

$$\frac{m_v^*}{m}(r,E)=1-\frac{1}{2}\frac{\partial}{\partial E}\big[V_{V,n}(r,E)+V_{V,p}(r,E+\overline{V}_C)\big], \tag{13}$$

where $\overline{V}_C$ is the Coulomb potential averaged over radial coordinates. Theoretically, the same method and reasoning may be adopted to achieve the decomposition of imaginary central components of the proton and neutron OMPs to produce isoscalar and isovector imaginary (surface and volume) potentials and related effective masses.

To obtain a practicable solution, we assumed that the effective masses related to real and imaginary potentials are constant and can be approximated by

$$\frac{m_V^*}{m}=\frac{m_{Wd}^*}{m}=\frac{m_{Wv}^*}{m}=1, \tag{14}$$

where m_{Wd}^*/m and m_{Wv}^*/m are the effective masses related to surface and volume imaginary potentials, respectively.

Adopting effective masses equal to unity hence from now, the neutron and proton OMPs may be expressed in terms of isoscalar and isovector components in a simple manner. For convenience, we abbreviate our notation and focus only on the E-dependence of the potential depths. The real well depths for incident neutrons and protons may be defined as follows [41]

$$V_{V,n}(E)=V_0(E)-\alpha V_1(E), \tag{15}$$
$$V_{V,p}(E)=\left[1-\overline{V}_C\frac{\partial}{\partial E}\right]\big[V_0(E)+\alpha V_1(E)\big], \tag{16}$$

where

$$\overline{V}_C=\frac{1.73}{r_C}\frac{Z}{A^{1/3}}, \tag{17}$$

assuming a uniform charge distribution of radius $R_C = r_C A^{1/3}$. The reduced Coulomb radius r_C takes on values which are not constant through the mass range of interest. It is parameterized as

$$r_C = 1.198 + 0.697\,A^{-2/3} + 12.994\,A^{-5/3}, \tag{18}$$

a closed form which results from a fit to r_C values deduced for many nuclei [42] from Hartree–Fock and Hartree–Fock–Bogoliubov predictions based on Gogny's D1S force [43].

In most phenomenological OMP analyses, V_1 is taken as a constant, and $V_{V,n}$, $V_{V,p}$ and V_0 for self-conjugate (i.e., $\alpha = 0$) nuclei (and implicitly V_0 for nuclei with $\alpha \neq 0$) as linear functions of energy [44,45]. In those OMPs, $V_{V,p}$ is expressed as

$$V_{V,p}(E) = V_0(E) + \alpha V_1 + \Delta V_C, \tag{19}$$

where ΔV_C is the so-called Coulomb correction term, which takes on constant values ranging from $\Delta V_C = 0.42Z/A^{1/3}$ MeV [46] to $\Delta V_C = 0.48Z/A^{1/3}$ MeV [47]. Since the E-dependence adopted in Eq. (7) for the real central potential depths breaks the linear E-dependence assumption, in our study ΔV_C is no longer constant. In principle, ΔV_C should be obtained together with $V_0(E)$ and $V_1(E)$ from solving Eqs. (15) and (16) simultaneously. This is not an easy task, so we have proceeded by making further approximations.

The first approximation concerns the E-dependences of $V_0(E)$ and $V_1(E)$. Microscopic calculations [48], semi-microscopic OMP calculations [1], and phenomenological analyses of quasi-elastic (p,n) scattering [49] suggest that $V_1(E)$ decreases smoothly with increasing energy. Since $V_{V,n}(E)$ and $V_{V,p}(E)$ are also decreasing functions of energy in our work, we make a second assumption, namely that $V_0(E)$ and $V_1(E)$ display the same E-dependence as that for $V_{V,n}(E)$ and $V_{V,p}(E)$. More explicitly, we assume that Eqs. (15) and (16) may be expressed as

$$\begin{aligned} V_{V,n}(E) &= (V_0 - \alpha V_1) g_n(E), \\ V_{V,p}(E) &= (V_0 + \alpha V_1)\left[1 - \overline{V}_C \frac{\partial}{\partial E}\right] g_p(E), \end{aligned} \tag{20}$$

where $g_n(E)$ and $g_p(E)$ are closed forms similar to that adopted for $V_V(E)$ in Eq. (7), and where the equality $g_n(E) = g_p(E)$ should hold for the sake of consistency with Eqs. (15) and (16). We have not been able to find g-functions which exactly fulfill the relation $g_n(E) = g_p(E)$. To some extent, this may be related to the Fermi energies, embedded in the closed forms (7), which take on distinct values for neutron and proton shells. However, we have found that the functions $g_n(E)$ and $g_p(E)$ as built from our local OMP parameters are close enough to make meaningful and successful analyses dealing with the establishment of nucleon–nucleus OMPs from proton and neutron OMPs. A careful analysis is indeed required since there are ambiguities in the determination of the asymmetry potential and Coulomb correction term, both of which are components of real central potentials.

A similar analysis may be applied to the absorptive potentials. For these potential components, information collected in earlier works is scarce and only qualitative in nature. To some extent, this is due to the precision with which the imaginary potentials were obtained from fits to proton and neutron scattering data. Usually, W_D and W_V values are

empirically determined to within at least 10%, while the level of uncertainty is typically of the order of 1% to 2% for V_V values. As a consequence, it appears difficult to deduce sound values simultaneously for the asymmetry and Coulomb correction components of the imaginary potentials, though attempts for $N = Z$ nuclides have been made [46,50,51]. Here, we have been able to extract the asymmetry component for the imaginary surface potential, assuming that the Coulomb correction term may be ignored, but have not been able to do so for the imaginary volume potential.

5.2. Global nucleon–nucleus OMP

As a first step, the global OMP analysis has been performed separately for neutron and proton scattering and reaction data. As soon as we found it possible for any of the neutron and proton potential parameters (except for the potential depths) to assign a common value, we decided to do so. Actually, these parameters were obtained after performing many trials during which the parameters tied with the adopted closed forms are tuned. We proceeded with these manual iterations until we obtained $g_n(E) \sim g_p(E)$ when solving Eqs. (15), (16).

5.2.1. Real central potential

For the real potential depths the results are

$$V_{V,n}(E) = [59.3 - 0.024\,A - 21.0\,\alpha] \times \left[1 - v_2^n\left(E - E_f^n\right) + v_3^n\left(E - E_f^n\right)^2 - v_4^n\left(E - E_f^n\right)^3\right], \tag{21}$$

with E_f^n, v_2^n, v_3^n, and v_4^n values in Table 10. Note that, in the spirit of a smooth global OMP, the Fermi energy E_f^n is now given by a global form. For protons, we have

$$V_{V,p}(E) = [59.3 - 0.024\,A + 21.0\,\alpha] \times \left[1 - v_2^p\left(E - E_f^p\right) + v_3^p\left(E - E_f^p\right)^2 - v_4^p\left(E - E_f^p\right)^3\right] + \Delta V_C(E), \tag{22}$$

with E_f^p, v_2^p, v_3^p, and v_4^p values in Table 11, and with the Coulomb correction term

$$\Delta V_C(E) = \overline{V}_C\left[v_2^p - 2v_3^p\left(E - E_f^p\right) + 3v_4^p\left(E - E_f^p\right)^2\right] \times [59.3 - 0.024\,A + 21.0\,\alpha]. \tag{23}$$

To study the effect of the E-dependent Coulomb correction term ΔV_C on the present OMP predictions, we have also performed an analysis with a constant Coulomb correction term for the real central potential, with value $\Delta V_C = 0.42Z/A^{1/3}$ (MeV). The overall description of proton scattering data with this constant Coulomb correction term was not as satisfactory as it is now with Eq. (23), especially for $E > 120$ MeV. It is worth mentioning that this particular energy dependence is taken into account in an effective way in the local OMP parameters for $V_V(E)$ of Eq. (7), which does not include an explicit Coulomb correction term.

The Coulomb correction term $\Delta V_C(E)$ of Eq. (23), for the ^{120}Sn target, and for energies between 20 and 200 MeV, is shown by the solid curve in Fig. 45. Evidently, ΔV_C

Table 10
Potential depth parameters and Fermi energy for the neutron global OMP of Eq. (40)

v_1^n	$= 59.30 - 21.0(N-Z)/A - 0.024\,A$	MeV
v_2^n	$= 0.007228 - 1.48 \times 10^{-6}\,A$	MeV^{-1}
v_3^n	$= 1.994 \times 10^{-5} - 2.0 \times 10^{-8}\,A$	MeV^{-2}
v_4^n	$= 7 \times 10^{-9}$	MeV^{-3}
w_1^n	$= 12.195 + 0.0167\,A$	MeV
w_2^n	$= 73.55 + 0.0795\,A$	MeV
d_1^n	$= 16.0 - 16.0(N-Z)/A$	MeV
d_2^n	$= 0.0180 + 0.003802/\big(1 + \exp[(A-156)/8]\big)$	MeV^{-1}
d_3^n	$= 11.5$	MeV
v_{so1}^n	$= 5.922 + 0.0030\,A$	MeV
v_{so2}^n	$= 0.0040$	MeV^{-1}
w_{so1}^n	$= -3.1$	MeV
w_{so2}^n	$= 160$	MeV
E_f^n	$= -11.2814 + 0.02646\,A$	MeV

Table 11
Potential depth parameters and Fermi energy for the proton global OMP of Eq. (41). The parameter values for neutrons are given in Table 10. $\overline{V}_C$ appears in the Coulomb correction term $\Delta V_C(E)$ (see Eq. (23)), of the real central potential

v_1^p	$= 59.30 + 21.0(N-Z)/A - 0.024\,A$	MeV
v_2^p	$= 0.007067 + 4.23 \times 10^{-6} A$	MeV^{-1}
v_3^p	$= 1.729 \times 10^{-5} + 1.136 \times 10^{-8} A$	MeV^{-2}
v_4^p	$= v_4^n$	MeV^{-3}
w_1^p	$= 14.667 + 0.009629\,A$	MeV
w_2^p	$= w_2^n$	MeV
d_1^p	$= 16.0 + 16.0(N-Z)/A$	MeV
d_2^p	$= d_2^n$	MeV^{-1}
d_3^p	$= d_3^n$	MeV
v_{so1}^p	$= v_{so1}^n$	MeV
v_{so2}^p	$= v_{so2}^n$	MeV^{-1}
w_{so1}^p	$= w_{so1}^n$	MeV
w_{so2}^p	$= w_{so2}^n$	MeV
E_f^p	$= -8.4075 + 0.01378\,A$	MeV
$\overline{V}_C$	$= 1.73/r_C Z A^{-1/3}$	MeV

behaves nearly as a linear function and with values ranging from 0.5 MeV to 5.5 MeV. For comparison, this figure also includes the usual $\Delta V_C = 0.42\,Z/A^{1/3}$ constant value (dashed line). From this comparison, we suggest that most earlier OMP analyses focusing on proton data available over a narrow energy range, typically $E = 15$–30 MeV, led to

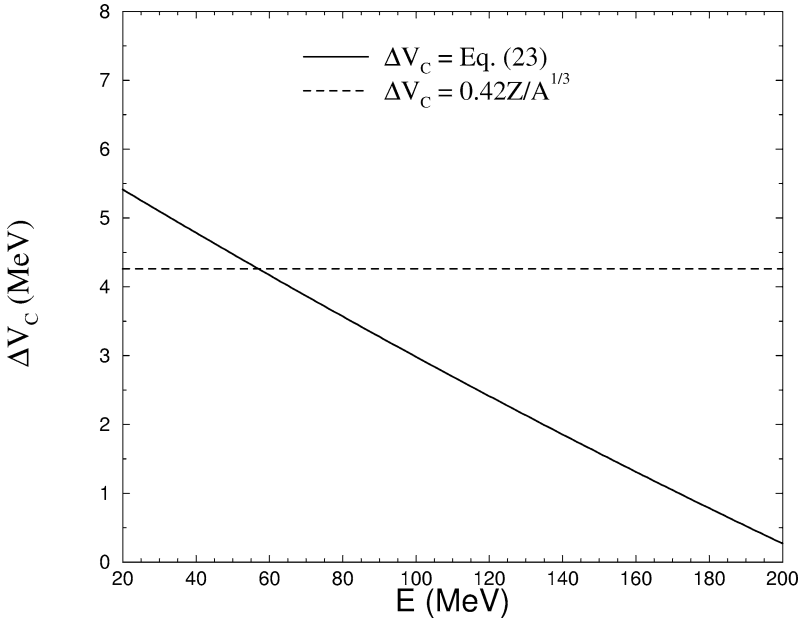

Fig. 45. Energy dependent Coulomb correction term, see Eq. (23), of our global OMP (solid line) versus constant Coulomb correction (dashed line), for ^{120}Sn.

ambiguous results for the determination of both asymmetry and Coulomb correction OMP components.

In this work, it was implicitly assumed from the beginning that the real asymmetry potential V_1 has a volume shape, like in most previous OMP studies [41]. To first order in $(E - E_f)$, the V_1 depth of Eqs. (21), (22) is a linear function of incident energy, namely

$$V_1(E) \approx 21 - 0.15\,E, \tag{24}$$

assuming a mean Fermi energy value of $\langle E_f \rangle \sim -6$ MeV. This estimate is in rather good agreement with results from (p, n) reactions to isobaric analogue states, as summarized in Ref. [52] and from previous (n, n) and (p, p) scattering data analyses [53]. Values determined with Eq. (24) are also in fair agreement with predictions from nuclear matter calculations [48], provided they are renormalized to match (p, n) quasi-elastic scattering data [3].

We found it necessary to consider the isoscalar component V_0 of our global OMP to be slightly A-dependent. Such an A-dependence was mentioned previously for single-particle bound state calculations [19], and also in proton scattering analyses [41], where a possible hidden isospin effect was suggested. In this work, it automatically emerges from the local OMPs. The found well depths of the real central potential can only be reproduced by a global OMP if the separation between an asymmetry term and a term linear in A as in Eq. (21) is adopted. Otherwise, a too large asymmetry strength will induce too large differences in V_0 values along isotopic chains. Moreover, it will never account for the proper asymmetry term necessary to describe proton scattering. Note that the linear A-term

does not change sign for protons. Thus, contrary to the previous point of view [54], which stated that the quality of the existing experimental database was insufficient to isolate such a term, we have now been able to extract the linear A-term of $V_V(E)$ in the global OMP as a true effect. The linear A-dependence is also necessary to compensate for the increase of r_V with mass, which has also been clearly identified in our grid search on a nucleus by nucleus basis.

Next, we discuss the geometrical parameters, which are displayed in Fig. 46. In our global OMP, r_V is parameterized as

$$r_V = 1.3039 - 0.4054\,A^{-1/3}. \tag{25}$$

This functional form was also adopted in the global OMP of Varner et al. [4], and has been confirmed by parameterizations of nuclear charge radii [55] and by folding models of the nucleon–nucleus potential. On average, the r_V values of Eq. (25) are between 0.01 and 0.03 fm higher than those of Ref. [4]. This difference may result from the fact that our global value is based on individually obtained parameters, as opposed to a value obtained from one global fit to all experimental data. Also, besides the elastic scattering angular distributions and analyzing powers used in Ref. [4], we also included total (reaction) cross sections and average resonance parameters in the process to obtain our OMPs. The diffuseness parameter of the volume potentials decreases with mass as

$$a_V = 0.6778 - 1.487 \times 10^{-4} A. \tag{26}$$

This formula shows that the difference between the a_V parameters of the lightest and heaviest nuclides in our study is only about 0.03 fm. We mention here that, for the sake of predictive performance, the global values a_V of Eq. (26) are slightly less than those that would result from a best-fit curve through the data, as can be observed in Fig. 46. Arguably, this means that there are still some cross-correlations in the parameterization of the real central potential to be uncovered. The overall effect of the mass dependence of the potential depths and geometries will be further discussed in Section 6, where we examine the volume integrals.

5.2.2. Imaginary central potential

The global functional form for volume absorption is

$$W_{V,n}(E) = w_1^n \frac{(E - E_f^n)^2}{(E - E_f^n)^2 + (w_2^n)^2}, \tag{27}$$

with w_1^n and w_2^n values in Table 10 for incident neutrons, and

$$W_{V,p}(E) = w_1^p \frac{(E - E_f^p)^2}{(E - E_f^p)^2 + (w_2^p)^2}, \tag{28}$$

with w_1^p and w_2^p values in Table 11 for incident protons. We find an asymptotic parameter w_1 that is approximately 2 MeV higher for protons than for neutrons. The decomposition of the volume absorption into isoscalar and isovector components has also been investigated. We failed in this attempt because W_V is not well constrained by the proton scattering and reaction data available beyond $E = 150$ MeV. Invoking a Coulomb correction term

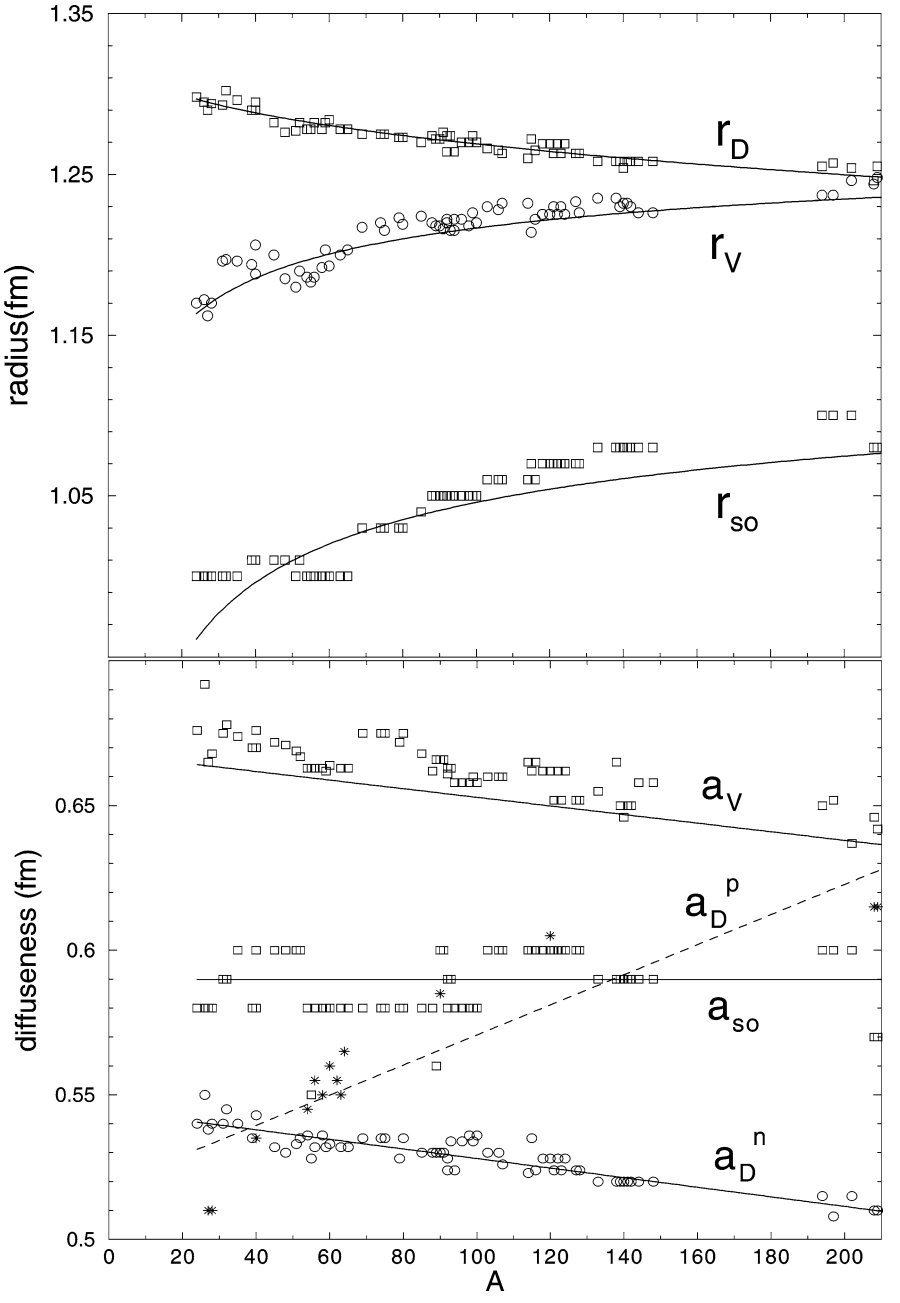

Fig. 46. Reduced radius and diffuseness parameter of the volume (V), surface (D), and spin–orbit (SO) potentials. The symbols represent the values of our local OMPs, see Tables 3–6, and the solid lines those of the global OMP, see Eqs. (25), (26), (31)–(33), (36) and (37). The solid stars and the associated dashed line correspond to the proton surface diffuseness parameter a_D of Eq. (33).

for volume absorption would be counter-productive: it is negative since W_V increases with incident energy. There is a slight A-dependence in the parameters that drive W_V. The increase with mass of w_1 is consistent with the mass independence of the imaginary volume integral, as confirmed recently in a semi-microscopic approach [1]. We have not found evidence that this mass dependence could simulate the need for an asymmetry term. For completeness, we repeat here that $W_V(E)$ is associated with the same geometry as that for $V_V(E)$.

For surface absorption we obtain

$$W_{D,n}(E) = \big[16.0 - 16.0\,\alpha\big]\frac{(E - E_f^n)^2}{(E - E_f^n)^2 + (d_3^n)^2}\exp\big[-d_2^n\big(E - E_f^n\big)\big], \tag{29}$$

with d_2^n and d_3^n values in Table 10, and

$$W_{D,p}(E) = \big[16.0 + 16.0\,\alpha\big]\frac{(E - E_f^p)^2}{(E - E_f^p)^2 + (d_3^p)^2}\exp\big[-d_2^p\big(E - E_f^p\big)\big], \tag{30}$$

with d_2^p and d_3^p values in Table 11. Note that we have not included a Coulomb correction term, ΔW_C, for the imaginary surface potential. Since W_D is not determined with a precision better than 10% to 20% from our fitting procedure, as pointed out before, the extracted ΔW_C values are ill defined, so we found it better to set $\Delta W_C = 0$.

For incident neutrons, the reduced radius and diffuseness parameters for surface absorption both decrease with mass

$$r_D = 1.3424 - 0.01585\,A^{1/3}, \tag{31}$$

$$a_D^n = 0.5446 - 1.656 \times 10^{-4} A. \tag{32}$$

For incident protons we had to adopt a surface diffuseness parameter a_D which increases with mass and which is generally larger than a_D for neutrons,

$$a_D^p = 0.5187 + 5.205 \times 10^{-4} A. \tag{33}$$

This was necessary to obtain a satisfactory fit of the proton reaction cross sections. A possible explanation for this has been given by Satchler [41] and Menet et al. [56], who postulate an asymmetry term in the surface diffuseness parameter.

5.2.3. Spin–orbit potential

The complex proton and neutron *SO* potentials vary similarly in depths and radial shapes, as was deduced earlier in a systematic semi-microscopic analysis [1,3]. Following conclusions of that work, here we make the assumption that the *SO* potential components are identical for both incident neutrons and protons. For incident neutrons the real *SO* potential has the form

$$V_{SO}(E) = v_{so1}^n \exp\big[-v_{so2}^n\big(E - E_f^n\big)\big], \tag{34}$$

with v_{so1}^n and v_{so2}^n values in Table 10. The same expression holds for protons. The imaginary *SO* potential depth for incident neutrons has the form

$$W_{SO}(E) = w_{so1}^n \frac{(E - E_f^n)^2}{(E - E_f^n)^2 + (w_{so2}^n)^2}, \tag{35}$$

with w^n_{so1} and w^n_{so2} values in Table 10. The same expression holds for protons. We found no mass dependence of the $W_{SO}(E)$ parameters. The mass dependence of r_{SO} is similar to that of r_V, namely

$$r_{SO} = 1.1854 - 0.647\, A^{-1/3}, \tag{36}$$

and the *SO* diffuseness parameter has a constant value

$$a_{SO} = 0.59. \tag{37}$$

The rather low global r_{SO} curve in Fig. 46 results from the large number of individual r_{SO} values at lower masses and the adopted functional form (36). This induces a too low global r_{SO} value for the heavy nuclides. Nevertheless, the impact is small. Finally, we ignore the Coulomb *SO* potential (also known as Mott–Schwinger potential) which for incident neutrons impacts the OMP predictions in a significant way only at very forward angles of differential cross sections and analyzing powers [1].

5.3. Results for global optical model

5.3.1. Neutrons

The results of our global neutron OMP are shown as dashed curves in Figs. 2–31 where they are compared with local OMP calculations and scattering and reaction data. Apparently, the global OMP results are nearly as good as those based on local OMPs of the present work, and describe the whole data set as well. The only conspicuous deviations from the local OMP results and from the experimental data can be found for neutron total cross sections below 1 MeV. Also, for some elastic scattering angular distributions at backward angles the difference is non-negligible. For some individual nuclides (^{27}Al, ^{28}Si, ^{48}Ti, and ^{51}V) the global OMP underestimates the local OMP results whereas for a few others ($^{96-100}$Mo) there is a slight overestimation. Indeed, the dispersion of individual nuclide parameters around the average is the largest for the surface absorption W_D, which is responsible for this behaviour. Thus we have not been able to globalize W_D as well as the other OMP parameters. For analyzing powers, the local and global OMP results are practically identical.

We are particularly pleased to see that the global OMP prediction of the neutron total cross section above 5 MeV hardly differs from that by a local OMP. Therefore, we expect our global OMP to predict neutron total cross sections in the 5 to 200 MeV range for spherical or slightly deformed nuclei with an accuracy of 2%. Additional neutron total cross section measurements in this energy range, and in the "empty" mass ranges $65 < A < 89$, $100 < A < 115$, and $124 < A < 150$, would be welcomed to test this statement.

In Table 12 we compare results from our global neutron OMP with the well-known other global optical models of Wilmore–Hodgson [57], Rapaport et al. [47], Varner et al. [4], Walter–Guss [58], and Madland [59] on a χ^2/N (per point) basis. The results are based on all experimental elastic angular distributions and total cross sections sets considered in this paper, thus covering the whole range of interest. When judged with this numerical criterion, our global OMP appears to perform better than each of the listed models, even when the comparison is restricted to only those measurements that fall in

Table 12
Comparison of our global neutron OMP ($0.001 < E < 200$ MeV, $24 \leqslant A \leqslant 209$) with other global potentials. The χ^2 per point are given as separate averages for all elastic scattering angular distributions ($\chi^2_{\rm ad}$) and total cross sections ($\chi^2_{\rm tot}$) presented in this paper. To obtain this table, our global OMP was tested for observables in the mass and energy ranges for which the older optical models were claimed to be valid. The unlabeled χ^2/N refers to the performance of the OMPs listed in the first column. The χ^2/N labeled by (this) refers to our global OMP in the same mass and energy range

OMP	A	E (MeV)	$\chi^2_{\rm ad}/N$	$\chi^2_{\rm ad}/N$ (this)	$\chi^2_{\rm tot}/N$	$\chi^2_{\rm tot}/N$ (this)
Wilmore–Hodgson [57]	40–208	0−15	11.2	7.4	9.2	6.7
Rapaport et al. [47]	40–208	7−26	10.0	7.0	4.1	1.8
Varner et al. [4]	40–208	7−26	8.3	7.0	4.7	1.8
Walter–Guss [58]	53–208	10−80	6.3	6.1	2.3	1.3
Madland [59]	40–208	50−200	8.6	4.5	6.9	1.2

the latter (narrower) mass and energy range of applicability. Thus, we are not punished for adopting a too large energy range for our model. Only the Walter–Guss OMP [58] for elastic scattering angular distributions in the 10 to 80 MeV range comes close to our performance, but in that case, as with the other listed OMPs, the improvement obtained by our global OMP for total cross sections is significant.

An additional validation of our global neutron OMP is provided by average resonance parameters, namely the s- and p-wave strength functions S_0 and S_1 and the potential scattering radius R'. The corresponding experimental data [60] are shown in Fig. 47 together with the global OMP predictions. The exact energy at which these quantities need to be evaluated depends on the availability of measured resonances and thus changes from nucleus to nucleus. Therefore, three predictions are given in Fig. 47, for 1, 10 and 100 keV, respectively, which sheds light on the energy dependence of these quantities.

Each of these average resonance parameters displays a gross structure when plotted against mass number, which is reasonably well described by our global OMP calculations. However, several deviations between measurements and predictions are observed. First, we find an underestimation of R' in the $90 < A < 136$ mass range, where many nuclides display complex collective properties (i.e., anharmonic vibrations and tri-axial rotation), features which are ignored in our spherical model approach. Second, the predicted S_1 values seem too high, especially around $A = 60$. This overall scale problem may easily be remedied by increasing the sharp-edge radius R_s, employed while calculating the p-wave penetrability factor, beyond the value $R_s = 1.35A^{1/3}$ (fm) that is traditionally adopted [60]. Finally, the s-wave strength function is overpredicted throughout the range $90 < A < 136$. Again, this may stem from ignoring coupling to collective levels in our model, and may also point to the need for inclusion of l-dependent components in phenomenological OMPs (which indeed would alter both S_0 and S_1 predictions). The physics underlying the present OMP may entail that even though our global OMP yields the correct total cross sections in the keV region for these nuclides, see Fig. 15, its division into a shape-elastic part and a reaction part for these energies and nuclides may not be precise.

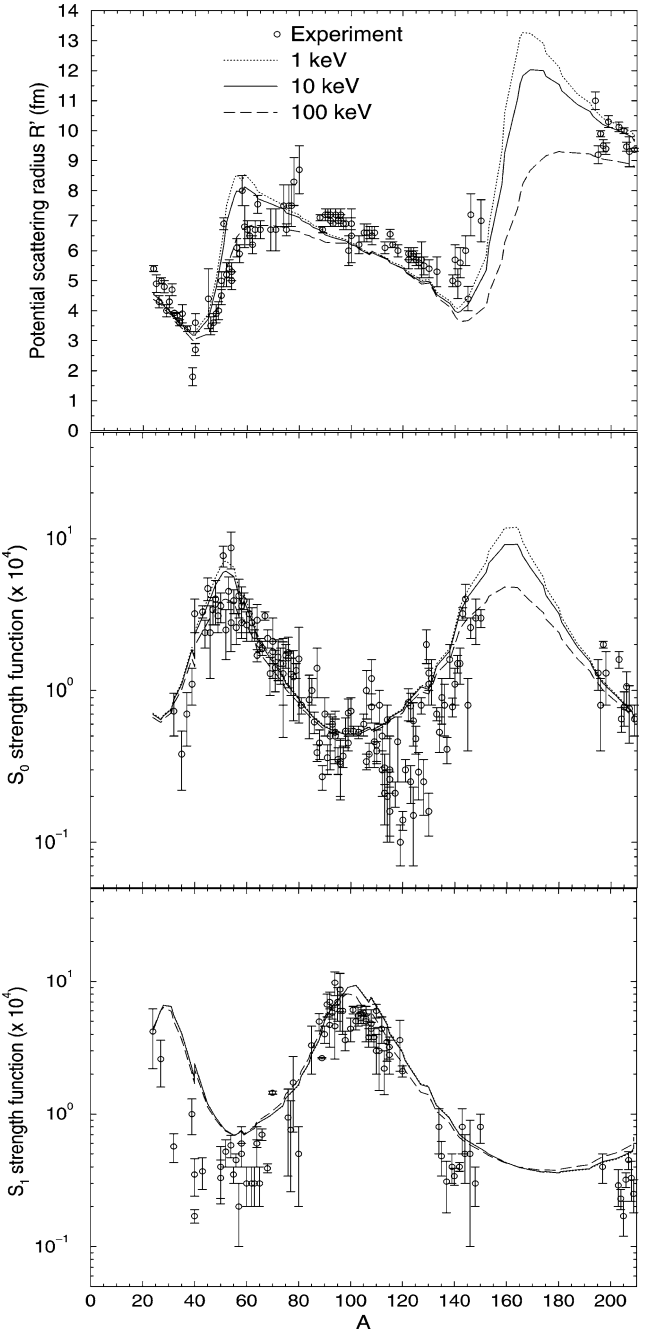

Fig. 47. Potential scattering radius (R') and s- and p-wave strength functions (S_0 and S_1) as predicted by our global neutron OMP at 1 keV (dotted curves), 10 keV (solid curves), and 100 keV (dashed curves). The experimental data (symbols) were taken from Ref. [60].

5.3.2. Protons

Predictions based on our global OMP are shown as dashed curves in Figs. 33–44 where they are compared with local OMP predictions and scattering data. Per nucleus, the difference between the local and global OMP predictions is somewhat larger than for incident neutrons. Again, the difference is most pronounced at the backward angles of angular distributions. For relatively light nuclides, below say $A = 56$, and the heavy masses around $A = 208$, the global proton OMP produces backward angular distributions lower than those predicted by the local OMPs, whereas for masses in the $A = 90$–120 region the situation is reversed. As for neutrons, the globalization of the absorption parameters W_D is the most difficult, since the dispersion of the local parameters for W_D around the average is rather large. For the A_y data of ^{58}Ni, there is an interesting deviation from the local OMP at the highest incident energies. Finally, the difference between the local and global OMP predictions for reaction cross sections, shown in Fig. 32 is relatively small.

6. Integral properties: volume integrals

The volume integrals J_i/A are relatively invariant functions of the OMP parameters and give insight in the behaviour of the optical potentials as a function of mass and energy. With phenomenologically determined OMPs, the energy or mass dependence of the potential depths may be compensated by that of the geometry parameters, thereby masking particular structure effects. Such effects may become more visible by means of volume integrals. They are also particularly helpful to compare OMP predictions from separate analyses, e.g., (semi-)microscopic approaches where the density distribution of the nucleus is not represented in a simple analytical form.

Defining

$$y_i = \left(\frac{\pi a_i}{R_i}\right)^2, \tag{38}$$

where the index i can be V (volume) or D (surface), then to a good approximation for Woods–Saxon based potentials the volume integrals per nucleon for the various potentials are given by

$$\begin{aligned}
J_V/A &= \frac{4}{3}\pi\left(R_V^3/A\right)V_V(1+y_V),\\
J_{W_V}/A &= \frac{4}{3}\pi\left(R_V^3/A\right)W_V(1+y_V),\\
J_{W_D}/A &= 16\pi a_D\left(R_D^2/A\right)W_D\left(1+\frac{1}{3}y_D\right),\\
J_W/A &= J_{W_V}/A + J_{W_D}/A.
\end{aligned} \tag{39}$$

Figs. 48 and 49 display some properties of the volume integrals, both for the local OMPs and the global OMP, as a function of mass and energy. For neutrons at not too high incident energies, we observe the known [46] decrease of both J_V/A and J_W/A with mass. At 200 MeV, J_W/A is practically constant with mass and we therefore suggest that the

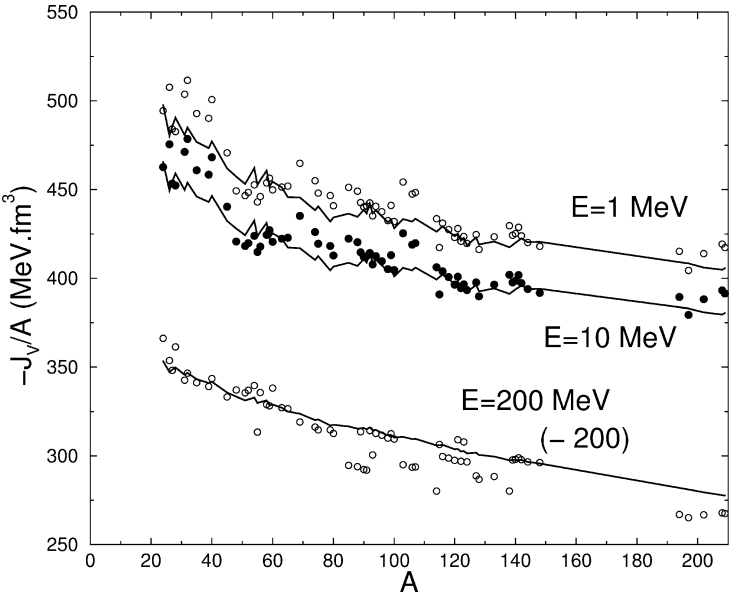

Fig. 48. Volume integrals for neutron-induced reactions for the real central potential as a function of mass, plotted at three different energies. The symbols correspond to the values of the local OMPs while the solid curves represent the global OMP (the curves in the deformed region, $148 < A < 194$ can be discarded).

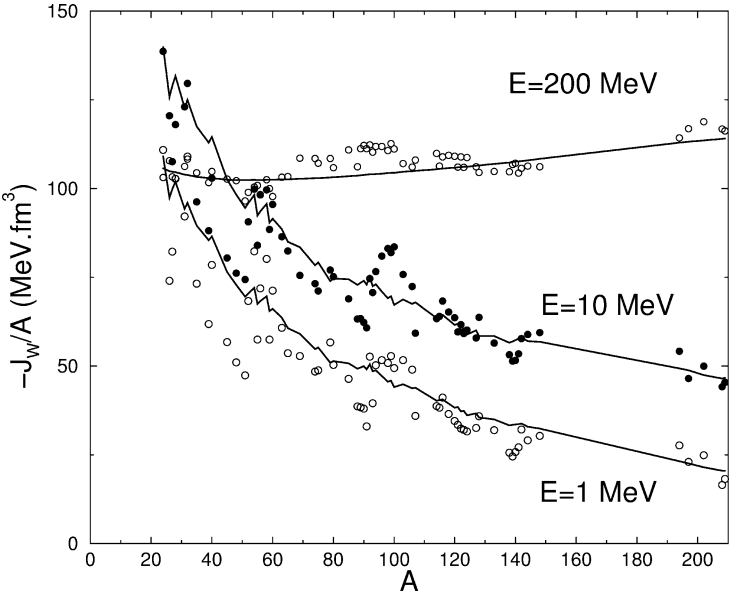

Fig. 49. Volume integrals for neutron-induced reactions for the imaginary central potential as a function of mass, plotted at three different energies. The symbols correspond to the values of the local OMPs while the solid curves represent the global OMP (the curves in the deformed region, $148 < A < 194$ can be discarded).

imaginary asymmetry potential is weak. This in line with the Dirac approach of Ref. [12], where calculated proton volume integrals J_W/A for ^{40}Ca and ^{208}Pb show the same energy and mass dependence as does Fig. 49. Hence, at the upper energy end of the applicability range of our OMPs, we seem to have a sound connection with the relativistic high-energy model predictions.

Another conspicuous feature of J_W/A is the pronounced structure in the transition region around mass $A = 100$, at low energies. The somewhat anomalous W_D parameters for these deformed nuclides were already reported in Section 4, and these parameters are responsible for the deviation from the global average. The global OMP does not exhibit this structure, which is in line with the deviation of the local versus global OMP predictions for elastic scattering angular distributions in this mass range.

7. Conclusions

We have presented new OMPs for incident neutrons and protons with energies from 1 keV up to 200 MeV, for (near-)spherical nuclides in the mass range $24 \leqslant A \leqslant 209$. Our negative experience with fully automatic least-square searches for OMP parameters has led us to use a new computational steering technique, which has enabled us to obtain OMP parameters for many individual nuclides. All nuclei have thereby been treated on the same footing, and the resulting OMP parameters all scatter around physically justified averages.

The parameterization of our local OMPs is given by Eq. (7), with parameters for incident neutrons given in Tables 3–6, and parameters for incident protons given in Tables 8, 9. In sum, the key properties of our local OMPs are:

(i) A unique functional parameterization for the OMP that can successfully be applied in a large part of the periodic table of elements, and over an unprecedented energy range,
(ii) A constrained set of OMP parameters, obtained by simultaneously analyzing all different types of observables over a wide range of energies, and including both compound nucleus and relativistic effects, and
(iii) No unphysical freedom of geometry parameters. The real and imaginary parts of each (volume, surface, spin–orbit) component of the potential share the same radius and diffuseness parameters which are both E-independent. We mention here that this geometry constraint differs from that adopted in the global optical models of, e.g., Refs. [4–47], which assume equal geometry parameters for $\mathcal{W}_V$ and $\mathcal{W}_D$ and different geometry parameters for $\mathcal{V}_V$.

Out of the local OMPs we have developed a global nucleon OMP that, in terms of predicting measured data, comes remarkably close to the performance of the local OMPs. We have been able to disentangle asymmetry, Coulomb correction and mass-dependent components of the global OMPs.

The global neutron OMP for $0.001 \leqslant E \leqslant 200$ MeV and $24 \leqslant A \leqslant 209$ is given by

$$V_V(E) = v_1^n\big[1 - v_2^n\big(E - E_f^n\big) + v_3^n\big(E - E_f^n\big)^2 - v_4^n\big(E - E_f^n\big)^3\big],$$

$$
\begin{aligned}
&W_V(E) = w_1^n \frac{(E-E_f^n)^2}{(E-E_f^n)^2+(w_2^n)^2},\\
&r_V = 1.3039 - 0.4054\,A^{-1/3},\\
&a_V = 0.6778 - 1.487\times 10^{-4}\,A,\\
&W_D(E) = d_1^n \frac{(E-E_f^n)^2}{(E-E_f^n)^2+(d_3^n)^2}\exp\bigl[-d_2^n(E-E_f^n)\bigr],\\
&r_D = 1.3424 - 0.01585\,A^{1/3},\\
&a_D = 0.5446 - 1.656\times 10^{-4}A,\\
&V_{SO}(E) = v_{so1}^n \exp\bigl[-v_{so2}^n\bigl(E-E_f^n\bigr)\bigr],\\
&W_{SO}(E) = w_{so1}^n \frac{(E-E_f^n)^2}{(E-E_f^n)^2+(w_{so2}^n)^2},\\
&r_{SO} = 1.1854 - 0.647\,A^{-1/3},\\
&a_{SO} = 0.59,
\end{aligned}
\tag{40}
$$

where the units are in fm and MeV and the parameters for the potential depths and E_f^n are given in Table 10.

The global proton OMP is given by

$$
\begin{aligned}
&V_V(E) = v_1^p\bigl[1 - v_2^p\bigl(E-E_f^p\bigr) + v_3^p\bigl(E-E_f^p\bigr)^2 - v_4^p\bigl(E-E_f^p\bigr)^3\bigr]\\
&\qquad + \overline{V}_C.v_1^p\bigl[v_2^p - 2v_3^p\bigl(E-E_f^p\bigr) + 3v_4^p\bigl(E-E_f^p\bigr)^2\bigr],\\
&W_V(E) = w_1^p \frac{(E-E_f^p)^2}{(E-E_f^p)^2+(w_2^p)^2},\\
&r_V = 1.3039 - 0.4054\,A^{-1/3},\\
&a_V = 0.6778 - 1.487\times 10^{-4}\,A,\\
&W_D(E) = d_1^p \frac{(E-E_f^p)^2}{(E-E_f^p)^2+(d_3^p)^2}\exp\bigl[-d_2^p\bigl(E-E_f^p\bigr)\bigr],\\
&r_D = 1.3424 - 0.01585\,A^{1/3},\\
&a_D = 0.5187 + 5.205\times 10^{-4}A,\\
&V_{SO}(E) = v_{so1}^p \exp\bigl[-v_{so2}^p\bigl(E-E_f^p\bigr)\bigr],\\
&W_{SO}(E) = w_{so1}^p \frac{(E-E_f^p)^2}{(E-E_f^p)^2+(w_{so2}^p)^2},\\
&r_{SO} = 1.1854 - 0.647\,A^{-1/3},\\
&a_{SO} = 0.59,\\
&r_C = 1.198 + 0.697\,A^{-2/3} + 12.994\,A^{-5/3},
\end{aligned}
\tag{41}
$$

where the parameters for the potential depths, $\overline{V}_C$ and E_f^p are given in Table 11. The functional form of the proton global OMP differs from the neutron global OMP only by the Coulomb correction term in $V_V(E)$, which has been derived in Section 5.

In addition to the aspects mentioned for local OMPs, the key properties of our global OMPs are:

(i) The first global optical model that is obtained from a grid search based on local optical models for individual nuclides,
(ii) A global optical model that is applicable at any energy up to 200 MeV, and that compares favorably to other global optical models, in terms of predictive power, and
(iii) For the real central potential, isolation of the asymmetry strength from a plain A-dependent term and, in the case of protons, a theoretically fixed Coulomb correction component which is E-dependent (as it should). On the other hand, we have not been able to identify unambiguously Coulomb correction terms in the imaginary potentials.

The E-dependence that we have adopted for the absorptive potentials suggests an obvious extension of our work: including dispersion relations. The absence of dispersive corrections in the present paper can be inferred from the absence of a real surface term $\mathcal{V}_D$ in Eq. (1) or, equivalently, an effective E-dependent radius of the real volume potential. We note that our potential already fulfills the convenient condition that the real and imaginary components of the volume potential have the same geometry. Indeed, we have obtained preliminary dispersive OMPs for all nuclides as well as a global dispersive OMP, but leave this as the subject of another paper. Surprisingly, there are indications that the inclusion of dispersion relations improves the description of the data in some mass regions (e.g., around $A = 140$) but worsens the agreement in others (e.g., around $A = 95$). Also, we expect that the method of this paper will also work for deformed nuclides or for composite particle scattering (though we need a big compiled experimental database for the latter, which is lacking). A formal extension to light nuclides is also possible, in terms of fitting data, but the resulting OMPs will have less physical meaning. Finally, we think that the OMPs presented in this paper may serve as a starting point for the development of Lane-consistent OMPs, which will then enable a proper description of (p, n) reactions to isobaric analogue states.

The potentials developed in this paper may find direct application in theoretical nuclear model calculations, and are available from the Reference Input Parameter Library [8] as well as directly from the authors [9]. The recipe for using our work is straightforward: use a local OMP whenever it is available from the tables and use the global OMP otherwise.

We have used a huge experimental database, with all types of observables that are necessary to constrain an OMP, to minimize the deviation of calculation from measurement. Nevertheless, there are still some gaps in the existing database, which should be filled to enable further exploration of the nucleon–nucleus interaction. Examples are additional total cross section measurements, as mentioned in Section 5.3, and neutron elastic scattering at high energies. Before long, 96 MeV $d\sigma/d\Omega$ for neutrons incident on Fe and Pb will be available from Uppsala University (HINDAS project) that will further test the correctness of the asymmetry strength, and its E-dependence, of our potential.

We have attempted to push the phenomenological OMP to the limit, without resorting to unphysical parameter values or dependencies to mimic unknown physics. This means

that, until evidence to the contrary is provided, a better description of measurements with a phenomenological Woods–Saxon model can only be obtained by relaxing the parameter constraints (for example, by introducing an E-dependent geometry to describe low-energy neutron scattering in the Fe mass region), which may nevertheless be valuable in applied physics. The other way forward is, obviously, the microscopic optical model. The performance of models in which the nucleon–nucleon interaction and the matter density distribution are folded to give a direct measure of the shape and strength of the nuclear potential, is in principle less dependent on the particular nucleus under study than that of the phenomenological OMP. Hence, for nuclei far from stability, for which no experimental data exist, it is arguably safer to make qualitative statements about the predictive power of a microscopic OMP than with a phenomenological OMP. Our phenomenological OMP has only been tested for well-studied nuclei and is therefore only *at least* reliable in the neighborhood of these nuclei. We hope that the mass- and E-dependencies of our potentials and related integral properties provide new inspiration for the improvement of microscopic optical models.

Acknowledgements

This work was partly supported by the HINDAS project of the 5th Euratom Framework Programme, contract no. FIKW-CT-2000-0031. We thank Dr. E. Bauge for providing us with many references for experimental data, Dr. J. Raynal for his continuous effort in extending his ECIS-code according to our wishes, Dr. J.J. van Wijk for the construction of ECISVIEW, and the referee for useful comments. A. Koning wishes to thank CEA Bruyères-le-Châtel for the support and hospitality during his stay.

References

[1] E. Bauge, J.P. Delaroche, M. Girod, Phys. Rev. C 58 (1998) 1118.
[2] K. Amos, P.J. Dortmans, H.V. von Geramb, S. Karataglidis, J. Raynal, in: J.W. Negele, E. Vogt (Eds.), Advances in Nuclear Physics, Vol. 25, Plenum, New York, 2000, and references therein.
[3] E. Bauge, J.P. Delaroche, M. Girod, Phys. Rev. C 63 (2001) 024607.
[4] R.L. Varner, W.J. Thompson, T.L. McAbee, E.J. Ludwig, T.B. Clegg, Phys. Rep. 201 (1991) 57.
[5] A.J. Koning, J.J. van Wijk, J.P. Delaroche, in: Proceedings of the OECD/NEA Specialists' Meeting on the Nucleon Nucleus Optical Model up to 200 MeV, Bruyères-le-Châtel, 1996, p. 111, available at http://www.nea.fr/html/science/om200/.
[6] J. Raynal, Notes on ECIS94, CEA Saclay Report No. CEA-N-2772, 1994.
[7] C.M. Perey, F.G. Perey, At. Data Nucl. Data Tables 13 (1974) 293;
C.M. Perey, F.G. Perey, At. Data Nucl. Data Tables 17 (1974) 1.
[8] P.G. Young, Handbook for Calculations of Nuclear Reaction Data: Reference Input Parameter Library, IAEA-TECDOC-1034, 1998, p. 41.
[9] A.J. Koning, unpublished, e-mail: koning@nrg-nl.com.
[10] G. Audi, A.H. Wapstra, Nucl. Phys. A 595 (1995) 409.
[11] C. Mahaux, R. Sartor, in: J.W. Negele, E. Vogt (Eds.), Advances in Nuclear Physics, Vol. 20, Plenum, New York, 1991.
[12] S. Hama, B.C. Clark, E.D. Cooper, H.S. Sherif, R.L. Mercer, Phys. Rev. C 41 (1990) 2737.
[13] G.E. Brown, M. Rho, Nucl. Phys. A 372 (1981) 397.

[14] J.P. Delaroche, Y. Wang, J. Rapaport, Phys. Rev. C 39 (1989) 391.
[15] P.A. Moldauer, Nucl. Phys. A 344 (1980) 185.
[16] J.M. Blatt, L.C. Biedenharn, Rev. Mod. Phys. 52 (1952) 725.
[17] A. Gilbert, A.G.W. Cameron, Can. J. Phys. 43 (1965) 1446.
[18] A. Mengoni, Y. Nakajima, J. Nucl. Sci. Technol. 31 (1994) 151.
[19] P.E. Hodgson, Nuclear Reactions and Nuclear Structure, Clarendon Press, Oxford, 1971.
[20] G.R. Satchler, Direct Nuclear Reactions, Oxford Univ. Press, New York, 1983.
[21] F.G. Perey, Phys. Rev. C 131 (1963) 745.
[22] W.L. Goffe, G. Ferrier, J. Rogers, J. Econometrics 60 (1994) 65.
[23] J.R.M. Annand, R.W. Finlay, F.S. Dietrich, Nucl. Phys. A 443 (1985) 249.
[24] R.W. Finlay, W.P. Abfalterer, G. Fink, E. Montei, T. Adami, P.W. Lisowski, G.L. Morgan, R.C. Haight, Phys. Rev. C 47 (1993) 237.
[25] W.P. Abfalterer, F.B. Bateman, F.S. Dietrich, R.W. Finlay, R.C. Haight, G.L. Morgan, Phys. Rev. C 63 (2001) 44608.
[26] E. Fabrici, S. Micheletti, M. Pignanelli, F.G. Resmini, R. DeLeo, G. D'Erasmo, A. Pantaleo, J.L. Escudié, A. Tarrats, Phys. Rev. C 21 (1980) 830.
[27] E. Fabrici, S. Micheletti, M. Pignanelli, F.G. Resmini, R. DeLeo, G. D'Erasmo, A. Pantaleo, Phys. Rev. C 21 (1980) 844.
[28] M. Pignanelli, H.V. von Geramb, R. DeLeo, Phys. Rev. C 24 (1981) 369.
[29] M. Baba, M. Ibaraki, T. Miura, T. Aoki, Y. Hirasawa, H. Nakashima, S. Meigo, S. Tanaka, J. Nucl. Sci. Technol. Suppl. 1 (2000) 683;
M. Ibaraki, M. Baba, T. Miura, Y. Hirasawa, Y. Nauchi, H. Nakashima, S. Meigo, O. Iwamoto, S. Tanaka, Nucl. Instrum. Methods Phys. Res. A 446 (2000) 536.
[30] G.M. Honoré, PhD thesis, Duke University, 1986;
G.M. Honoré, W. Tornow, C.R. Howell, R.S. Pedroni, R.C. Byrd, R.L. Walter, J.P. Delaroche, Phys. Rev. C 33 (1986) 1129.
[31] C.H. Johnson, C. Mahaux, Phys. Rev. C 38 (1988) 2589.
[32] J.P. Delaroche, E. Bauge, P. Romain, S. Vuillier, in: Proceedings of the OECD/NEA Specialists' Meeting on the Nucleon Nucleus Optical Model up to 200 MeV, Bruyères-le-Châtel, 1996, p. 217, available at http://www.nea.fr/html/science/om200/.
[33] R.S. Pedroni, C.R. Howell, G.M. Honoré, H.G. Pfutzner, R.C. Byrd, R.L. Walter, J.P. Delaroche, Phys. Rev. C 38 (1988) 2052.
[34] T. Kawano, F.H. Fröhner, Nucl. Sci. Engrg. 127 (1997) 130.
[35] D. Schmidt, W. Mannhart, Report No. PTB-N-31, PTB Braunschweig, Germany, 1998.
[36] J.P. Delaroche, in: C. Koutsnetzoff (Ed.), Neutron Physics and Nuclear Data for Reactors and Other Applied Purposes, OECD Nuclear Energy Agency, Paris, 1978, p. 366.
[37] R.W. Finlay, J.R.M. Annand, T.S. Cheema, J. Rapaport, F.S. Dietrich, Phys. Rev. C 30 (1984) 796.
[38] C.H. Johnson, D.J. Horen, C. Mahaux, Phys. Rev. C 36 (1987) 2252.
[39] R.F. Carlson, At. Data Nucl. Data Tables 63 (1996) 93.
[40] A. Ingemarsson, J. Nyberg, P.U. Renberg, O. Sundberg, R.F. Carlson, A. Auce, A. Johansson, G. Tibell, B.C. Clark, L. Kurth Kerr, S. Hama, Nucl. Phys. A 653 (1999) 341.
[41] G.R. Satchler, in: D.H. Wilkinson (Ed.), Isospin in Nuclear Physics, North-Holland, Amsterdam, 1969, p. 391.
[42] J.F. Clergeau, L. Roux, J.P. Delaroche, Bruyères-le-Châtel Report, 1996, unpublished.
[43] J. Dechargé, D. Gogny, Phys. Rev. C 21 (1980) 1568;
J.F. Berger, M. Girod, D. Gogny, Comput. Phys. Commun. 63 (1990) 365, and references therein.
[44] C.R. Howell, PhD thesis, Duke University, 1984.
[45] F.D. Becchetti, G.W. Greenlees, Phys. Rev. 182 (1969) 1190.
[46] J. Rapaport, Phys. Rep. 87 (1982) 25.
[47] J. Rapaport, V. Kulkarni, R.W. Finlay, Nucl. Phys. A 330 (1979) 15.
[48] J.P. Jeukenne, A. Lejeune, C. Mahaux, Phys. Rev. C 15 (1977) 10.
[49] D.M. Patterson, R.R. Doering, A. Galonsky, Nucl. Phys. A 263 (1976) 261.
[50] R.P. De Vito, S.M. Austin, U.E.P. Berg, R. De Leo, W.A. Sterrenburg, Phys. Rev. C 28 (1983) 2530.

[51] C.R. Howell, R.S. Pedroni, G.M. Honore, K. Murphy, R.C. Byrd, G. Tungate, R.L. Walter, Phys. Rev. C 38 (1988) 1552.
[52] S.M. Austin, in: C.D. Goodman, S.M. Austin, S. Bloom, J. Rapaport (Eds.), The (p,n) Reaction and the Nucleon–Nucleon Force, Plenum, New York, 1979, p. 203.
[53] J. Rapaport, in: C.D. Goodman, S.M. Austin, S. Bloom, J. Rapaport, G.R. Satchler (Eds.), The (p,n) Reaction and the Nucleon–Nucleon Force, Plenum, New York, 1979, p. 233.
[54] P.E. Hodgson, Rep. Prog. Phys. 47 (1984) 613.
[55] W.D. Myers, Nucl. Phys. A 204 (1973) 465.
[56] J.J.H. Menet, E.E. Gross, J.J. Malanify, A. Zucker, Phys. Rev. C 4 (1971) 1114.
[57] D. Wilmore, P.E. Hodgson, Nucl. Phys. 55 (1964) 673.
[58] R.L. Walter, P.P. Guss, in: P.G. Young (Ed.), Proceedings of the International Conference on Nuclear data for Basic and Applied Science, Santa Fe, 1985, Gordon and Breach, New York, 1986, p. 1079.
[59] D.G. Madland, in: Proceedings of a Specialists' Meeting on Preequilibrium Reactions, Semmering, Austria, February 10–12 1988, OECD, Paris, 1988, p. 103.
[60] S.F. Mughabghab, Neutron Cross Sections, Academic Press, New York, 1984.
[61] T. Schweitzer, D. Seeliger, S. Unholzer, IAEA Report No. IAEA-190-2, 243, 1976.
[62] D.T. Stewart, W.M. Currie, J. Martin, P.W. Martin, Report EANDC-50S, 1, 1965.
[63] G. Haouat, Ch. Lagrange, Y. Patin, R. de Swiniarski, F.S. Dietrich, A. Virdis, in: K.H. Böckhoff (Ed.), Proceedings of the International Conference on Nuclear Data for Science and Technology, Antwerp, 1982, p. 796.
[64] D.B. Thomson, L. Cranberg, J.S. Levin, Phys. Rev. 125 (1962) 2049.
[65] W.E. Kinney, F.G. Perey, Oak Ridge National Laboratory Report No. ORNL-4550, 1970.
[66] A. Mittler, Dissertation Abstracts B 32 (1971) 1142.
[67] J.C. Ferrer, J.D. Carlson, J. Rapaport, Nucl. Phys. A 275 (1977) 325.
[68] R.L. Clarke, W.G. Cross, Nucl. Phys. 53 (1964) 177.
[69] N. Olsson, B. Trostell, E. Ramstroem, B. Holmqvist, Nucl. Phys. A 472 (1987) 237.
[70] R.L. Becker, W.G. Guindon, G.J. Smith, Nucl. Phys. 89 (1966) 154.
[71] W.E. Kinney and F.G. Perey, Oak Ridge National Laboratory Report No. ORNL-4516, 1970.
[72] G. Dagge, W. Grum, J.W. Hammer, K.-W. Hoffmann, G. Schreder, Phys. Rev. C 39 (1989) 1768.
[73] C.S. Whisnant, J.H. Dave, C.R. Gould, Phys. Rev. C 30 (1984) 1435.
[74] Ph. Martin, R.L. Walter, Phys. Rev. C 34 (1986) 384.
[75] J.S. Petler, M.S. Islam, R.W. Finlay, F.S. Dietrich, Phys. Rev. C 32 (1985) 673.
[76] A. Bratenahl, S. Fernbach, R.H. Hildebrand, C.E. Leith, J. Moyer, Phys. Rev. 77 (1950) 597.
[77] G.L. Salmon, Nucl. Phys. 21 (1960) 15.
[78] C.P. Van Zyl, R.G.P. Voss, R. Wilson, Philos. Mag. 1 (1956) 1003.
[79] R. Alarcon, J. Rapaport, Nucl. Phys. A 458 (1986) 502.
[80] R.P. De Vito, S.M. Austin, W. Sterrenburg, U.E.P. Berg, Phys. Rev. Lett. 47 (1981) 628.
[81] J. Rapaport, J.D. Carlson, D. Bainum, T.S. Cheema, R.W. Finlay, Nucl. Phys. A 286 (1977) 232.
[82] K. Tsukada, S. Tanaka, M. Maruyama, Y. Tomita, in: IAEA Seminar on the Physics of Fast and Intermediate Reactors, Vienna, 1961, p. 75.
[83] J. Martin, D.T. Stewart, W.M. Currie, Nucl. Phys. A 113 (1968) 564.
[84] J.D. Brandenberger, A. Mittler, M.T. McEllistrem, Nucl. Phys. A 196 (1972) 65.
[85] B. Holmqvist, T. Wiedling, S.G. Johansson, G. Lodin, A. Kiss, B. Gustavsson, B. Antalkovic, Nucl. Phys. A 146 (1970) 321.
[86] F.G. Perey, W.E. Kinney, Oak Ridge National Laboratory Report No. ORNL-4539, 1970.
[87] R.P. De Vito, PhD thesis, Michigan State University, 1980.
[88] B.E. Leshchenko, G.U. Nurabaeva, Yu.N. Onishchuk, Kiev State University, 1987, unpublished.
[89] P.L. Beach, R.W. Finlay, R.L. Cassola, R.D. Koshel, Phys. Rev. 156 (1967) 1201.
[90] J.H. Towle, W.B. Gilboy, Nucl. Phys. 72 (1965) 515.
[91] J.D. Reber, J.D. Brandbenberger, Phys. Rev. 163 (1967) 1077.
[92] W. Tornow, E. Woye, G. Mack, C.E. Floyd, K. Murphy, P.P. Guss, S.A. Wender, R.C. Byrd, R.L. Walter, T.B. Clegg, H. Leeb, Nucl. Phys. A 385 (1982) 373.
[93] D.E. Bainum, R.W. Finlay, J. Rapaport, J.D. Carlson, W.G. Love, Phys. Rev. C 16 (1977) 1377.
[94] R. Alarcon, J. Rapaport, R.W. Finlay, Nucl. Phys. A 462 (1987) 413.

[95] N. Olsson, E. Ramstroem, B. Trostell, Nucl. Phys. A 513 (1990) 205.
[96] E.L. Hjort, F.P. Brady, J.L. Romero, J.R. Drummond, D.S. Sorenson, J.H. Osborne, B. McEachern, L.F. Hansen, Phys. Rev. C 50 (1994) 275.
[97] A.B. Smith, P.T. Guenther, J. Phys. G 19 (1993) 655.
[98] A.B. Smith, J. Phys. G 24 (1998) 637.
[99] C. St Pierre, M.C. Machwe, P. Lorraine, Phys. Rev. 115 (1959) 999.
[100] F.G. Perey, W.E. Kinney, Oak Ridge National Laboratory Report No. ORNL-4551, 1970.
[101] D. Schmidt, W. Mannhart, Z. Chenwei, in: G. Reffo (Ed.), Proceedings of the International Conference on Nuclear Data for Science and Technology, Trieste, Italy, 1997, p. 407.
[102] W.E. Kinney, F.G. Perey, Oak Ridge National Laboratory Report No. ORNL-4806, 1974.
[103] W.E. Kinney, Oak Ridge National Laboratory Report No. TM-2052, 1968;
W.E. Kinney, Oak Ridge National Laboratory Report No. ORNL-4249, 1968.
[104] S.M. El-Kadi, C.E. Nelson, F.O. Purser, R.L. Walter, A. Beyerle, C.R. Gould, L.W. Seagondollar, Nucl. Phys. A 390 (1982) 509.
[105] S. Mellema, R.W. Finlay, F.S. Dietrich, F. Petrovich, Phys. Rev. C 28 (1983) 2267.
[106] P. Boschung, J.T. Lindow, E.F. Shrader, Nucl. Phys. A 161 (1971) 593.
[107] J.P. Delaroche, S.M. El-Kadi, P.P. Guss, C.E. Floyd, R.L. Walter, Nucl. Phys. A 390 (1982) 541.
[108] T.P. Stuart, J.D. Anderson, C. Wong, Phys. Rev. 125 (1962) 276.
[109] S.T. Lam, W.K. Dawson, S.A. Elbakr, H.W. Fielding, P.W. Green, R.L. Helmer, I.J. van Heerden, A.H. Hussein, S.P. Kwan, G.C. Neilson, T. Otsubo, D.M. Sheppard, H.S. Sherif, J. Soukup, Phys. Rev. C 32 (1985) 76.
[110] P.P. Guss, R.C. Byrd, C.E. Floyd, C.R. Howell, K. Murphy, G. Tungate, R.S. Pedroni, R.L. Walter, J.P. Delaroche, T.B. Clegg, Nucl. Phys. A 438 (1985) 187.
[111] Y. Yamamouti, J. Rapaport, S.M. Grimes, V. Kulkani, R.W. Finlay, D. Bainum, P. Grabmayr, G. Randers-Pehrson, in: Proceedings of the International Conference on Nuclear Cross Sections for Technology, Knoxville, 1979, p. 146.
[112] W.E. Kinney, F.G. Perey, Oak Ridge National Laboratory Report No. ORNL-4807, 1974.
[113] F.G. Perey, C.O. Le Rigoleur, W.E. Kinney, Oak Ridge National Laboratory Report No. ORNL-4523, 1970.
[114] W.E. Kinney, F.G. Perey, Oak Ridge National Laboratory Report No. ORNL-4908, 1974.
[115] C.E. Floyd, P.P. Guss, R.C. Byrd, K. Murphy, R.L. Walter, J.P. Delaroche, Phys. Rev. C 28 (1983) 1498.
[116] P.T. Guenther, D.L. Smith, A.B. Smith, J.F. Whalen, Nucl. Phys. A 448 (1986) 280.
[117] R.S. Harding, Phys. Rev. 111 (1958) 1164.
[118] J.C. Hopkins, D.M. Drake, Nucl. Sci. Engrg. 36 (1969) 275.
[119] B. Holmqvist, T. Wiedling, AE-Report AE-452, 1972.
[120] G.V. Gorlov, N.S. Lebedeva, V.M. Morozov, Dokl. Akad. Nauk 158 (1964) 574.
[121] R.G. Kurup, R.W. Finlay, J. Rapaport, Nucl. Phys. A 420 (1984) 237.
[122] M. Walt, H.H. Barschall, Phys. Rev. 93 (1954) 1062.
[123] D.W. Kent, S.P. Puri, S.C. Snowdon, W.P. Bucher, Phys. Rev. 125 (1962) 331.
[124] H. Nauta, Nucl. Phys. 2 (1956) 124.
[125] D.E. Bainum, R.W. Finlay, J. Rapaport, H.H. Hadizadeh, J.D. Carlson, Nucl. Phys. A 311 (1978) 492.
[126] S.A. Cox and E.E. Dowling, Argonne National Laboratory Report No. ANL-7935, 1972.
[127] V.I. Popov, V.I. Trikova, in: Neutron Physics Conference, Kiev, 1971, p. 223.
[128] P. Kuijper, J.C. Veefkind, C.C. Jonker, Nucl. Phys. A 181 (1972) 545.
[129] R.D. Lawson, P.T. Guenther, A.B. Smith, Phys. Rev. C 34 (1986) 1599.
[130] F.G. Perey, W.E. Kinney, Oak Ridge National Laboratory Report No. ORNL-4552, 1970.
[131] G.M. Honore, R.S. Pedroni, C.R. Howell, H.G. Pfutzner, R.C. Byrd, G. Tungate, R.L. Walter, Phys. Rev. C 34 (1986) 825.
[132] S. Mellema, J.S. Petler, R.W. Finlay, F.S. Dietrich, J.A. Carr, F. Petrovich, Phys. Rev. C 36 (1987) 577.
[133] P.T. Guenther, A.B. Smith, J.F. Whalen, Phys. Rev. C 12 (1975) 1797.
[134] R.W. Stooksberry, J.H. Anderson, M. Goldsmith, Phys. Rev. C 13 (1976) 1061.
[135] W. Tanaka, NEANDC Report No. NEANDC(J)-51/U, 1977, p. 11.
[136] Y. Wang, J. Rapaport, Nucl. Phys. A 517 (1990) 301.
[137] F.D. McDaniel, J.D. Brandenberger, G.P. Glasgow, H.G. Leighton, Phys. Rev. C 10 (1974) 1087.
[138] A.B. Smith, P.T. Guenther, J.F. Whalen, Nucl. Phys. A 415 (1984) 1.

[139] A.B. Smith, P.T. Guenther, R.D. Lawson, Argonne National Laboratory Report No. ANL-NDM-91, 1985.
[140] R.S. Pedroni, R.C. Byrd, G.M. Honoré, C.R. Howell, R.L. Walter, Phys. Rev. C 43 (1991) 2336.
[141] R. Finlay, W. Walter, A. Marcinkowski, J. Rapaport, 1991, unpublished.
[142] A.B. Smith, P.T. Guenther, J.F. Whalen, Nucl. Phys. A 244 (1975) 213.
[143] F.D. McDaniel, J.D. Brandenberger, G.P. Glasgow, M.T. McEllistrem, J.L. Weil, Report ERDA-NDC-9, 315, 1977.
[144] J. Rapaport, T.S. Cheema, D.E. Bainum, R.W. Finlay, J.D. Carlson, Nucl. .Phys. A 313 (1979) 1.
[145] A.B. Smith, P.T. Guenther, J. Phys. G 20 (1994) 795.
[146] A.B. Smith, P.T. Guenther, J.F. Whalen, Argonne National Laboratory Report No. ANL-NDM-71, 1982.
[147] S. Chiba, P.T. Guenther, A.B. Smith, Ann. Nucl. Engrg. 16 (1989) 637.
[148] A.B. Smith, P.T. Guenther, G. Winkler, J.F. Whalen, Nucl. Phys. A 332 (1979) 297.
[149] A.B. Smith, Argonne National Laboratory Report No. ANL-NDM-137, 1996.
[150] A.B. Smith, P.T. Guenther, Nucl. Phys. A 568 (1994) 221.
[151] W.G. Cross, R.G. Jarvis, Nucl. Phys. 15 (1960) 155.
[152] S. Chiba, P.T. Guenther, R.D. Lawson, A.B. Smith, Phys. Rev. C 42 (1990) 2487.
[153] J.O. Elliot, Phys. Rev. 101 (1956) 684.
[154] P.P. Guss, R.C. Byrd, C.R. Howell, R.S. Pedroni, G. Tungate, R.L. Walter, J.P. Delaroche, Phys. Rev. C 39 (1989) 405.
[155] J. Rapaport, M. Mirzaa, H.H. Hadizadeh, D.E. Bainum, R.W. Finlay, Nucl. Phys. A 341 (1980) 56.
[156] C. Budtz-Jörgensen, P.T. Guenther, A.B. Smith, Nucl. Phys. A 415 (1984) 1.
[157] R.M. Wilenzick, K.K. Seth, P.R. Bevington, H.W. Lewis, Nucl. Phys. 62 (1965) 511.
[158] C. Wong, J.D. Anderson, J.W. McClure, B.D. Walker, Phys. Rev. 128 (1962) 2339.
[159] A.B. Smith, Argonne National Laboratory Report No. ANL-149, 2000.
[160] L.A. Rayburn, Phys. Rev. 116 (1959) 1571.
[161] W. Begum, R.B. Galloway, F.K. Mcniel-Watson, Nucl. Phys. A 332 (1979) 349.
[162] V.I. Strizhak, V.V. Bobyr, Sov. Phys. JETP 14 (1962) 225.
[163] L.D. Vincent, I.L. Morgan, J.T. Prud'homme, Wright Air Devel. Centre Report, USA, WADD-TR-60-217 (1960).
[164] R.W. Hill, Phys. Rev. 109 (1958) 2105.
[165] S. Tanaka, Y. Tomita, K. Ideno, S. Kikuchi, Nucl. Phys. A 179 (1972) 513.
[166] W.B. Gilboy, J.H. Towle, Nucl. Phys. 42 (1963) 86.
[167] S.C. Buccino, C.E. Hollandsworth, P.R. Bevington, Z. Phys. 196 (1966) 103.
[168] R. Singh, H.H. Knitter, Z. Phys. A 272 (1975) 47.
[169] D.L. Bernard, G. Lenz, J.D. Reber, in: Proceedings of the 2nd Conference on Nuclear Cross-Sections and Technology, Washington, 1968, p. 755.
[170] D.F. Coope, S.N. Tripathi, M.C. Schell, M.T. McEllistrem, Bull. Am. Phys. Soc. 24 (1979) 854.
[171] G. Haouat, J. Lachkar, Ch. Lagrange, M.T. McEllistrem, Y. Patin, R.E. Shamu, J. Sigaud, Phys. Rev. C 20 (1979) 78.
[172] D.F. Coope, S.N. Tripathi, M.C. Schell, J.L. Weil, M.T. McEllistrem, Phys. Rev. C 16 (1977) 2223.
[173] Ch. Lagrange, R.E. Shamu, T. Burrows, G.P. Glasgow, G. Hardie, F.D. McDaniel, Phys. Lett. B 58 (1975) 293.
[174] M.T. McEllistrem, R.E. Shamu, J. Lachkar, G. Haouat, Ch. Lagrange, Y. Patin, J. Sigaud, F. Cocu, Phys. Rev. C 15 (1977) 927.
[175] R.B. Day, Los Alamos National Laboratory Report, 1965, unpublished.
[176] M. Walt, J.R. Beyster, Phys. Rev. 98 (1955) 677.
[177] B. Holmqvist, T. Wiedling, AE-Report No. AE-366, 1969.
[178] B. Holmqvist, T. Wiedling, J. Nucl. Engrg. 27 (1973) 543.
[179] J.R.M. Annand, R. Galloway, J. Phys. G 11 (1985) 1341.
[180] G.E. Belovitskij, L.N. Kolesnikova, I.M. Frank, Yad. Fiz. 15 (1972) 662.
[181] V.M. Morozov, Ju.G. Zubov, N.S. Lebedeva, Jaderno-Fizicheskie Issledovanija 14 (1972) 8.
[182] M.L. Roberts, P.D. Felsher, G.J. Weisel, Z. Chen, C.R. Howell, W. Tornow, R.L. Walter, D.J. Horen, Phys. Rev. C 44 (1991) 2006, and references therein.
[183] J. Rapaport, T.S. Cheema, D.E. Bainum, R.W. Finlay, J.D. Carlson, Nucl. Phys. A 296 (1978) 95.
[184] R.K. Das, R.W. Finlay, Phys. Rev. C 42 (1990) 1013.

[185] M. Ahmed, F.W.K. Firk, in: 5th Int. Symp. on Polarization Phenomena in Nuclear Physics, Santa Fe, NM, 1980, p. 389.
[186] G.J. Weisel, W. Tornow, C.R. Howell, P.D. Felsher, M. Alohali, M.L. Roberts, R.K. Das, R.L. Walter, G. Mertens, Phys. Rev. C 54 (1996) 2410.
[187] N. Olsson, B. Trostell, E. Ramstroem, B. Holmqvist, F.S. Dietrich, Nucl. Phys. A 472 (1987) 237.
[188] D.C. Larson, J.A. Harvey, N.W. Hill, H. Weigmann, Oak Ridge National Laboratory Report No. ORNL-TM-6420, 1978.
[189] M. Ohkubo, in: P.G. Young (Ed.), Proceedings of the International Conference on Nuclear Data for Science and Technology, Santa Fe, 1985, p. 1623.
[190] G. Rohr, R. Shelley, C. Nazareth, M. Moxon, in: J.K. Dickens (Ed.), Proceedings of the International Conference on Nuclear Data for Science and Technology, Gatlinburg, 1994, p. 215.
[191] D.C. Larson, J.A. Harvey, N.W. Hill, Oak Ridge National Laboratory Report No. ORNL-5787, 1981.
[192] F.G. Perey, T.A. Love, W.E. Kinney, Oak Ridge National Laboratory Report No. ORNL-4823, 1972.
[193] D.C. Larson, C.H. Johnson, J.A. Harvey, N.W. Hill, Oak Ridge National Laboratory Report No. ORNL-TM-5618, 1976.
[194] J.F. Whalen, J.W. Meadows, Argonne National Laboratory Report No. ANL-7210, 1966.
[195] D.G. Foster Jr., D.W. Glasgow, Phys. Rev. C 3 (1971) 576.
[196] C.H. Johnson, J.L. Fowler, N.W. Hill, Bull. Am. Phys. Soc. 23 (1978) 636.
[197] P.T. Guenther, D. Havel, A.B. Smith, J.F. Whalen, Nucl. Phys. A 307 (1978) 224.
[198] R.R. Spencer, H. Beer, F.H. Froehner, Report EANDC(E)-146, 1972.
[199] P.T. Guenther, A.B. Smith, J.F. Whalen, Nucl. Sci. Engrg. 82 (1982) 408.
[200] J.A. Harvey, F.G. Perey, J.A. Hill, Report DOE-NDC-33, 142 (1984).
[201] K. Berthold, C. Nazareth, G. Rohr, H. Weigmann, in: J.K. Dickens (Ed.), Proceedings of the International Conference on Nuclear Data for Science and Technology, Gatlinburg, 1994, p. 224.
[202] C.M. Perey, F.G. Perey, J.A. Harvey, N.W. Hill, N.M. Larson, R.L. Macklin, Oak Ridge National Laboratory Report No. ORNL-TM-10841, 1988.
[203] A. Brusegan, G. Rohr, R. Shelley, E. Macavero, C. van der Vorst, F. Poortmans, I. Mewissen, G. Vanpraet, in: J.K. Dickens (Ed.), Proceedings of the International Conference on Nuclear Data for Science and Technology, Gatlinburg, 1994, p. 224.
[204] M.S. Pandey, J.B. Garg, J.A. Harvey, Phys. Rev. C 15 (1977) 600.
[205] W.P. Poenitz, J.F. Whalen, Argonne National Laboratory Report No. ANL-NDM-80, 1983.
[206] L. Musgrove, J.A. Harvey, W.M. Good, Austr. J. Phys. 30 (1977) 379.
[207] R.W. Stooksberry, J.H. Anderson, Nucl. Sci. Engrg. 51 (1973) 235.
[208] V.V. Filippov, in: Proceedings of the 6th All-Union Conf. on Neutron Physics, Kiev, 1983, p. 107.
[209] P. Lambropoulos, P.T. Guenther, A.B. Smith, J.F. Whalen, Nucl. Phys. A 201 (1973) 1.
[210] R.F. Carlton, S. Raman, J.A. Harvey, G.G. Slaughter, Phys. Rev. C 14 (1976) 1439.
[211] E. Islam, M. Hussain, N. Ameen, M. Enayetullah, N. Islam, Nucl. Phys. A 209 (1973) 189.
[212] J.M. Peterson, A. Bratenahl, J.P. Stoering, Phys. Rev. 120 (1960) 521.
[213] H.S. Camarda, T.W. Phillips, R.M. White, Phys. Rev. C 29 (1984) 2106.
[214] J. Franz, H.P. Grotz, L. Lehmann, E. Roessle, H. Schmitt, L. Schmitt, Nucl. Phys. A 490 (1988) 667.
[215] W.P. Poenitz, J.F. Whalen, A.B. Smith, Nucl. Sci. Engrg. 78 (1981) 333.
[216] R.H. Tabony, K.K. Seth, Ann. Phys. (N.Y.) 46 (1968) 401.
[217] R.F. Carlton, R.R. Winters, J.A. Harvey, N.W. Hill, C.H. Johnson, J. Schiedmayer, Bull. Am. Phys. Soc. 36 (1991) 1349.
[218] J.L. Fowler, E.C. Campbell, Phys. Rev. 127 (1962) 2192.
[219] J.A. Harvey, W.M. Wilson, N.W. Hill, Oak Ridge National Laboratory Report, 1975, unpublished.
[220] P.T. Guenther, A.B. Smith, J.F. Whalen, Nucl. Sci. Engrg. 75 (1980) 69.
[221] I.E. Dayton, G. Schranck, Phys. Rev. 101 (1956) 1358.
[222] R. Dittmann, H.S. Sandhu, R.K. Cole, C.N. Waddell, Nucl. Phys. A 126 (1969) 592.
[223] E. Colombo, R. de Leo, J.L. Escudie, E. Fabrici, S. Micheletti, M. Pignanelli, F. Resmini, J. Phys. Soc. Jpn. 44 (1978) 543.
[224] C.B. Fulmer, J.B. Ball, A. Scott, M.L. Whiten, Phys. Rev. 181 (1969) 1565.
[225] A.E. Taylor, E. Wood, Nucl. Phys. 25 (1961) 642.
[226] V. Comparat, R. Frascaria, N. Marty, M. Morlet, A. Willis, Nucl. Phys. A 221 (1974) 403.

[227] A. Johansson, G. Tibell, K. Parker, P.E. Hodgson, Nucl. Phys. A 21 (1960) 383.
[228] A. Johansson, U. Svanberg, P.E. Hodgson, Ark. Fys. 19 (1961) 541.
[229] D.J. Baugh, G.W. Greenlees, J.S. Lilley, S. Roman, Nucl. Phys. 65 (1965) 33.
[230] L.W. Put, P.P. Urone, A.M. Paans, Phys. Lett. B 35 (1971) 311.
[231] M.P. Fricke, E.E. Gross, A. Zucker, Phys. Rev. 163 (1967) 1153.
[232] H. Sakaguchi, M. Nakamura, K. Hatanaka, A. Goto, T. Noro, F. Ohtani, H. Sakamoto, H. Ogawa, S. Kobayashi, Phys. Rev. C 26 (1982) 944.
[233] C. Olmer, A.D. Bacher, G.T. Emery, W.P. Jones, D.W. Miller, H. Nann, P. Schwandt, S. Yen, T.E. Drake, R.J. Sobie, Phys. Rev. C 29 (1984) 361.
[234] P. Schwandt, H.O. Meyer, W.W. Jacobs, A.D. Bacher, S.E. Vigdor, M.D. Kaitchuck, T.R. Donoghue, Phys. Rev. C 26 (1982) 55.
[235] Q. Chen, J.J. Kelly, P.P. Singh, M.C. Radhakrishna, W.P. Jones, H. Nann, Phys. Rev. C 41 (1990) 2514.
[236] E.T. Boschitz, R.W. Bercaw, J.S. Vincent, Phys. Lett. 13 (1964) 322.
[237] R.L. Varner, PhD thesis, University of North Carolina at Chapel Hill, 1986.
[238] D.L. Watson, J. Lowe, J.C. Dore, R.M. Craig, D.J. Baugh, Nucl. Phys. A 92 (1967) 193.
[239] L.N. Blumberg, E.E. Gross, A. van der Woude, A. Zucker, R.H. Bassel, Phys. Rev. 147 (1966) 812.
[240] E.E. Gross, R.H. Bassel, L.N. Blumberg, B.J. Morton, A. van der Woude, A. Zucker, Nucl. Phys. A 102 (1967) 673.
[241] C. Rolland, B. Geoffrion, N. Marty, M. Morlet, B. Tatischeff, A. Willis, Nucl. Phys. 80 (1966) 625.
[242] A. Nadasen, P. Schwandt, P.P. Singh, W.W. Jacobs, A.D. Bacher, P.T. Debevec, M.D. Kaitchuck, J.T. Meek, Phys. Rev. C 23 (1981) 1023.
[243] H. Seifert, J.J. Kelly, A.E. Feldman, B.S. Flanders, M.A. Khandaker, Q. Chen, A.D. Bacher, G.P.A. Berg, E.J. Stephenson, P. Karen, B.E. Norum, P. Welch, A. Scott, Phys. Rev. C 47 (1993) 1615, and references therein.
[244] J. Stephenson, J. Phys. Soc. Jpn. (Suppl.) 55 (1985) 316.
[245] G.W. Greenlees, C.H. Poppe, J.A. Sievers, D.L. Watson, Phys. Rev. C 3 (1971) 1231.
[246] J. Beneviste, A.C. Mitchel, A.C. Fulmer, Phys. Rev. 133 (1964) B317.
[247] L.L. Lee Jr., J.P. Schiffer, Phys. Rev. 134 (1964) B765.
[248] J.P.M.G. Melssen, PhD thesis, Technische Hogeschool Eindhoven, 1978;
J.P.M.G. Melssen, P.J. van Hall, S.D. Wassenaar, O.J. Poppema, G.J. Nijgh, S.S. Klein, Nucl. Phys. A 376 (1982) 183.
[249] P. Kossanyi-Demay, R. de Swiniarski, C. Glashauser, Nucl. Phys. A 94 (1967) 513.
[250] J.R. Tesmer, F.H. Schmidt, Phys. Rev. C 5 (1972) 864.
[251] D.J. Baugh, M.J. Kemiy, J. Lowe, D.L. Watson, H. Wojciechowski, Nucl. Phys. A 99 (1967) 203.
[252] M.K. Brussel, J.H. Williams, Phys. Rev. 114 (1959) 525.
[253] G.S. Mandi, D.T. Jones, D. Jacques, Nucl. Phys. A 165 (1971) 384.
[254] L. Rosen, J.G. Berry, A.S. Goldhaber, E.H. Auerbach, Ann. Phys. (N.Y.) 34 (1965) 96.
[255] S.F. Eccles, H.F. Lutz, V.A. Madsen, Phys. Rev. 141 (1966) 1067.
[256] B.W. Ridley, J.F. Turner, Nucl. Phys. 58 (1964) 497.
[257] R. Alphonce, A. Johansson, G. Tibell, Nucl. Phys. 4 (1957) 643.
[258] A. Johansson, G. Tibell, P. Hillman, Nucl. Phys. 11 (1959) 540.
[259] S. Kobayashi, K. Matsuda, Y. Nagahara, Y. Oda, N. Yamamuro, J. Phys. Soc. Jpn. 15 (1960) 1151.
[260] N. Baron, R. Leonard, D. Lind, Phys. Rev. 180 (1969) 978.
[261] C.B. Fulmer, Phys. Rev. 125 (1962) 631.
[262] T. Eliyakut-Roshko, R.H. McCamis, W.T.H. van Oers, R.F. Carlson, A.J. Cox, Phys. Rev. C 51 (1995) 1295.
[263] H.S. Liers, R.N. Boyd, C.H. Poppe, J.A. Sievers, D.L. Watson, Phys. Rev. C 2 (1970) 1399.
[264] K. Kwiatkowski, S. Wall, Nucl. Phys. A 301 (1978) 349.
[265] P.G. Roos, N.S. Wall, Phys. Rev. 140 (1965) B1237.
[266] A. Ingemarsson, A. Johansson, G. Tibell, Nucl. Phys. A 322 (1979) 285.
[267] H. Sakaguchi, et al., RCPN Annual Report, 1993, p. 4.
[268] D.W. Dewins, H.H. Forester, G.G. Gigas, Nucl. Phys. 35 (1962) 617.
[269] W.S. Gray, R.A. Kenefick, J.J. Kraushaar, G.R. Satchler, Phys. Rev. 142 (1966) 142.

[270] C. Glashauser, R. de Swiniarski, J. Goudergues, R.M. Lombard, B. Mayer, J. Thirion, Phys. Rev. 184 (1969) 1217.
[271] J.B. Ball, C.B. Fulmer, R.H. Bassel, Phys. Rev. 135 (1964) B706.
[272] R. de Swiniarski, et al., Can. J. Phys. 55 (1977) 43.
[273] S.D. Wassenaar, PhD thesis, Technische Hogeschool Eindhoven, 1982.
[274] M.P. Fricke, E.E. Gross, B.J. Morton, A. Zucker, Phys. Rev. 156 (1967) 1207.
[275] W. Kretscmer, M. Loh, K. Spitzer, W. Stach, Phys. Lett. 87B (1975) 343.
[276] W.T.H. van Oers, H. Haw, N.E. Davison, A. Ingemarsson, B. Fagerstrom, G. Tibell, Phys. Rev. C 10 (1974) 307.
[277] G.W. Greenlees, V. Hnizdo, O. Karban, J. Love, Phys. Rev. C 3 (1970) 1063.
[278] D.A. Hutcheon, et al., in: G.G. Olsen, R.H. Brown, N. Jarnie, W.W. McNaughton, G.M. Hale (Eds.), Polarization Phenomena in Nuclear Physics, 1980, Fifth International Symposium, Santa Fe, Proceedings of the Fifth International Symposium on Polarization Phenomena in Nuclear Physics, in: AIP Conf. Proc., Vol. 69, AIP, New York, 1981, p. 454.
[279] M. Ju, MS thesis, Simon Fraser University, 1987.
[280] N. Ottenstein, S.J. Wallace, J.A. Tjon, Phys. Rev. C 38 (1988) 2272.
[281] S. Yamabe, M. Takeda, M. Kondo, S. Kato, T. Yamazaki, N. Takahashi, N. Kawai, R. Chiba, J. Phys. Soc. Jpn. 17 (1962) 729.